

Dynamic Instabilities and Pattern Formation in Chemotactic Active Matter

Hongbo Zhao,^{1,2,3,4,*} Qiwei Yu,^{5,†} Andrej Košmrlj,^{6,7,‡} and Sujit S. Datta^{8,3,§}

¹*Department of Physics, University of California, San Diego, CA 92093*

²*Department of Chemistry, University of California, San Diego, CA 92093*

³*Department of Chemical and Biological Engineering, Princeton University, Princeton, NJ 08544*

⁴*Omenn-Darling Bioengineering Institute, Princeton University, Princeton, NJ 08544*

⁵*Lewis-Sigler Institute for Integrative Genomics, Princeton University, Princeton, NJ 08544*

⁶*Department of Mechanical and Aerospace Engineering, Princeton University, Princeton, NJ 08544*

⁷*Princeton Materials Institute, Princeton University, Princeton, NJ 08544*

⁸*Division of Chemistry and Chemical Engineering,
California Institute of Technology, Pasadena, CA 91125*

(Dated: March 4, 2026)

Collectives of actively-moving particles can spontaneously segregate into dilute and dense phases through a process known as motility-induced phase separation (MIPS). This captivating phenomenon is well-studied for randomly-moving particles with no directional bias. However, many active systems perform collective chemotaxis—directed motion along a chemical gradient collectively generated by the particles themselves through consumption or production. Here, we use linear stability analysis, amplitude equations, and numerical simulations to study how MIPS is influenced by collective chemotaxis. We find that chemotaxis can either arrest or entirely suppress MIPS, or give rise to novel dynamic instabilities such as traveling waves and spirals. We predict the stability region of the stationary and oscillatory patterns and identify four types of bifurcation that can arise: pitchfork, saddle-node, infinite period, and supercritical Hopf. We also derive analytical expressions for the amplitude of the pattern and traveling wave velocity, yielding excellent quantitative agreement with simulations. Furthermore, we generalize our model to study particles that either consume or produce chemoattractant or chemorepellent, as well as mixtures of particles with different chemotactic behaviors. By establishing quantitative principles describing the competition between MIPS and chemotaxis, our study helps deepen understanding of the rich physics underlying chemically-responsive active matter systems.

I. INTRODUCTION

Active matter systems—such as flocking birds [1–3], swimming bacteria [4, 5], crawling cells [6, 7], and chemically-actuated colloids [8–11]—consume energy to generate mechanical forces, such as those that enable self-propulsion. These out-of-equilibrium systems exhibit fascinating collective behaviors, many of which have now been elucidated by theoretical models and mimicked by artificial systems [12, 13]. A paradigmatic model of such systems is to treat the constituents as active Brownian particles (ABPs) [14] that self-propel at a fixed speed while their orientation fluctuates randomly. At short distances on the order of the particle size, the particles are mutually repulsive. Nevertheless, despite having only these purely repulsive interactions, collectives of ABPs can exhibit motility-induced phase separation (MIPS)—where the particles separate into coexisting dense and dilute phases—when their motion is sufficiently directed [14–18]. This process occurs because the particles slow down in densely-packed regions, which initiates a positive feedback loop where the decrease in mobility further promotes clustering, amplifying spatial

fluctuations in particle density and eventually leading to macroscopic phase separation [14, 18–28].

In reality, however, the constituents of many active matter systems do not move purely randomly. For example, many forms of active matter are chemically responsive: the constituent particles bias their random motion in response to an external chemical gradient, a process known as chemotaxis. When the particles move up (down) the gradient, the chemical is known as a chemoattractant (chemorepellent). This gradient is often established by the constituent particles themselves through collective consumption or production of the chemical—hence, we refer to this form of biased motion as *collective chemotaxis*. Manifestations of this process abound in living and active matter. For example, swimming bacteria use collective chemotaxis to gain access to more nutrients in heterogeneous terrain [4, 29–42]. Another biological example is that of the slime mold *Dictyostelium discoideum*, whose cells move toward self-generated signaling molecules, causing them to aggregate into protective multicellular structures during starvation [4, 43]. Chemotaxis has also been engineered in synthetic self-propelled colloids and droplets, which move using phoresis or Marangoni flow in response to self-generated chemical gradients [9, 10, 21, 44–57], mediating attraction or repulsion between the individual particles in turn [48, 57–60]. Even at the molecular scale, the catalytic activity of enzymes can direct their motion along substrate gradients [61–66]. Given the ubiquity of collective chemotaxis

* hongbo@ucsd.edu

† qiweiyu@princeton.edu

‡ andrej@princeton.edu

§ ssdatta@caltech.edu

in living and active matter, we ask: Does it alter the paradigm of MIPS, and if so, how? And can our findings guide ways to use chemotaxis to engineer collective behaviors, such as pattern formation and large-scale migration [9, 58, 59, 67–77], in such systems?

Recently [78], we took a first step toward addressing these questions by combining established continuum models of MIPS [20, 22–24, 26, 27, 79–82] and collective chemotaxis [29]. We found that when ABPs consume an externally-supplied chemoattractant, collective chemotaxis can generate oscillatory instabilities that manifest as traveling waves or spirals, arrest coarsening during MIPS, or completely suppress MIPS altogether—reminiscent of phenomena observed in diverse active matter systems [83–106]. However, a quantitative theory for the classification of these dynamical patterns and how they emerge or vanish through different bifurcations remains lacking. Moreover, our prior work only focused on consumers of chemoattractant in two dimensions (2D)—whereas many living and active systems involve consumers or producers of chemoattractant or chemorepellent, often with multiple types of such constituents mixed together, in 2D or three dimensions (3D) [107–110]. Here, we build on our continuum model of chemotactic MIPS to address these knowledge gaps.

We first introduce the model in §II and derive the linear stability analysis for the most general case, without invoking any specific constitutive laws, in §III. Focusing on consumers of chemoattractant as an illustrative example, we then use linear stability analysis and 2D numerical simulations to map out the full chemotactic MIPS phase diagram in §IV. We then study the physics of stationary and oscillatory patterns in §V and §VI, respectively. By deriving amplitude equations, we go beyond the linear regime and establish analytical expressions for the pattern amplitude and traveling wave velocity, which we validate with full numerical simulations in both 2D and 3D. Finally, we broaden our study to the case of particles with different chemotactic properties in §VII, and close with discussions in §VIII.

II. MODEL

ABPs are particles of size a that self-propel at a speed U_0 with a randomly fluctuating orientation that decorrelates over a time scale τ_R . The particle persistence length is then $\sim U_0\tau_R$, and the directedness of the ABP motion can therefore be described by the inverse of the reorientation Péclet number, $\text{Pe}_R \equiv a/(U_0\tau_R)$. As established previously [14, 19, 20, 25, 28, 79, 81, 111], in the limit of large time ($t \gg \tau_R$) and length ($l \gg U_0\tau_R$) scales, a coarse-grained continuum equation that describes the dynamics of the ABP density can be derived. This coarse-graining procedure allows one to construct an effective ABP free energy G based on their density-dependent speed, which decreases with density because of steric repulsion between particles, thereby yielding a thermodynamic de-

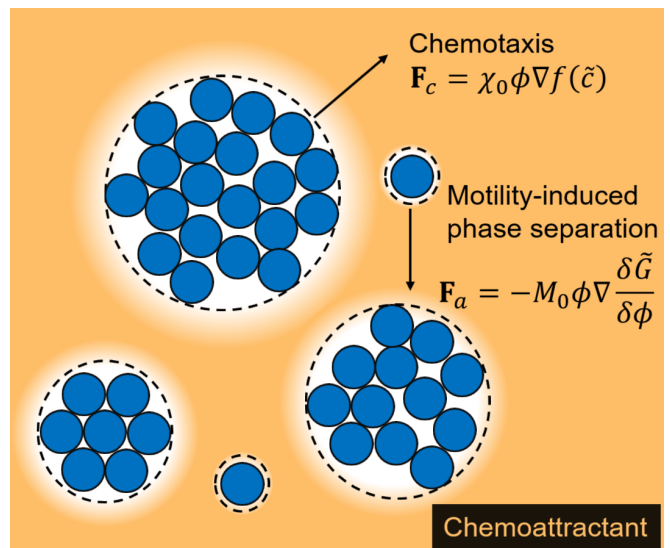


FIG. 1. **Schematic illustration of chemotactic active Brownian particles (ABPs) undergoing motility-induced phase separation.** At sufficiently low reorientation Péclet number Pe_R and moderate particle volume fraction, non-chemotactic ABPs (blue) form dense clusters via MIPS. When particles consume a chemoattractant (yellow), they direct their motion toward higher concentrations and migrate away from depleted clusters. As a result, chemotactic dispersal competes with MIPS clustering. Producers of chemorepellent exhibit qualitatively similar dispersal.

scription of MIPS. Alternatively, an effective free energy can also be derived from a constitutive model for the density-dependent swim pressure [22–24].

In this continuum description, the volume fraction ϕ of non-chemotactic ABPs satisfies the continuity equation $\frac{\partial \phi}{\partial t} = -\nabla \cdot \mathbf{F}_a$, where t is time and \mathbf{F}_a is the flux due to active Brownian motion. Consistent with the free energy formulation, this flux can be written in a form that is driven by the effective chemical potential gradient (Fig. 1),

$$\mathbf{F}_a = -M_0 \phi \nabla \frac{\delta \tilde{G}}{\delta \phi}, \quad (1)$$

where M_0 is the active diffusivity, \tilde{G} is the free energy functional normalized by the characteristic energy scale $\sim \zeta U_0^2 \tau_R$, where ζ is the drag coefficient, and the variational derivative $\delta \tilde{G} / \delta \phi$ is the chemical potential normalized by the same energy scale. When the active diffusivity is dominated by the random propulsion of ABPs, $M_0 = 0.5 U_0^2 \tau_R$ [14, 18, 22, 23, 111]; the specific numeric prefactor based on the free energy model is discussed in §IV.

Following the classical Cahn-Hilliard description of MIPS [14, 112], the free energy functional consists of a normalized bulk free energy density $\tilde{g}_h(\phi, \text{Pe}_R)$ and a term that smooths sharp gradients in ϕ that arise from

phase separation,

$$\tilde{G}[\phi] = \int \left(\tilde{g}_h(\phi, \text{Pe}_R) + \frac{1}{2} \kappa |\nabla \phi|^2 \right) dV, \quad (2)$$

where $\sqrt{\kappa} \sim U_0 \tau_R$ sets the characteristic width of the interface between the dense and dilute phases in MIPS [14, 20, 81]. The normalized chemical potential is then $\tilde{\mu} \equiv \delta \tilde{G} / \delta \phi = \tilde{\mu}_h - \kappa \nabla^2 \phi$, where the normalized bulk chemical potential is $\tilde{\mu}_h(\phi, \text{Pe}_R) = \partial \tilde{g}_h / \partial \phi$. We define characteristic time and length scales $t_0 \equiv \kappa / M_0 \sim \tau_R$ and $l_0 \equiv \sqrt{\kappa}$, respectively, yielding the characteristic speed $v_0 \equiv M_0 / \sqrt{\kappa} \sim U_0$. From the coarse-graining approach, one then obtains that for a broad range of Pe_R and ϕ , $\partial_\phi \mu_h < 0$ —causing a net flux of particles toward high-density regions, triggering the spontaneous formation of dense clusters (Fig. 1), and ultimately causing these clusters to merge and coarsen into distinct macroscopic dense and dilute phases via MIPS [14, 20, 22, 28]. Other generalized models of MIPS [26, 82] that are not derived from a free energy functional can explain additional complexities such as negative surface tension and bubble formation [113] and will be useful to explore in future work.

In addition to moving randomly, many biological and synthetic active matter systems direct their motion via collective chemotaxis. Hence, in Ref. [78], we studied a microscopic model of chemotactic ABPs [60, 71] that experience chemotactic motion, arising from a combination of translation drift along the chemical gradient and a rotational torque that orients the direction of self-propulsion along the chemical gradient, in addition to randomly-oriented self-propulsion. Following the same coarse-graining approach as described above for non-chemotactic ABPs [78], one can derive a lowest-order continuum equation in the limit of long time ($t \gg \tau_R$) and length ($l \gg U_0 \tau_R$) scales. In the resulting continuum model, the active Brownian motion and chemotaxis contribute additively to the particle flux. That is, the particle volume fraction evolves in time as

$$\frac{\partial \phi}{\partial t} = -\nabla \cdot (\mathbf{F}_a + \mathbf{F}_c), \quad (3)$$

where the active Brownian flux \mathbf{F}_a still follows Eq. (1) and \mathbf{F}_c is the chemotactic flux. As described by the celebrated Keller-Segel model [29], which is widely used to describe the chemotaxis of living and synthetic active systems [4, 32, 34–41, 51, 60, 62, 114–121],

$$\mathbf{F}_c = \chi_0 \phi \nabla f(\tilde{c}), \quad (4)$$

where \tilde{c} is the concentration, normalized by a fixed characteristic value, of a diffusible chemical signal that the particles sense and direct their motion in response to. The function $f(\tilde{c})$ describes the ability of the particles to sense the chemical and typically increases monotonically with \tilde{c} . The chemotactic coefficient χ_0 describes the ability of the particles to move along the sensed chemical gradient; when $\chi_0 > 0$ (< 0), the particles move up

(down) the gradient (Fig. 1), and the chemical signal is known as a “chemoattractant” (“chemorepellent”). The chemotactic Péclet number $\text{Pe}_C \equiv \chi_0 / M_0$ then describes the strength of directed chemotaxis relative to undirected active diffusion.

Lastly, the dynamics of the chemical signal itself are described by the reaction-diffusion equation

$$\frac{\partial \tilde{c}}{\partial t} = D_c \nabla^2 \tilde{c} - R(\tilde{c}, \phi), \quad (5)$$

where $R(\tilde{c}, \phi)$ is the net depletion rate of the chemical. For generality, we take $R = g(\tilde{c})\phi + S(\tilde{c})$, where the first term describes uptake by the particles at a rate $g(\tilde{c})$ per particle, and the second term describes the degradation (or replenishment, if $S < 0$) rate of the chemical. We define normalized rates $\tilde{R} \equiv R/k$, $\tilde{g} \equiv g/k$, and $\tilde{S} \equiv S/k$ using the same characteristic rate constant k . Comparing the rates of chemical uptake and diffusion over the length scale l_0 then defines the Damköhler number $\text{Da} \equiv k\kappa / D_c$. We also define the dimensionless parameter $\alpha \equiv M_0 / D_c$, which compares the ABP and chemical diffusivities.

This approach combines two established models of active matter that are typically studied separately: MIPS of randomly-moving active particles and collective chemotaxis of directed active particles, described by the first and second terms of the governing Eq. (3), respectively. In the limit that the active particles are non-chemotactic ($\text{Pe}_C = 0$), Eq. (3) becomes decoupled from Eq. (5) and our model recovers conventional MIPS, as expected. Conversely, in the limit that the particles are strongly chemotactic, but are too dilute to cluster and exhibit MIPS, our model instead reduces to the conventional Keller-Segel model of chemotaxis, again as expected. In this case, if the particles consume a chemoattractant or produce a chemorepellent ($\chi_0 g > 0$), they move along the collectively-generated gradient and disperse—as exemplified by bacteria migrating toward nutrients in traveling fronts [34, 35, 38, 40, 115, 122, 123]. Conversely, if the particles produce chemoattractant or consume chemorepellent ($\chi_0 g < 0$), they instead aggregate—as exemplified by the “chemotactic condensation” of microbes in stressful conditions [114, 116, 119–121]. But how do these different effects of MIPS and collective chemotaxis interact? Our model of “chemotactic active matter” addresses this gap in knowledge. As described below, this model exhibits fascinating dynamic instabilities and pattern formation resulting from active clustering in MIPS competing with active dispersal induced by collective chemotaxis when $\chi_0 g > 0$ (Fig. 1), or alternatively, MIPS becoming reinforced by chemotaxis when $\chi_0 g < 0$.

III. GENERAL LINEAR STABILITY ANALYSIS

Linear stability framework. To identify how MIPS is influenced by collective chemotaxis, we first perform a linear stability analysis of our continuum model [Eqs. (1),

(3), (4), and (5)] for the most general case—without any assumptions on the functional forms of the chemical potential $\tilde{\mu}_h(\phi, \text{Pe}_R)$, chemotactic sensing function $f(\tilde{c})$, and chemical depletion rate $R(\tilde{c}, \phi)$. In later sections, specific functional forms relevant to experimental active systems will be discussed, and the full model will be solved numerically using these specific functional forms. The only condition we place is that there exists a homogeneous dynamic steady state with spatially uniform particle volume fraction $\phi(\mathbf{x}) = \phi_0$ and spatially uniform and nonzero chemical concentration $\tilde{c}(\mathbf{x}) = \tilde{c}_0 > 0$, from which we perform our linear stability analysis. To accomplish this steady state, the net depletion rate of the chemical must be zero everywhere: $R(\tilde{c}_0, \phi_0) = g(\tilde{c}_0)\phi_0 + S(\tilde{c}_0) = 0$. That is, the chemical is neither fully depleted nor accumulates without bound, which can be accomplished by, e.g., externally supplying the chemical when it is consumed by the particles, or by allowing the chemical to degrade when the particles produce it.

To perform linear stability analysis, we perturb this homogeneous steady state $\phi(\mathbf{x})$ and $\tilde{c}(\mathbf{x})$ with small-amplitude fluctuations of spatial wavevector \mathbf{q} and growth rate ω , $\delta\phi = \delta\hat{\phi}e^{\omega t + i\mathbf{q}\cdot\mathbf{x}}$, and $\delta\tilde{c} = \delta\hat{c}e^{\omega t + i\mathbf{q}\cdot\mathbf{x}}$, respectively. Substituting this perturbed state into linearized versions of Eqs. (3) and (5) yields the eigenvalue problem $(\omega\mathbf{I} - \mathbf{J}) \cdot (\delta\hat{\phi}, \delta\hat{c})^T = 0$, where \mathbf{I} is the identity matrix and the Jacobian matrix is

$$\mathbf{J} = \begin{pmatrix} -M_0\phi_0q^2(\partial_\phi\tilde{\mu}_h + \kappa q^2) & \chi_0\phi_0q^2f' \\ -g & -D_cq^2 - \partial_cR \end{pmatrix}; \quad (6)$$

here, $q = |\mathbf{q}|$ is the wavenumber, f' is the derivative of $f(c)$ with respect to c , and all derivatives are taken at ϕ_0 and \tilde{c}_0 . The solution to the eigenvalue problem then gives the dispersion relation $\omega(q)$ describing the rate at which fluctuations of different wavenumbers q grow or shrink. We normalize these quantities by the corresponding values of the most unstable mode in non-chemotactic MIPS: $\tilde{\omega} \equiv \omega/\omega_0$ and $\tilde{q} \equiv q/q_0$, where the maximal growth rate $\omega_0 = \max_q \omega(q; \chi_0 = 0) = M_0\phi_0(\partial_\phi\tilde{\mu}_h)^2/\kappa$ and corresponding most unstable wavenumber $q_0 = \arg \max_q \omega(q; \chi_0 = 0) = (|\partial_\phi\tilde{\mu}_h|/\kappa)^{1/2}$. Similarly, we define $\tilde{\mathbf{J}} \equiv \mathbf{J}/\omega_0$.

The normalized Jacobian $\tilde{\mathbf{J}}$ has two invariants, which are the trace $\text{tr}(\tilde{\mathbf{J}})$ and the determinant $\det(\tilde{\mathbf{J}})$, related to the two eigenvalues $\tilde{\omega}_\pm$ by $\text{tr}(\tilde{\mathbf{J}}) = \tilde{\omega}_- + \tilde{\omega}_+$ and $\det(\tilde{\mathbf{J}}) = \tilde{\omega}_-\tilde{\omega}_+$. The two invariants of $\tilde{\mathbf{J}}$ are described by the three dimensionless parameters governing chemotactic active matter:

$$\alpha' \equiv \frac{M_0\phi_0|\partial_\phi\tilde{\mu}_h|}{D_c} = \frac{\text{ABP diffusion rate}}{\text{Chemical diffusion rate}}, \quad (7)$$

$$\text{Da}' \equiv \frac{\partial_cR}{D_cq_0^2} = \frac{\text{Differential reaction rate}}{\text{Chemical diffusion rate}}, \quad (8)$$

$$\text{Pe}'_C \equiv \frac{\chi_0\phi_0f'}{M_0\phi_0|\partial_\phi\tilde{\mu}_h|} \frac{g}{\partial_cR} = \frac{\text{Chemotactic response rate}}{\text{ABP diffusion rate}}, \quad (9)$$

which as expected are proportional to the parameters α , Da and Pe_C introduced in §II. However, these parameters are weighted by additional factors that arise from the linear stability analysis: $\alpha' = \alpha\phi_0|\partial_\phi\tilde{\mu}_h|$, $\text{Da}' = \text{Da}(\partial_c\tilde{R})/|\partial_\phi\tilde{\mu}_h|$, and $\text{Pe}'_C = \text{Pe}_C f' \tilde{g}/(|\partial_\phi\tilde{\mu}_h|\partial_c\tilde{R})$. Using these definitions, the two invariants of $\tilde{\mathbf{J}}$ are

$$\text{tr}(\tilde{\mathbf{J}}) = -\tilde{q}^4 - \left(\sigma + \frac{1}{\alpha'}\right)\tilde{q}^2 - \frac{\text{Da}'}{\alpha'} \quad (10)$$

$$\det(\tilde{\mathbf{J}}) = \frac{\tilde{q}^2}{\alpha'} [(\tilde{q}^2 + \sigma)(\tilde{q}^2 + \text{Da}') + \text{Da}'\text{Pe}'_C], \quad (11)$$

where $\sigma = \text{sgn}(\partial_\phi\tilde{\mu}_h)$; that is, $\sigma = 1$ or -1 outside or inside the region, respectively, in which non-chemotactic ABPs exhibit spinodal decomposition (hereafter referred to as the ‘‘MIPS spinodal region’’), respectively.

Before proceeding, we comment on the sign of the dimensionless parameters. Since the diffusivities are positive ($M_0 > 0$ and $D_c > 0$), $\alpha' > 0$. We restrict our subsequent analysis to the case of $\partial_cR > 0$, that is, the chemical uptake rate increases with increasing chemical concentration. In other words, we require that the chemical reaction is autoinhibitory, because if the reaction is autocatalytic ($\partial_cR < 0$), the chemical concentration field is always unstable under a spatially uniform perturbation ($q = 0$), when one of the eigenvalues is $-\partial_cR$. We focus on the case where R increases strictly monotonically with c such that a unique solution for \tilde{c}_0 exists for $R(\tilde{c}_0, \phi_0) = 0$ given ϕ_0 . Therefore, $\text{Da}' > 0$. Lastly, because $f' > 0$, the sign of Pe'_C depends on χ_0g . As discussed in §II, when $\text{Pe}'_C > 0$ ($\chi_0g > 0$), chemotaxis causes particles to disperse while when $\text{Pe}'_C < 0$ ($\chi_0g < 0$), it causes particles to aggregate. Hence, in the following sections, we term $|\chi_0g|$ the chemotactic dispersal or aggregation rate, depending on the sign of χ_0g .

Stability conditions. Next, we use this linear stability analysis to identify the conditions under which chemotactic active matter systems are linearly stable. In particular, the stability condition for the homogeneous state $\text{Re } \tilde{\omega}_\pm \leq 0$ is equivalent to $\text{tr}(\tilde{\mathbf{J}}) \leq 0$ and $\det(\tilde{\mathbf{J}}) \geq 0$ for all \tilde{q} . Since $\max_{\tilde{q}} \text{tr}(\tilde{\mathbf{J}}) = \frac{1}{4\alpha'^2}(\min\{\sigma\alpha' + 1, 0\})^2 - \frac{\text{Da}'}{\alpha'}$ and $\min_{\tilde{q}} \alpha'\tilde{q}^{-2}\det(\tilde{\mathbf{J}}) = -\frac{1}{4}(\min\{\sigma + \text{Da}', 0\})^2 + \text{Da}'(\text{Pe}'_C + \sigma)$, this stability condition is then equivalent to

$$\text{Da}' \geq \frac{(\min\{\sigma\alpha' + 1, 0\})^2}{4\alpha'} \equiv \text{Da}'_{\text{crit}}, \quad (12)$$

and

$$\text{Pe}'_C \geq \frac{(\min\{\text{Da}' + \sigma, 0\})^2}{4\text{Da}'} - \sigma \equiv \text{Pe}'_{C,\text{crit}}. \quad (13)$$

At the critical condition $\text{Da}' = \text{Da}'_{\text{crit}}$, the critical wavenumber is $\tilde{q}_{\text{crit},1}^2 = \min\left\{0, -\frac{\sigma + \alpha'^{-1}}{2}\right\}$ and at the critical condition $\text{Pe}'_C = \text{Pe}'_{C,\text{crit}}$, the critical wavenumber is

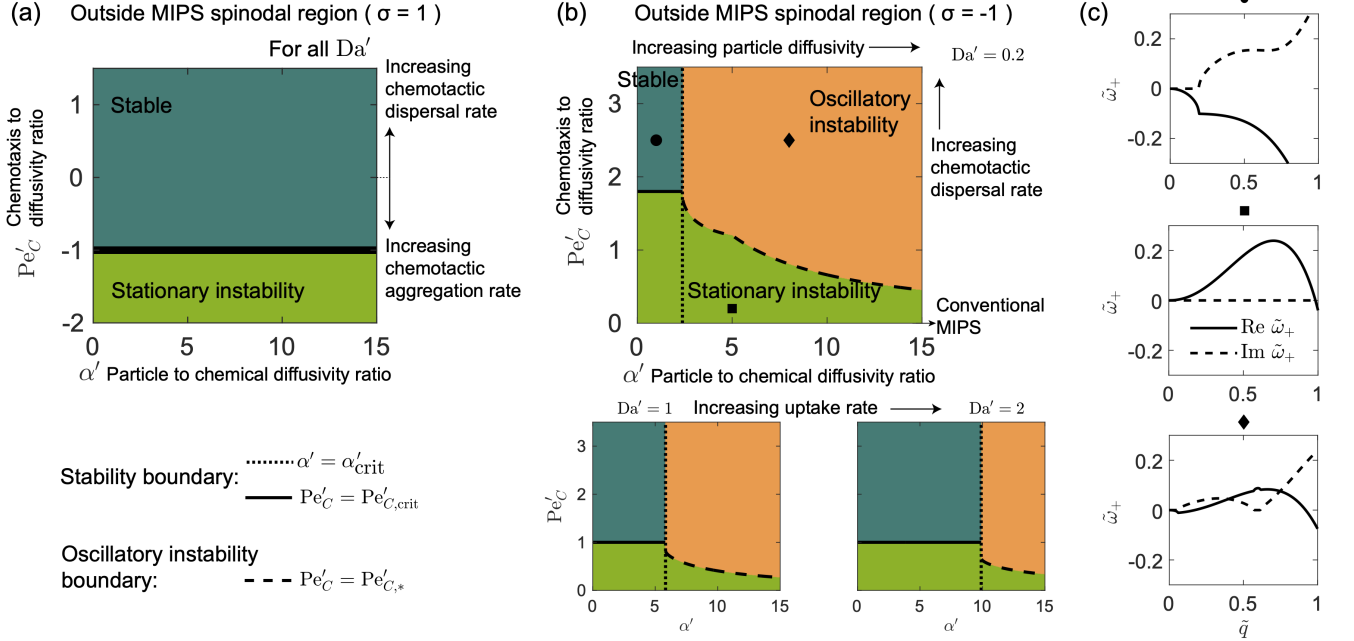


FIG. 2. **Linear stability analysis reveals three distinct regimes of chemotactic MIPS depending on chemical diffusivity and chemotactic strength.** (a) Outside the MIPS spinodal region ($\sigma = 1$), the uniform state is stable when $Pe'_C \geq -1$, independent of Da' and α' ; stationary instability occurs when $Pe'_C < -1$. (b) Inside the MIPS spinodal region ($\sigma = -1$), three regimes emerge: stable (dark teal, where $\alpha' \leq \alpha'_{crit}$ and $Pe'_C \geq Pe'_{C,crit}$), stationary instability (light green), and oscillatory instability (orange, where $\alpha' > \alpha'_{crit}$ and $Pe'_C > Pe'_{C,*}$). Increasing Da' (faster chemical uptake) shrinks both instability regions. (c) Representative dispersion relations showing the positive branch of the nondimensionalized eigenvalue $\tilde{\omega}_+$ at $Da' = 0.2$ for the three regimes marked in (b): stable (dot), stationary instability (square), and oscillatory instability (diamond).

$\tilde{q}_{crit,2}^2 = \min\left\{0, -\frac{\sigma + Da'}{2}\right\}$. Thus, outside the MIPS spinodal region ($\sigma = 1$), the stability condition reduces to $Pe'_C \geq -1$, while the other condition $Da' \geq 0$ is satisfied automatically. This condition represents the stability condition of the classical Keller-Segel model — chemotactic aggregation occurs when $\chi_0 g$ is sufficiently negative.

As shown in Fig. 2(a), the system is linearly stable when $Pe'_C \geq -1$, and exhibits a stationary instability when $Pe'_C < -1$, independent of Da' and α' . By contrast, inside the MIPS spinodal region ($\sigma = -1$), phase separation is suppressed when $Pe'_C \geq Pe'_{C,crit} > 0$, i.e., chemotactic dispersal is sufficiently rapid, and $Da' > Da'_{crit}$. This latter condition is equivalent to $\alpha' \leq 1 + 2Da' + 2\sqrt{Da'(1 + Da')} \equiv \alpha'_{crit}$, i.e., the chemical diffusivity is sufficiently fast compared to the particle diffusivity, as shown by the dark teal region in Fig. 2(b). An example of the dispersion relation $\tilde{\omega}_+(\tilde{q})$ in this linearly stable regime ($\text{Re } \tilde{\omega}_+ < 0$) is shown by the dot in Fig. 2(c). This region of linear stability expands with faster chemical uptake (increasing Da'), as shown by the different panels of Fig. 2(b).

Classification of instabilities. Having established the conditions under which chemotactic active matter is linearly stable, we next categorize the conditions under which it is unstable. We focus on two classes of instabil-

ity. The first is known as a stationary instability, in which all unstable modes with $\text{Re } \tilde{\omega}(\tilde{q}) > 0$ have $\text{Im } \tilde{\omega}(\tilde{q}) = 0$. This instability arises at sufficiently small Pe'_C , as shown in light green in panels (a)-(b), consistent with the fact that as Pe'_C decreases to 0, the model reduces to standard MIPS. An example of the corresponding dispersion relation is shown by the square in Fig. 2(c). The second class is known as an oscillatory instability, in which there exists a wavenumber \tilde{q} for which $\text{Re } \tilde{\omega}(\tilde{q}) > 0$ and $\text{Im } \tilde{\omega}(\tilde{q}) \neq 0$. This condition is equivalent to the condition that there exists \tilde{q} for which $\text{tr}(\tilde{\mathbf{J}}) > 0$ and $\Delta < 0$, where $\Delta = \text{tr}(\tilde{\mathbf{J}})^2 - 4\det(\tilde{\mathbf{J}})$ is the discriminant. As noted earlier, the requirement that $\text{tr}(\tilde{\mathbf{J}}) > 0$ is equivalent to $Da' < Da'_{crit}$, which is only possible when $\sigma = -1$ (inside the MIPS spinodal region), and is equivalent to $\alpha' > \alpha'_{crit}$. In this case, Eqs. (10) and (11) yield

$$\Delta(\tilde{q}) = \left[\tilde{q}^4 + \left(\sigma - \frac{1}{\alpha'} \right) \tilde{q}^2 - \frac{Da'}{\alpha'} \right]^2 - \frac{4Da'Pe'_C}{\alpha'} \tilde{q}^2, \quad (14)$$

which shows that that $\Delta(\tilde{q}) < 0$ is possible only when Pe'_C is positive and sufficiently large. Altogether, this analysis indicates that an oscillatory instability arises when four criteria are met: (i) The system is in the MIPS spinodal region, (ii) chemical diffusivity is sufficiently slow relative to the particle diffusivity, i.e., $\alpha' > \alpha'_{crit}$, (iii) chemotaxis drives particles to disperse, i.e.,

$\chi_{0g} > 0$, and (iv) chemotaxis is sufficiently strong, i.e., $\text{Pe}'_C > \text{Pe}'_{C,*}$ where the critical value $\text{Pe}'_{C,*}$ is given by Eq. (S6). The emergence of oscillatory instability at sufficiently large Pe'_C and α' is shown by the orange region in Fig. 2(b). An example of the corresponding dispersion relation is shown by the diamond in Fig. 2(c). These criteria can be summarized in a simple, intuitive picture: an oscillatory instability emerges due to the competition between clustering via MIPS and dispersal via collective chemotaxis, in the case where the chemical signal diffuses so slowly that its gradient lags behind the moving particles.

IV. PHASE DIAGRAM OF CHEMOTACTIC MIPS

Construction of the phase diagram. The phase diagram of non-chemotactic ABPs is conventionally parameterized by the average particle volume fraction ϕ_0 and the reorientation Péclet number Pe_R [14]. In particular, MIPS occurs at intermediate ϕ_0 and high directedness of self-propulsion (small Pe_R). We now build on our analysis in §III to extend the canonical MIPS phase diagram to account for the effect of chemotaxis using specific illustrative models of $\tilde{\mu}_h(\phi, \text{Pe}_R)$, $f(c)$, and $R(c, \phi)$.

Refs. [22, 23] used a mechanical model to derive the effective free energy density of non-chemotactic ABPs as a function of ϕ_0 and Pe_R . In particular, for ABPs in 2D or 3D, the normalized chemical potential is given by

$$\begin{aligned} \tilde{\mu}_h(\phi, \text{Pe}_R) = & \ln \phi + 1 - 2\phi - 0.3\phi^2 \\ & - \frac{4}{\pi} \text{Pe}_R \phi_m \left(\ln \left[1 - \frac{\phi}{\phi_m} \right] - \frac{\phi}{\phi_m - \phi} \right) \quad (2D) \quad (15) \end{aligned}$$

$$\begin{aligned} \tilde{\mu}_h(\phi, \text{Pe}_R) = & \ln \phi + 1 - 2\phi - 1.5\phi^2 \\ & - 3\text{Pe}_R \phi_0 \left[\ln \left(1 - \frac{\phi}{\phi_m} \right) - \frac{\phi}{\phi_m - \phi} \right] \quad (3D), \quad (16) \end{aligned}$$

where the maximum dense-packing density in 2D or 3D is $\phi_m = 0.9$ or 0.65 , respectively, and the chemical potential is normalized by $\zeta U_0^2 \tau_R / 2$ or $\zeta U_0^2 \tau_R / 6$, respectively. We use these established relations here, first focusing our analysis on the well-studied 2D case [Eq. (15)], and then extending our analysis to 3D in §VI [Eq. (16)].

As an illustrative example, we first examine particles that consume the chemical signal ($g > 0$); the opposite case of particles that instead produce the chemical signal is then discussed in §VII. To satisfy the conditions specified in §III that $\partial_c R > 0$ and a homogeneous steady state exists, we take $g(\tilde{c}) = k\tilde{c}$ with the chemical signal supplied at a constant, spatially-uniform rate $S(\tilde{c}) = -S_0$. The uniform chemical concentration at steady state is then $\tilde{c}_0 = S_0 / (k\phi_0)$. We also take $f(\tilde{c}) = \tilde{c}$ as is commonly done. Because the governing Eqs. (3) and (5) are then linear with respect to $\delta\tilde{c} \equiv \tilde{c} - \tilde{c}_0$, scaling the supply

rate S_0 by a constant is equivalent to scaling the chemotactic rate and hence Pe_C by the same constant. Therefore, without loss of generality, we fix the supply rate to be $S_0/k = 1$. Supplementary Table S1 summarizes all these constitutive relations as well as the corresponding relationships between the dimensionless parameters α , Da , Pe_C , and the reduced versions α' , Da' , and Pe'_C .

With these choices, we can now use the results of our linear stability analysis in §III to construct the full phase diagram of chemotactic MIPS—which is parameterized by $\{\phi_0, \text{Pe}_R\}$ as well as the three new dimensionless parameters $\{\alpha, \text{Da}, \text{Pe}_C\}$. For ease of visualization, we show the linear stability boundary by the gray surface in the three-dimensional $\{\phi_0, \text{Pe}_R, \text{Pe}_C\}$ phase space for $\text{Da} = 0.3$ and $\alpha = 1$ or 10 in Fig. 3(a),(d). Below the stability boundary, the homogeneous state is unstable to small perturbations and the system undergoes phase separation, whereas above it, phase separation is suppressed. Cross-sections through this stability boundary at $\text{Pe}_C = 0.35$ and 0.8 are shown by the black curves in panels (b)-(c) and (e)-(f) in Fig. 3, along with snapshots of numerical simulations at $t = 2 \times 10^4 t_0$ shown by the inset panels, confirming that phase separation occurs below the stability boundary. The boundary at $\text{Pe}_C = 0$ corresponds to the conventional spinodal curve of non-chemotactic ABPs, below which typical MIPS occurs. We also show how the stability boundary changes with varying Da in Fig. 4. Below, we highlight the key results emerging from our analysis; their mathematical proofs are given in Supplementary Information §S1 A.

Chemotaxis suppresses phase separation. In the case of $\text{Da} = 0.3$, $\alpha = 1$ [Fig. 3(a)-(c)], the stability boundary corresponds to $\text{Pe}'_C = \text{Pe}'_{C,\text{crit}}$; the boundary given by $\alpha' = \alpha'_{\text{crit}}$ corresponds to $\text{Pe}_R < 0$ and is therefore inapplicable. Below the stability boundary shown in (a), the system thus exhibits a stationary instability. As indicated by the sloping nature of this boundary, the region of phase separation shrinks with increasing Pe_C . Additionally, visual inspection of the simulation results in (b)-(c) shows that, whereas the dense and dilute phases continually coarsen over time in conventional MIPS, chemotaxis arrests this process—resulting in the formation of stationary, finite-sized dot and stripe patterns. We characterize these patterns further in §V.

Notably, these results are for consumers of a chemoattractant ($\text{Pe}_C > 0$), for which chemotaxis drives particle dispersal (Fig. 1). However, for the opposite case of consumers of a chemorepellant, chemotaxis drives aggregation, not dispersal, as discussed in §II. Consistent with this expectation, we find the opposite behavior when Pe_C is increasingly negative—the region of phase separation instead *expands* compared to the non-chemotactic case.

Chemotaxis can generate an oscillatory instability. As noted in §III, chemotaxis can also generate an oscillatory instability when the chemical signal diffuses

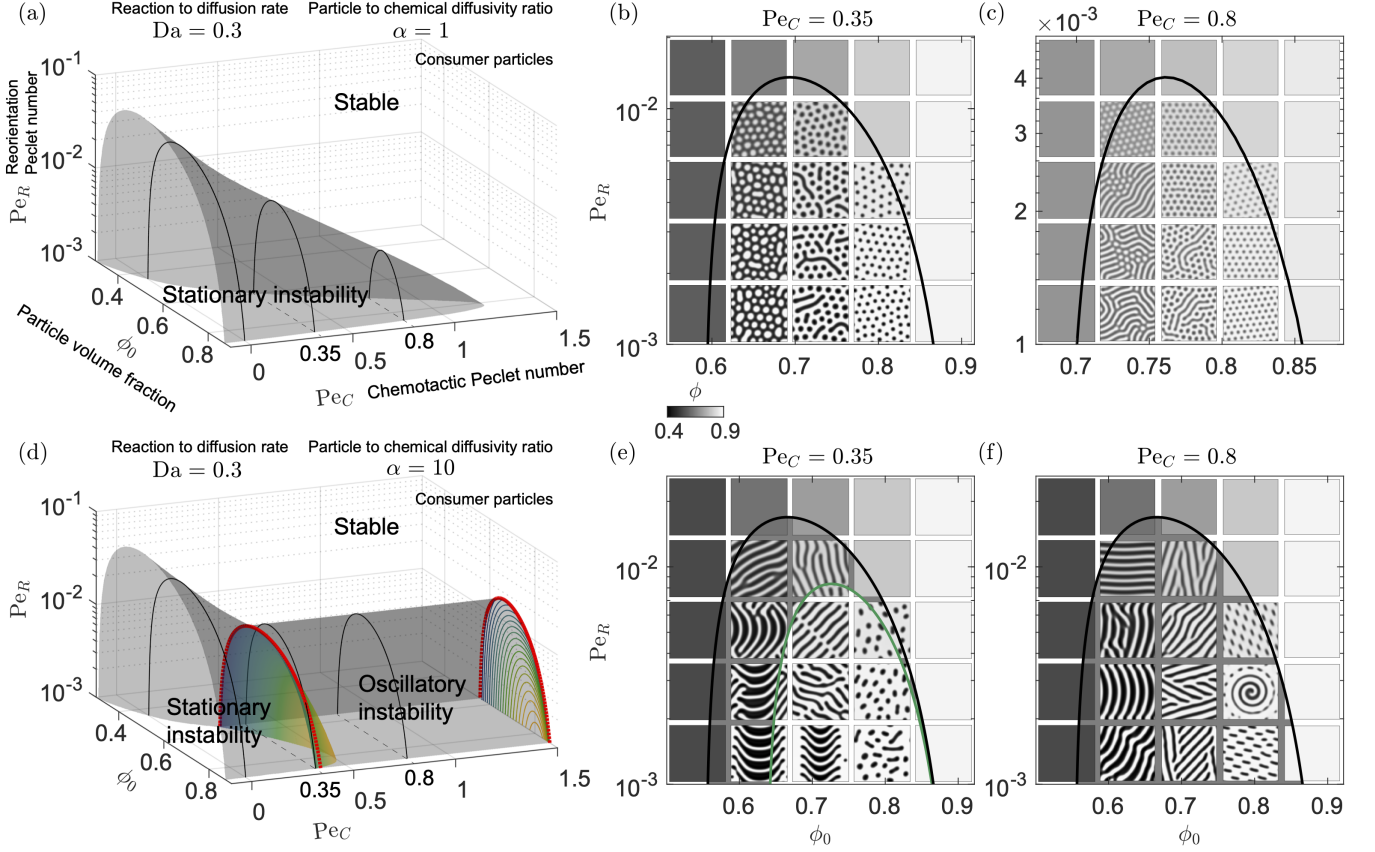


FIG. 3. Three-dimensional phase diagram reveals how chemotaxis suppresses MIPS and generates oscillatory instabilities in consumer particles. (a,d) Phase behavior of chemotactic ABPs that consume a chemoattractant in the $Pe_R - \phi_0 - Pe_C$ phase space at $Da = 0.3$ with $\alpha = 1$ (a) and $\alpha = 10$ (d). Gray surface marks the stability boundary from linear stability analysis; above it, the homogeneous state is stable, while below it, phase separation occurs. At small α (a), chemotaxis arrests coarsening below the boundary, producing stationary dots and stripes. At large α (d), the colored surface delineates stationary (left) from oscillatory (right) instability; the color represents the value of Pe_C , and the colormap ranges from the minimum to maximum values of Pe_C of the surface. The red dashed curve marks the transition from one regime to the other ($Pe'_C = Pe'_{C,crit}$ and $\alpha' = \alpha'_{crit}$). (b-c, e-f) Cross-sections of the $Pe_R - \phi_0$ phase space at $Pe_C = 0.35$ and 0.8 ; black curves are cross-sections through the gray surface, and the green curve in (e) shows a cross-section through the colored surface in (d). We expect a stationary instability below the black curves in (b)-(c) and below the green curve in (e), and an oscillatory instability in the gray shaded region between the black and green curves in (e) and below the black curve in (f). Simulation snapshots at $t = 2 \times 10^4 t_0$ confirm our predictions, with stationary dots/stripes at small α and traveling waves/dots at large α . Simulations use $[100l_0, 100l_0]$ periodic domains with homogeneous initial conditions plus small perturbations. Increasing Pe_C shrinks the phase separation region; increasing α expands the oscillatory regime.

so slowly that its gradient lags behind the moving particles. We explore this behavior by increasing α from 1 to 10, keeping $Da = 0.3$. As shown by the gray surface in Fig. 3(d), the stability boundary now consists of two parts. The first part lying to the left of the left-most red dashed curve is independent of α and corresponds to $Pe'_C = Pe'_{C,crit}$, as in panel (a). In this region, below the stability boundary, chemotaxis suppresses phase separation and generates a stationary instability, as discussed previously for $\alpha = 1$. The second part of the stability boundary lies to the right of the left-most red dashed curve, and corresponds to $\alpha' = \alpha'_{crit}$, which is independent of Pe_C . In this region, below the stability boundary, phase separation always occurs, regardless of

the value of Pe_C . Moreover, when chemotactic dispersal is sufficiently fast ($Pe'_C > Pe'_{C,*}$) — i.e., to the right of the bowed colored surface in panel (d), above the green boundary in (e), and below the black boundary in (f) — the system exhibits an oscillatory instability. The simulation results shown in (e)-(f) present examples of this instability, which results in the formation of traveling waves, traveling dots, and dynamic spiral patterns. Interestingly, the simulations indicate that oscillatory instability also arises below the green boundaries in (e), where the linear stability analysis predicts a stationary instability in this region instead. We revisit this point and provide a more accurate theoretical prediction for the incidence of oscillatory instability in §VI.

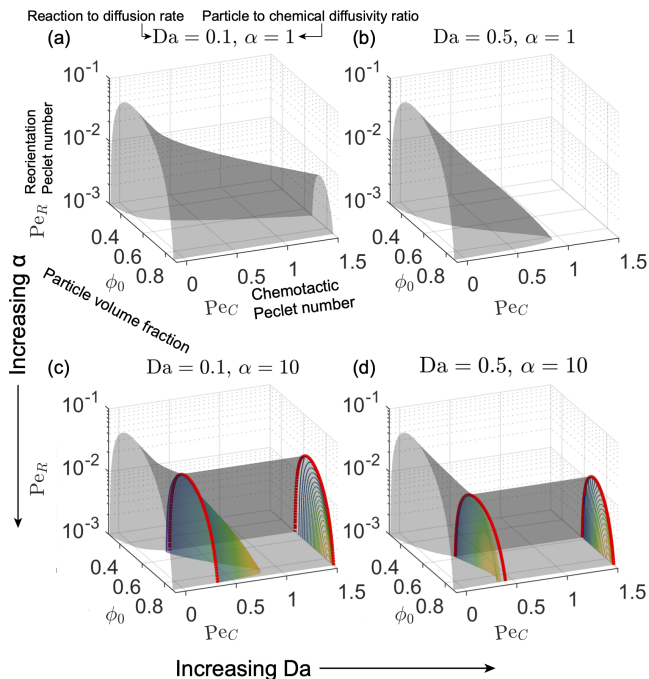


FIG. 4. **Increasing chemical uptake rate (Da) and particle-to-chemical diffusivity ratio (α) systematically alter the phase separation and oscillatory instability regions.** (a-b) At small $\alpha = 1$, increasing Da from 0.1 to 0.5 shrinks the stationary instability region, demonstrating that faster chemical uptake suppresses phase separation. (c-d) At large $\alpha = 10$, increasing Da similarly contracts both the phase separation region and the oscillatory instability region (colored surface).

Faster chemical uptake suppresses phase separation. How does increasing the rate of chemical uptake by the ABPs relative to its diffusion (i.e., increasing Da) influence phase behavior? We first examine the boundary corresponding to $Pe'_C = Pe'_{C,crit}$ demarcating the onset of stationary instability. When chemotactic dispersal is slow — specifically, when $Pe_C < Da \cdot \phi_0^3 k / S_0$ — this stability boundary is independent of Da, as we show in §S1 A. However, when chemotactic dispersal is sufficiently fast, the stability boundary shifts downward with increasing Da, as seen by comparing Figs. 4(a), 3(a), and 4(b). Next, we examine the boundary corresponding to $\alpha' = \alpha'_{crit}$ demarcating the onset of oscillatory instability. In this case, increasing Da also shifts the stability boundary downward, as seen by comparing Figs. 4(c), 3(d), and 4(d). These results are also corroborated by Fig. 2(b). Altogether, they demonstrate that faster chemical uptake suppresses phase separation, no matter the nature of the instability.

V. STATIONARY PATTERNS

Amplitude equation formulation. The results in Fig. 3(b)-(c) showed the emergence of finite-sized dot and stripe patterns in the stationary instability region. While linear stability analysis can capture the onset of the instability that causes these patterns to form (§IV), it cannot predict the morphology of the resulting patterns. To extend our analysis beyond the linear regime, we employ the amplitude equation method [124]—a systematic perturbative approach that describes pattern formation in the weakly nonlinear regime by tracking the slow evolution of pattern amplitude and phase. This method enables us to predict not only when stationary patterns emerge, but also their characteristic size, morphology, and stability, as demonstrated in other phase-separating biophysical systems [125].

To derive the amplitude equation, we expand the particle density and chemical concentration fields around the homogeneous steady state as $\phi = \phi_0 + \phi_1$ and $\tilde{c} = \tilde{c}_0 + \tilde{c}_1$, where ϕ_0 and \tilde{c}_0 are the homogeneous steady state solutions introduced in §III, and ϕ_1 and \tilde{c}_1 are the leading-order perturbations that represent small but finite-amplitude deviations from the uniform state. Following the standard amplitude equation formalism [124] and an established mean-field model of MIPS [79], we approximate the normalized bulk free energy density \tilde{g}_h using a fourth-order Ginzburg-Landau expansion around ϕ_0 . Taylor expanding the normalized bulk chemical potential $\tilde{\mu}_h(\phi) = \partial\tilde{g}_h/\partial\phi$ to third order in ϕ_1 yields $\tilde{\mu}_h(\phi) \approx \tilde{\mu}_h(\phi_0) - a\phi_1 + b\phi_1^2 + \gamma\phi_1^3$ where $a \equiv -\partial\tilde{\mu}_h/\partial\phi$, $b \equiv (\partial^2\tilde{\mu}_h/\partial\phi^2)/2$ and $\gamma \equiv (\partial^3\tilde{\mu}_h/\partial\phi^3)/6$, with all derivatives evaluated at ϕ_0 . Since ϕ_1 is small, the ABP mobility $M_0\phi_0$ and chemotactic coefficient $\chi_0\phi_0$ can be treated as constants.

With $g(\tilde{c}) = f(\tilde{c}) = \tilde{c}$ as before, the governing equations for ϕ_1 and \tilde{c}_1 are then

$$\begin{aligned} \frac{\partial\phi_1}{\partial t} &= M_0\phi_0\nabla^2(-a\phi_1 + \gamma\phi_1^2 + b\phi_1^3 - \kappa\nabla^2\phi_1) - \chi_0\phi_0\nabla^2\tilde{c}_1, \\ \frac{\partial\tilde{c}_1}{\partial t} &= D_c\nabla^2\tilde{c}_1 - k(\phi_0\tilde{c}_1 + \tilde{c}_0\phi_1 + \tilde{c}_1\phi_1). \end{aligned} \quad (17)$$

The perturbations ϕ_1 and \tilde{c}_1 can be decomposed into Fourier modes, $\phi_1 = \sum_{n=1}^N A_{\phi,n} e^{i\mathbf{k}_n \cdot \mathbf{x}} + \text{c.c.}$ and $\tilde{c}_1 = \sum_{n=1}^N A_{c,n} e^{i\mathbf{k}_n \cdot \mathbf{x}} + \text{c.c.}$, where the subscript $n = 1, \dots, N$ labels the Fourier modes, \mathbf{k}_n is the wavevector of the n th mode (distinct from \mathbf{q} used in the linear stability analysis), $A_{c,n}$ and $A_{\phi,n}$ are the complex amplitudes, and c.c. denotes the complex conjugate. To analyze spatially periodic patterns, it suffices to consider spatially uniform amplitudes with a single characteristic wavenumber $k_c = |\mathbf{k}_n|$. Substituting the amplitude expansion into Eq. (17) then yields the amplitude equations:

$$\begin{aligned} \frac{dA_{\phi,n}}{dt} &= -M_0\phi_0k_c^2 \left[(\kappa k_c^2 - a)A_{\phi,n} + \gamma \sum_{\mathbf{k}_n=\mathbf{k}_m+\mathbf{k}_p} A_{\phi,m}A_{\phi,p} + b \sum_{\mathbf{k}_n=\mathbf{k}_m+\mathbf{k}_p+\mathbf{k}_r} A_{\phi,m}A_{\phi,p}A_{\phi,r} \right] + \chi_0\phi_0k_c^2A_{c,n}, \\ \frac{dA_{c,n}}{dt} &= -(D_c k_c^2 + k\phi_0)A_{c,n} - k\tilde{c}_0A_{\phi,n} - k \sum_{\mathbf{k}_n=\mathbf{k}_m+\mathbf{k}_p} A_{c,m}A_{\phi,p}, \end{aligned} \quad (18)$$

which represent a dynamical system whose attractors represent patterns of different morphologies. We classify the emergence and stability of these states using bifurcation theory [126] below.

Stability of pattern morphologies. We consider three steady-state solutions of the amplitude equations — uniform, stripes, and arrays of dots. It suffices to consider up to $N = 3$ modes whose wavevectors are separated by $2\pi/3$ angles; the normalized characteristic wavenumber $\tilde{k}_c \equiv k_c l_0$. For convenience, we express the complex amplitudes in polar form $A_{\phi,n} = R_{\phi,n}e^{i\psi_n}$ and $A_{c,n} = R_{c,n}e^{i\varphi_n}$; explicit expressions for the moduli $R_{\phi,n}$, $R_{c,n}$ and phases ψ_n , φ_n are given by Eqs. (S7)–(S10) in Supplementary Information §S2. Our results are summarized in Fig. 5(a), which shows the amplitude equation predictions in the $\text{Pe}_C - \text{Da}$ phase diagram along with simulations of the weakly nonlinear model [Eq. (17)].

First, we consider the uniform (homogeneous) solution. Since all amplitudes are zero, the stability is completely captured by linear stability analysis. As detailed in §III, we expect this state to be stable in the region above the purple curve in Fig. 5(a). In this regime of large Pe_C and Da , fast chemotaxis and chemical uptake suppress phase separation.

Next, we consider the stripes solution, which has one nonzero Fourier mode: $R_{\phi,1} = R_\phi$, $R_{c,1} = R_c$, and $R_{\phi,2} = R_{\phi,3} = R_{c,2} = R_{c,3} = 0$. As derived in §S2 A 2, the steady-state amplitude is

$$R_\phi = \frac{1}{\sqrt{3b}} \sqrt{a - \tilde{k}_c^2 - \frac{\text{Da} \cdot \text{Pe}_C \cdot \tilde{c}_0}{\tilde{k}_c^2 + \text{Da} \cdot \phi_0}} \leq \sqrt{\frac{a - a_c}{3b}} \quad (19)$$

with $R_c = \frac{\text{Da} \cdot c_0}{\tilde{k}_c^2 + \text{Da} \cdot \phi_0} R_\phi$. Therefore, the stripe pattern exists only when $a > a_c \equiv 2\sqrt{\text{Da} \cdot \text{Pe}_C \cdot \tilde{c}_0} - \text{Da} \cdot \phi_0$, with an amplitude that scales as $R_\phi \sim \sqrt{a - a_c}$. That is, as a exceeds a_c , stripes emerge from the uniform state through a pitchfork bifurcation [126]. Moreover, the pattern amplitude is maximized when $\tilde{k}_c^2 = \tilde{k}_{c,\text{max}}^2 \equiv \max\{\sqrt{\text{Da} \cdot \text{Pe}_C \cdot \tilde{c}_0} - \text{Da} \cdot \phi_0, 0\}$. Note that the conditions $a > a_c$ and $\tilde{k}_{c,\text{max}}^2 > 0$ are equivalent to $\text{Pe}'_C < \text{Pe}'_{C,\text{crit}}$ and $\text{Da}' < 1$, which lie in the unstable regime of the linear stability analysis [Eqs. (12) and (13)].

The stability of the stripe morphology, which is determined by the Jacobian of the full amplitude equation, can be decomposed into stability in two directions: R , which is the amplitude, and $\Theta \equiv \theta - \psi$, which is the phase difference between ϕ and c . At steady state, $\Theta = \pi(+2n\pi)$,

which means that they are in antiphase: Regions abundant with particles are scarce in the chemoattractant and vice versa. In the Θ direction, the antiphase fixed point ($\cos \Theta = -1$) is stable when $\alpha < 4/(\text{Pe}_C \tilde{c}_0)$. When $\alpha > 4/(\text{Pe}_C \tilde{c}_0)$, a new fixed point appears with a finite phase shift. It represents oscillatory patterns with a velocity proportional to $\sin \Theta$ [§VI]. The stability in the R direction can be obtained by numerically computing the eigenvalues of the 4×4 Jacobian and finding the region with only negative eigenvalues. The combined stability region of the stripe solution is to the left of the orange line in Fig. 5(a).

We then consider the dots solution, which is represented by 3 Fourier modes ($N = 3$) of equal amplitudes: $R_{\phi,1} = R_{\phi,2} = R_{\phi,3} = R_\phi$, $R_{c,1} = R_{c,2} = R_{c,3} = R_c$. Using the same characteristic wavenumber $\tilde{k}_c^2 = \tilde{k}_{c,\text{max}}^2$ that maximizes the amplitude of R_ϕ (which also maximizes the amplitude for the stripes solution), as derived in §S2 A 3, the steady-state amplitude is

$$R_\phi = \frac{1}{15b} \left(|\gamma - \text{Da}| + \sqrt{(\gamma - \text{Da})^2 + 15b(a - a_c)} \right), \quad (20)$$

again with $R_c = \frac{\text{Da} \cdot c_0}{\tilde{k}_c^2 + \text{Da} \cdot \phi_0} R_\phi$. Therefore, the dots pattern exists only when $(\gamma - \text{Da})^2 + 15b(a - a_c) > 0$. It emerges through a saddle-node bifurcation, with a finite amplitude $R_{\phi,\text{crit}} = |\gamma - \text{Da}|/(15b)$ at the critical point. The dots and homogeneous solution can coexist in the bistable region of $-(\gamma - \text{Da})^2/(15b) < a - a_c < 0$. Similar to the stripes case, the stability boundaries of the dots solution are obtained by numerically calculating the eigenvalues of the Jacobian [§S2 A 3]. The resulting stable region of the dots solution is in between the green lines in Fig. 5(a).

To examine this saddle-node bifurcation in detail, we perform a hysteresis analysis. In Fig. 5(b), we zoom in on the region near the stability boundary of the uniform and dots solution and track the amplitude of the pattern R_ϕ as we ramp the value of Pe_C up and down across the phase boundary [along the vertical double-headed black arrow in Fig. 5(a)]. Since the uniform solution is stable when $a < a_c$, as we decrease Pe_C [which decreases a_c ; see dark blue points in (b)], the amplitude remains zero, until $a = a_c$ where the uniform state is destabilized and dots emerge. On the other hand, since the dots solution is stable when $a > a_c - (\gamma - \text{Da})^2/(15b)$, as we increase Pe_C [which increases a_c ; see orange points in (b)], the dots solution remain stable until $a = a_c - (\gamma - \text{Da})^2/(15b)$, which is the saddle-node bifurcation point (black point). Thus,

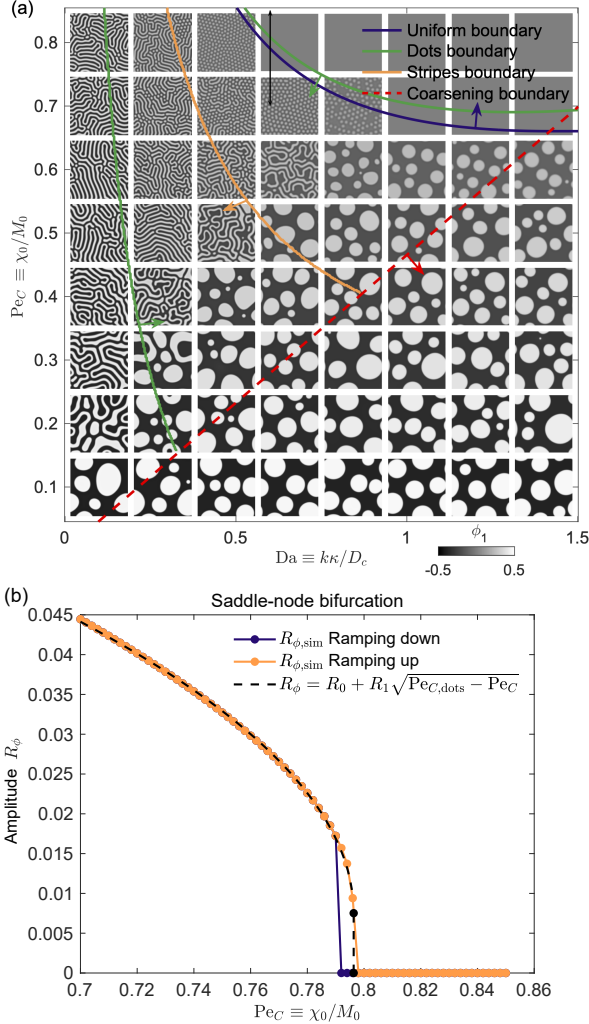


FIG. 5. Amplitude equation analysis quantitatively predicts the stability boundaries and bifurcation types of stationary patterns. (a) Phase diagram in $Pe_C - Da$ space with $Pe_R = 10^{-3}$, $\phi_0 = 0.775$, and $\alpha = 2$, showing pattern morphologies from simulations of the weakly nonlinear model [Eq. 17]. Stability boundaries predicted by the amplitude equation (solid curves) separate uniform (purple), stripes (yellow), and dots (green) solutions, with excellent agreement with simulations. Bistable regions exist where dots coexist with either stripes or uniform states. Below the red dashed line ($\sqrt{Da \cdot Pe_C \cdot \tilde{c}_0} = Da \cdot \phi_0$), patterns coarsen to system size. Simulations are performed on a $[200l_0, 200l_0]$ periodic domain and solved on a 512×512 grid. The snapshots are taken at $t = 10^5 t_0$. These parameters are selected such that no oscillatory patterns emerge. (b) Hysteresis at the uniform-to-dots transition [$Da = 0.6$, double-headed vertical arrow in (a)] demonstrates a saddle-node bifurcation. We calculate the amplitude from each simulation as $R_{\phi,sim} = \sqrt{\int (\phi(\mathbf{x}) - \phi_0)^2 d\mathbf{x} / (6 \int d\mathbf{x})}$. Ramping Pe_C down (blue) shows that the pattern persists below the stability threshold, while ramping up (orange) shows a delayed onset. Amplitude follows the fitted curve $R_\phi = R_0 + R_1 \sqrt{Pe_{C,dots} - Pe_C}$ (dashed line), where R_0 and R_1 are fit parameters; R_0 is nonzero at the bifurcation, indicating saddle-node behavior.

simulation of the model confirms the predicted hysteresis in $a \in (a_c - (\gamma - Da)^2 / (15b), a_c)$.

Expanding the amplitude [Eq. (20)] with respect to Pe_C at the critical value at the bifurcation point $Pe_{C,dots}$, the amplitude follows $R_\phi = R_0 + R_1 \sqrt{Pe_{C,dots} - Pe_C}$ for $Pe_C < Pe_{C,dots}$ (black dashed line). As a key characteristic of the saddle-node bifurcation, the amplitude has a nonzero value R_0 at the bifurcation point. We find excellent agreement between the black dashed line and the numerical results.

Pattern selection and coarsening. For both stripes and dots, the amplitude is maximized at characteristic wavevector $\tilde{k}_c = k_{c,max}$, which establishes the preferred domain size $L_c = 2\pi/k_{c,max}$. When $\sqrt{Da \cdot Pe_C \cdot \tilde{c}_0} < Da \cdot \phi_0$, however, the maximum amplitude is reached in the long wavelength limit, which means that the domains will coarsen until reaching the system size. This boundary is indicated by the red dashed line in Fig. 5(a) ($Pe_C = Da \cdot \phi_0^2 \tilde{c}_0^{-1}$). Coarsening occurs below this line, where chemotaxis is slow, and the chemical uptake rate is fast (small Pe_C and large Da).

Altogether, this analysis predicts six different stable stationary patterns in the $Pe_C - Da$ phase diagram shown in Fig. 5(a): (i) uniform above the purple curve, (ii) dot-uniform coexistence between the purple curve and the rightmost green curve, (iii) dots in between the orange and the purple curve, (iv) dot-stripe coexistence in between the leftmost green and orange curves, (v) stripes to the left of the leftmost green curve, and (vi) coarsening below the red dashed line. Our simulations confirm all these predictions, as shown by the inset panels in Fig. 5(a), except for slightly above the coarsening boundary, where the observed coarsening is possibly due to a finite system size.

Having established the stability boundaries of each pattern type, we now examine the bistability and hysteresis that arise when multiple solutions are stable. The phase diagram in Fig. 5(a) contains two bistable regions in between the leftmost green and orange curves and between the rightmost green and purple curves, where the dots pattern can coexist with stripes or the uniform state, respectively. A consequence of this bistability is that the pattern morphology should be hysteretic if parameters are varied in different directions. Fig. 5(b) already demonstrated hysteresis at the uniform-dots saddle-node bifurcation. We extend this analysis in Fig. S1, which shows the influence of ramping up and down the value of Da for each Pe_C , using the final steady state at the previous Da as the initial condition for the next Da value. We again observe the coexistence of dots and stripes (or uniform) solutions in the region where both states are stable. As expected for a bistable system, the dominance of one state over the other depends on the direction of the ramping: for example, when exploring dots-stripes coexistence, we find that stripes dominate in the coexistence region when ramping up the value of Da , while dots dominate when ramping down the value of Da . We observe

a similar hysteretic effect in the region where both dots and the uniform state are stable.

While the above results demonstrate excellent agreement between amplitude equation predictions and simulations of the weakly nonlinear model [Eq. (17)], we now assess the range of validity of the amplitude equation approach by comparing with numerical simulations of the full model. As shown in Fig. S2, as we move from the uniform phase to pattern forming phase by decreasing Da and Pe_C , the amplitude equation qualitatively captures the transition from uniform to dots to stripes as well as bistability between them. However, the agreement deteriorates far from the stability boundaries, where the weakly nonlinear approximation breaks down. Notably, the coarsening boundary $\text{Pe}_C > \text{Da}\phi_0^2\tilde{c}_0^{-1}$ (below the red dashed line) remains an accurate predictor of when patterns will coarsen to the system size, even in regions where other quantitative predictions deviate.

VI. OSCILLATORY PATTERNS

Plane wave analysis and existence conditions. Having analyzed stationary patterns in §V, we now turn to the oscillatory patterns—traveling waves, traveling dots, and spirals—that emerge when chemical diffusivity is sufficiently slow compared to particle mobility ($\alpha' > \alpha'_{\text{crit}}$) and chemotactic dispersal is sufficiently strong ($\text{Pe}_C > \text{Pe}'_{C,\text{crit}}$). We again use the amplitude equation method to predict when these patterns emerge, their velocities, and their amplitudes, which we validate through numerical simulations.

To understand the basic properties of oscillatory patterns, we begin by analyzing the simplest case: a plane-wave solution with $N = 1$ mode. We assume the wave propagates with a constant phase difference $\Theta \equiv \theta - \psi$ between the chemical and particle density fields, and with angular velocity $\omega = d\theta/dt = d\psi/dt$. That is, $\phi(\mathbf{x}, t) - \phi_0 = R_\phi e^{i(k_c \mathbf{x} + \omega t)} + \text{c.c.}$ and $\tilde{c} - \tilde{c}_0 = R_c e^{i(k_c \mathbf{x} + \omega t + \Theta)} + \text{c.c.}$ Substituting this ansatz into the amplitude equations [Eq. (18)] yields the traveling wave velocity, as derived in §S2 B:

$$v = \frac{\omega}{k_c} = v_0 \sqrt{\text{Da} \cdot \tilde{c}_0 \phi_0 \alpha^{-1} \cdot \text{Pe}_C} \sin \Theta, \quad (21)$$

where the phase difference satisfies

$$\cos \Theta = -\frac{\tilde{k}_c^2 + \text{Da} \cdot \phi_0}{\tilde{k}_c \sqrt{\text{Da} \cdot \tilde{c}_0 \alpha \phi_0 \cdot \text{Pe}_C}}. \quad (22)$$

Three key insights emerge from these equations. First, a finite phase shift between the particle and chemical fields ($\sin \Theta \neq 0$) is required for traveling waves to emerge; when $\Theta \rightarrow \pi$, the velocity v vanishes, and patterns become stationary. Second, since $\cos \Theta > -1$, traveling waves can only exist when

$$\tilde{k}_c + \frac{\text{Da} \cdot \phi_0}{\tilde{k}_c} < \sqrt{\text{Da} \cdot \tilde{c}_0 \alpha \phi_0 \cdot \text{Pe}_C}. \quad (23)$$

This condition requires both fast chemotaxis (large Pe_C) and slow chemical diffusion (large α). Third, the amplitude is given by

$$R_\phi = \frac{1}{\sqrt{3b}} \sqrt{a - \tilde{k}_c^2 - \frac{\text{Pe}_C \cdot \text{Da} \cdot \tilde{c}_0}{\tilde{k}_c^2 + \text{Da} \cdot \phi_0} \cos^2 \Theta}, \quad (24)$$

which is only stable when

$$\tilde{k}_c^2 + \frac{\text{Da}}{\tilde{k}_c^2 \alpha} + \frac{1}{\alpha \phi_0} < a, \quad (25)$$

as detailed in §S2 B.

Two bifurcation regimes. Two distinct bifurcation regimes emerge depending on which condition—existence [Eq. (23)] or stability [Eq. (25)]—is more restrictive. In both regimes, traveling waves are only stable when chemical diffusion is sufficiently slow compared to particle mobility: namely $\alpha > \alpha_c$ where α_c is a critical value that depends on Pe_C .

The first regime corresponds to small Pe_C , such that the existence condition [Eq. (23)] is more restrictive. Minimizing the left-hand side of this condition with respect to \tilde{k}_c gives $\alpha_c = 4/(\text{Pe}_C \cdot \tilde{c}_0)$, which is achieved at the critical wavenumber $\tilde{k}_c = \sqrt{\text{Da} \cdot \tilde{c}_0}$. At this wavenumber, the wave velocity is maximized:

$$\frac{v}{v_0} = \alpha^{-1} \sqrt{\text{Da} \cdot \tilde{c}_0 \phi_0 \cdot \text{Pe}_C (\alpha - \alpha_c)}. \quad (26)$$

The key signature of this regime is that as when $\alpha < \alpha_c$, the stripes solution is stable, while as α increases past α_c , stripes continuously transition to traveling waves. The amplitude R_ϕ remains finite and continuous across the transition, while the velocity grows continuously from zero as $v/v_0 \propto \alpha^{-1} \sqrt{\alpha - \alpha_c}$. This behavior is the signature of an infinite-period bifurcation at $\alpha = \alpha_c$.

The second regime corresponds to large Pe_C , where the stability condition [Eq. (25)] is more restrictive. Minimizing the left-hand side of this condition yields $a > 2\sqrt{\text{Da}/\alpha} + (\alpha \phi_0)^{-1}$, which gives $\alpha_c = a^{-2} \left(\sqrt{\text{Da}} + \sqrt{\text{Da} + a \phi_0^{-1}} \right)^2$, above which the traveling wave solution is stable. Note that $\alpha \leq \alpha_c$ is equivalent to the stability condition of the uniform state $\alpha' \leq \alpha'_{\text{crit}}$. At the critical wavenumber $\tilde{k}_c = (\text{Da}/\alpha)^{1/4}$, the velocity is

$$\begin{aligned} \frac{v}{v_0} &= \alpha^{-1} \sqrt{\text{Da} \cdot \tilde{c}_0 \phi_0 \cdot \text{Pe}_C} \\ &\times \sqrt{\alpha - \frac{\sqrt{\alpha \cdot \text{Da} \phi_0}}{\text{Pe}_C \cdot \tilde{c}_0} \left(1 + \frac{1}{\sqrt{\text{Da} \cdot \alpha \phi_0}} \right)^2} \end{aligned} \quad (27)$$

and the amplitude is

$$R_\phi = \frac{1}{\sqrt{3b}} \sqrt{a - \frac{1}{\alpha \phi_0} - 2\sqrt{\frac{\text{Da}}{\alpha}}}. \quad (28)$$

The key signature of this regime is that as α increases past α_c , the uniform state transitions to traveling waves. The amplitude grows continuously from zero as $R_\phi \propto \sqrt{\alpha - \alpha_c}$, while the velocity undergoes a discontinuous jump from zero to a finite value. This behavior is the signature of a supercritical Hopf bifurcation at $\alpha = \alpha_c$.

In summary, the critical α above which traveling waves exist and are stable is

$$\alpha_c = \max \left\{ \frac{4}{\text{Pe}_C \cdot \tilde{c}_0}, \frac{1}{a^2} \left(\sqrt{\text{Da}} + \sqrt{\text{Da} + a\phi_0^{-1}} \right)^2 \right\}. \quad (29)$$

The Pe_C value dividing the two regimes is given by equating these two expressions.

Comparison with numerical simulations. We now validate these predictions through numerical simulations. Fig. 6(a) shows the full model simulated across the $\text{Pe}_C - \alpha$ phase space with $\text{Da} = 0.5$, $\text{Pe}_R = 10^{-3}$, $\phi_0 = 0.8$. As expected from linear stability analysis [Fig. 2(b)], to the left of the stability boundary $\alpha' = \alpha'_{\text{crit}}$ (dotted line at $\alpha = 2$), the system reaches stationary states: either uniform (above the solid curve where $\text{Pe}_C > \text{Pe}_{C,\text{crit}}$) or stationary stripes/dots (below it).

To study the transition to oscillatory patterns, we gradually increase α for each value of Pe_C , using the final state from the previous α as the initial condition. Traveling stripes and dots emerge when α exceeds a critical value that decreases with increasing Pe_C , consistent with our predictions. We quantify the velocity of stripes that span the entire domain using the level-set velocity ($\mathbf{u} = -\partial_t \phi \nabla \phi / |\nabla \phi|^2$, i.e., the velocity at which contours of $\phi(x, t)$ move in the direction along the gradient), denoted by the red arrows in Fig. 6(a). The speed of the pattern v is the average of $|\mathbf{u}|$ in space, excluding regions with small $|\nabla \phi|$. For traveling dots and short stripes with a small aspect ratio, the velocity \mathbf{u} is obtained by tracking the center of mass of the pattern instead. The speed v is the average of $|\mathbf{u}|$ of all the dots or stripes.

The amplitude equation prediction [Eq. (29), blue curve] accurately captures the onset of oscillatory patterns, as shown in Fig. 6(a). By contrast, the linear stability prediction [Eq. S6] overestimates the critical α , as shown by the black dashed curve. Nevertheless, it captures the qualitative trend of decreasing critical α with increasing Pe_C . This discrepancy is expected: linear stability analysis applies only near the uniform state, while amplitude equations remain valid for transitions from both uniform and patterned states.

Velocity and amplitude scaling. Next, we examine the velocity and amplitude predicted by the amplitude equations by performing numerical simulations with high resolutions of α and Pe_C values. The results are shown in Fig. 6(b,c) with snapshots shown in Fig. S3.

Fig. 6(b) shows the average normalized speed $\tilde{v} = v/v_0$ as a function of α for different values of Pe_C , with dashed lines showing amplitude equation predictions [Eqs. (26)

and (27)]. The data confirm the two predicted bifurcation types: at small Pe_C (blue and green curves), \tilde{v} increases continuously from zero (infinite-period bifurcation), while at large Pe_C (orange curves), \tilde{v} jumps discontinuously (Hopf bifurcation). The critical α decreases with Pe_C as predicted. Additionally, at a constant Pe_C (constant particle diffusivity M_0), increasing α by decreasing chemical diffusivity first increases and then decreases the velocity \tilde{v} , vanishing as $\tilde{v} \sim \alpha^{-1/2}$ when $\alpha \rightarrow \infty$, just as predicted by the theory [Eqs. (21) and (22)]. Some of the lines also feature a second discontinuous jump, which can be attributed to a morphological change from stripes to dots (e.g., as seen in Fig. S3). Stripes are preferred at large Pe_C and small α while dots are found at small Pe_C and large α .

Fig. 6(c) shows that the pattern amplitude R_ϕ increases with increasing α and decreasing Pe_C , indicating stronger phase separation when chemotaxis and chemical diffusion are slow—consistent with the competition between MIPS clustering and chemotactic dispersal. For small Pe_C (blue and green curves), the amplitude remains constant when the pattern is stationary ($\alpha < \alpha_c$) and increases continuously with increasing $\alpha > \alpha_c$. For large Pe_C (orange curves), the amplitude grows continuously from zero beyond the Hopf bifurcation point.

To further distinguish different bifurcation types at small and large Pe_C , we investigate the scaling of velocity and amplitude. As shown in Fig. 6(d-f), we observe the predicted scaling of velocity and pattern amplitude near critical points. In the infinite-period regime ($\text{Pe}_C < 0.917$), when $\alpha > \alpha_c$, velocities at different Pe_C collapse onto the universal curve $\tilde{v} \cdot \alpha \cdot \text{Pe}_C^{-1/2} = \sqrt{\text{Da} \cdot \tilde{c}_0 \phi_0 (\alpha - \alpha_c)}$ [Eq. (26)], as shown by the black dashed line in Fig. 6(d). In the supercritical Hopf regime ($\text{Pe}_C > 0.917$), when $\alpha > \alpha_c$, amplitudes at different Pe_C increases continuously from zero with increasing α and is independent of Pe_C [Fig. 6(e)], in good agreement with the analytical prediction [Eq. (28)]. The traveling wave speed jumps from 0 to a finite value when $\alpha = \alpha_c$ as shown in Fig. 6(b). Fig. 6(f) shows excellent agreement between the simulated and theoretically predicted [Eq. (29)] critical α_c across the full Pe_C range, with the vertical dashed line marking the regime boundary.

Altogether, these results show that the amplitude equation analysis of the traveling wave solution based on the weakly nonlinear model provides a strikingly good agreement with the simulations over all ranges of α and Pe_C , despite the fact that the majority of the observed patterns are traveling dots, and the full nonlinear model is solved in the simulations. We also find excellent agreement between the results of the amplitude equations and simulations in 1D (where the dot patterns do not exist) [§S3 B 2].

Spiral waves obey the same scaling laws. Beyond traveling stripes and dots, the oscillatory regime also supports spiral wave solutions—rotating patterns with topological defects at their cores [127]. By slowly ramping up α in Fig. 6, we deliberately avoided these to focus on trav-

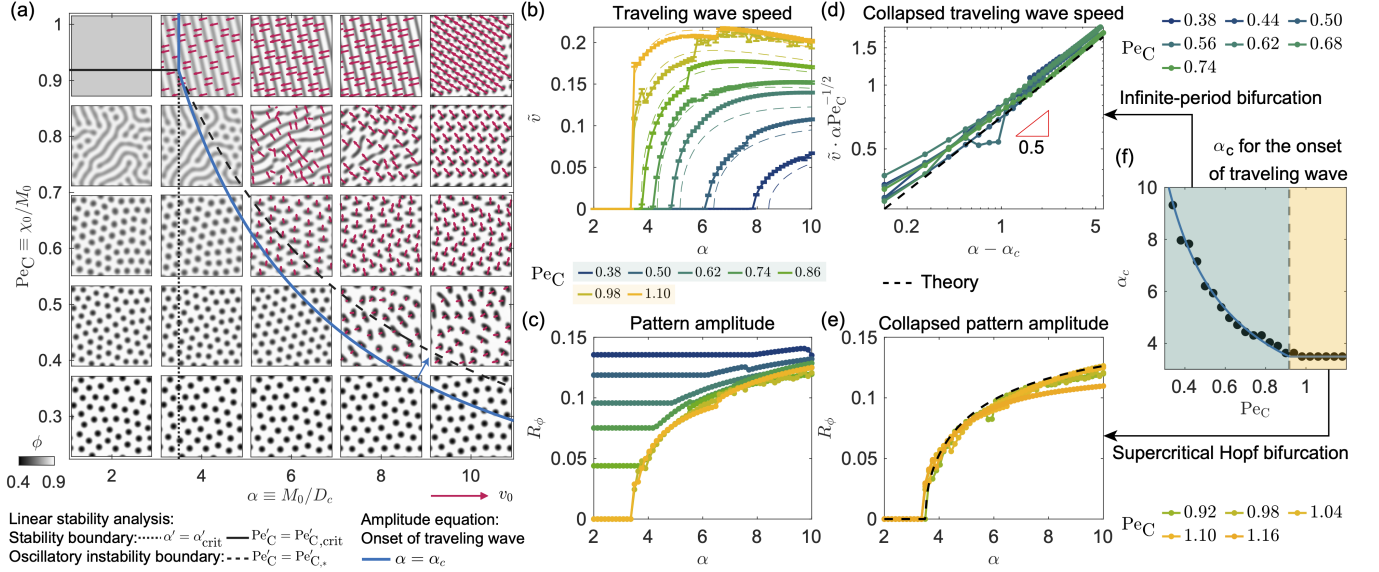


FIG. 6. **Amplitude equation predictions for oscillatory patterns agree quantitatively with simulations across the full $Pe_C - \alpha$ phase space.** (a) Simulations in $Pe_C - \alpha$ space ($Da = 0.5$, $Pe_R = 10^{-3}$, $\phi_0 = 0.8$ and $S_0/k = 1$) show traveling waves and dots emerging when α exceeds a critical value that decreases with Pe_C . Blue curve shows amplitude equation prediction [Eq. (29)], which accurately captures the onset of oscillatory patterns. Black dashed curve shows the linear stability prediction [Eq. S6], which overestimates the transition. Simulations at $\alpha = 2$ start from the uniform state with added noise as the initial condition. The value of α was ramped up for each Pe_C , i.e., simulations at $\alpha > 2$ use the final state of the previous α as the initial condition. Red arrows indicate pattern velocities; snapshots are at $t = 5 \times 10^3 t_0$. (b) Average normalized pattern speed $\tilde{v} = v/v_0$ as a function of α at different Pe_C . The speed is obtained from each simulation by averaging in space for each frame after the characteristic size of the pattern is less than 10% different from the final state, and then averaging in time to obtain the mean and standard deviation, as shown by the error bars. Dashed curves show the amplitude equation predictions [Eqs. (26) and (27)]. At small Pe_C (blue, green), velocity grows continuously from zero (infinite-period bifurcation); at large Pe_C (orange), velocity jumps discontinuously (supercritical Hopf bifurcation). (c) Pattern amplitude increases with α and decreases with Pe_C , reflecting stronger phase separation when chemotaxis and chemical diffusion are slow. The amplitude is obtained from each simulation as $R_{\phi, \text{sim}} = \sqrt{\int (\phi(\mathbf{x}) - \phi_0)^2 d\mathbf{x} / (2 \int d\mathbf{x})}$. (d) Velocity scaling collapse in infinite-period regime ($Pe_C < 0.917$) follows $\tilde{v} \cdot \alpha \cdot Pe_C^{-1/2} = \sqrt{Da \cdot \tilde{c}_0 \phi_0 (\alpha - \alpha_c)}$ (dashed line). (e) Amplitude scaling collapse in Hopf regime ($Pe_C > 0.917$): R_ϕ follows Eq. (28) (dashed line) independent of Pe_C . (f) Critical α_c for oscillatory onset matches analytical prediction [Eq. (29), blue curve] across all Pe_C ; vertical dashed line separates the two bifurcation regimes. Points are obtained from simulations by identifying the first α when $\tilde{v} > 0.01$.

eling dots and stripes. However, spirals can be observed by starting from a suitable initial condition. By starting from a spiral wave solution and systematically ramping up and down Pe_C , we obtain a family of spiral wave solutions shown in Fig. 7(a). As Pe_C increases, spiral velocity increases while the topological charge (number of arms) decreases. Remarkably, the system can sustain spirals with large topological charges, in contrast to examples in other reaction-diffusion systems where only spirals with charge ± 1 are stable [128]. At small Pe_C , the oscillatory solution becomes unstable, and so does the spiral. Below $Pe_C \approx 0.4$, spirals fragment into ripples before transitioning to a stationary pattern.

Using these solutions as initial conditions, we then ramp down α , and obtain spiral wave solutions at various α and Pe_C . Fig. 7(b) shows that in the infinite-period regime, the spiral wave speed collapses onto the same universal curve as traveling waves, $\tilde{v} \cdot \alpha \cdot Pe_C^{-1/2} = \sqrt{Da \cdot \tilde{c}_0 \phi_0 (\alpha - \alpha_c)}$, as predicted by

the amplitude equation. At small Pe_C , the spiral wave state remains stable as α decreases all the way until the pattern becomes stationary [Fig. S5]. The critical α_c for the onset of spiral waves [black dots in Fig. 7(c)] agrees well with Eq. (29) (blue curve) as well as the critical α_c for the onset of traveling stripes (gray dots). This remarkable agreement, despite spirals having fundamentally different topology, demonstrates the robustness of the amplitude equation predictions, as detailed further in §S3 B 3.

Transient dynamics before steady state. The above analysis focused on periodic steady states—ordered arrays of traveling stripes or dots moving coherently in a hexagonal lattice. However, before reaching steady state, the system undergoes rich transient dynamics with disordered oscillatory patterns. These transients are practically important because real systems, whether cells or synthetic colloids, experience continuous perturbations

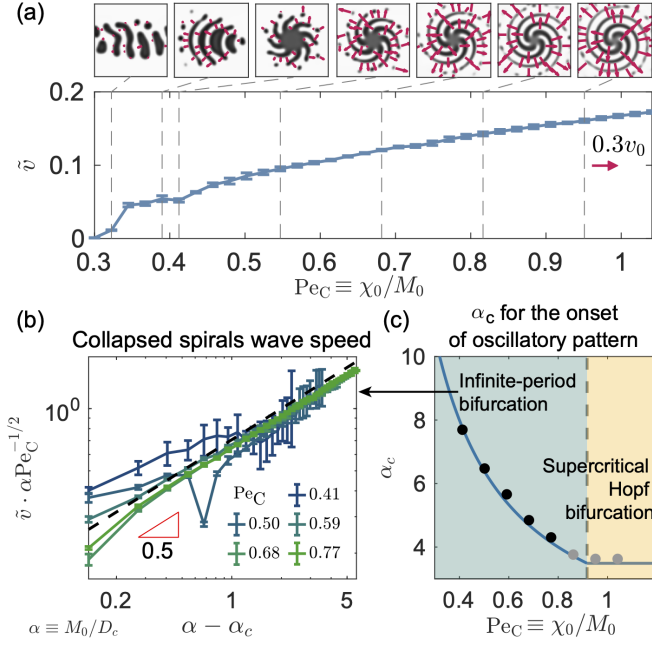


FIG. 7. **Spiral waves obey the same universal scaling laws as traveling waves despite their distinct topology.** (a) A family of spiral waves as a function of Pe_C at $\alpha = 10$ and $Da = 0.5$, $Pe_R = 10^{-3}$, $\phi_0 = 0.8$, and $S_0/k = 1$. Snapshots are taken at $t = 5 \times 10^3 t_0$; dashed vertical lines mark the corresponding Pe_C in the plot below, which shows the dependence of the normalized average speed \tilde{v} on Pe_C . Red arrows indicate the level set speed of the patterns with the same scale bar next to the snapshots. Velocities smaller than $0.005u_0$ are not shown. Increasing Pe_C increases spiral velocity and decreases topological charge (number of arms); below $Pe_C \approx 0.4$, spirals fragment into ripples before becoming stationary. (b) The spiral wave speed collapses onto the same curve as traveling stripes: $\tilde{v} \cdot \alpha \cdot Pe_C^{-1/2} = \sqrt{Da \cdot \tilde{c}_0 \phi_0 (\alpha - \alpha_c)}$ (dashed line), demonstrating universality of the infinite-period bifurcation. Pe_C values correspond to the black dots in (c). (c) The critical α_c for the onset of spiral waves (black dots) as a function of Pe_C matches the onset of traveling stripes (gray dots) and the analytical prediction from Eq. (29) (blue curve).

and may never reach true steady state. Hence, Fig. 8 illustrates the time evolution of four representative transient scenarios starting from homogeneous initial conditions:

Traveling waves with ordering. Fig. 8 (a) and Supplementary Movie S1 shows a representative example of traveling waves that span the entire domain. Initially, traveling waves form with random orientations in different spatial domains. The spatial correlation $C_\phi(\Delta\mathbf{x}, t) \equiv \langle \Delta\phi(\mathbf{x}, t), \Delta\phi(\mathbf{x} + \Delta\mathbf{x}, t) \rangle / \langle \Delta\phi(\mathbf{x}, t), \Delta\phi(\mathbf{x}, t) \rangle$ shows limited spatial extent. Over time, domains align and all waves propagate in the same direction, with the correlation extending in space, with a second peak approaching $l_p = 2\pi/(q_{\max})$, where $q_{\max} = \arg\max \text{Re } \omega_+(q)$ is the most unstable wavelength from linear stability analysis, confirming theoretical predictions.

Traveling dots with synchronization. Fig. 8(b) and Supplementary Movie S2 shows an example of traveling dots. Initially, dots that form as a result of spinodal decomposition move slowly, as seen from the evolution of the average speed $|\bar{\mathbf{u}}|$. They move in random directions while avoiding each other, undergoing fusion, fission, and dissolution. As a result, the polar order parameter $p \equiv |\bar{\mathbf{u}}|/|\mathbf{u}|$ [129], where $|\mathbf{u}|$ is the magnitude of the velocity averaged over all dots, is low. Eventually, dots synchronize: the speed increases to a steady state value, while the polar order parameter also increases, until eventually, the dots form a traveling hexagonal crystal.

Traveling stripes with alignment. Fig. 8(c) and Supplementary Movie S3 shows an example of short stripes that propagate along their minor axis. Initially, stripes move randomly, with longer stripes expanding concentrically and occasionally fragmenting. Over time, p approaches 1 as the stripes align and propagate coherently.

Intermittent bursts. In Fig. 8(d) and Supplementary Movie S4, dots also move and do not coarsen. However, in contrast with previous cases, polar order is never achieved. Instead, dots exhibit intermittent bursts of collective motion along transient local “pathways” but never achieve sustained order. Therefore, p fluctuates in time while the speed decays until the dots become stationary after $t/t_0 \approx 7 \times 10^4$.

These diverse morphologies span a spectrum: stripes extending across the system (large Pe_C and small α), to ellipsoids and circles (small Pe_C and large α), as seen throughout Figs. 8 (a)-(c), 6, and S3.

Oscillatory patterns in 3D. While we have focused on ABPs in 2D space, as is conventionally done, recent work has begun to explore both MIPS [81, 130, 131] and chemotaxis [38, 40, 122, 132] in 3D. Thus, we use the established 3D free energy model [Eq. (16)], which reproduces MIPS in 3D [23], to numerically simulate oscillatory traveling wave patterns that result from the competition between chemotaxis and MIPS. We focus on a $[50l_0, 50l_0, 50l_0]$ periodic domain with $Pe_R = 10^{-3}$, $Da = 1$, and $\alpha = 10$. Fig. 9 and the corresponding Supplementary Movies 5-8 shows three classes of 3D traveling patterns (opaque regions represent $\phi < 0.65$):

(a)-(b) *Traveling plane waves* ($\phi_0 = 0.55$, $Pe_C = 0.40$ and 0.71). Waves propagate as layered structures. Interestingly, different layers can interconnect while maintaining holes, creating complex 3D topology.

(c)-(d) *Traveling cylinders* ($\phi_0 = 0.58$, $Pe_C = 0.42$ and 0.80). Patterns resemble 2D dots extruded into the third dimension, forming elliptical cylinders with waviness along their axes.

(e)-(f) *Traveling spheroids* ($\phi_0 = 0.61$, $Pe_C = 0.37$ and 0.59). Ellipsoidal droplets travel through space. The aspect ratio depends on Pe_C , with traveling speed increasing with Pe_C .

In summary. Altogether, these results demonstrate that the amplitude equation approach successfully pre-

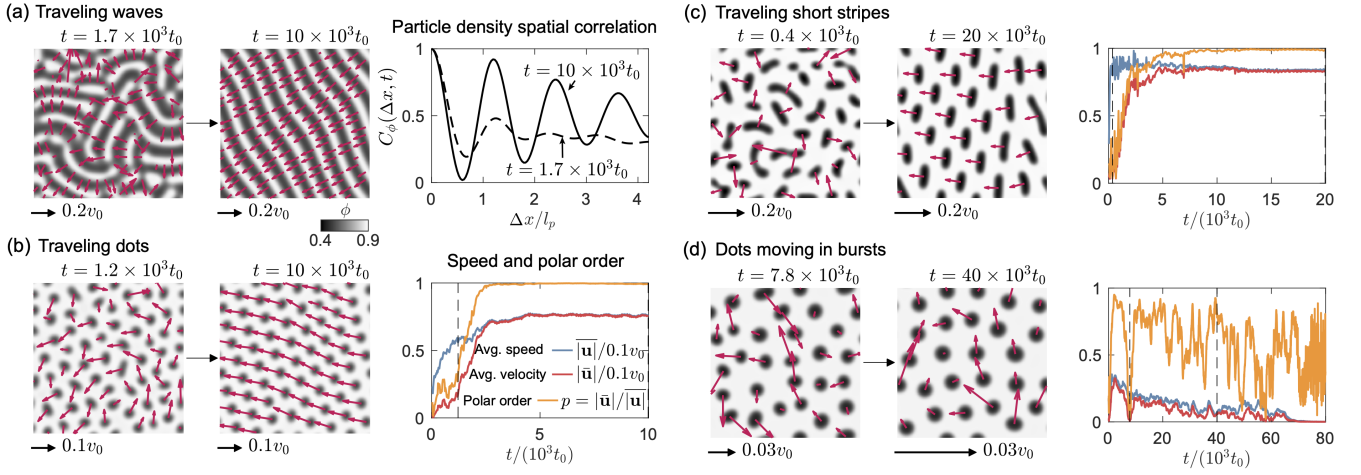


FIG. 8. **Transient dynamics before reaching steady state reveal diverse oscillatory morphologies and synchronization pathways.** Snapshots show particle density with red arrows indicating pattern velocity, defined by the level set velocity for stripes and the velocity of the center of mass for dots. All simulations start from uniform initial conditions with small perturbations. (a) Traveling waves spanning the domain initially form with random orientations in different regions, then align over time to propagate coherently. Spatial correlation $C_\phi(\Delta x, \Delta y = 0, t)$ in the horizontal direction (right) develops peaks at the predicted wavelength $l_p = 2\pi/q_{\max}$ where $q_{\max} = \arg\max \text{Re } \omega_+(q)$ is the most unstable wavenumber. Parameters: $\text{Pe}_R = 1.9 \times 10^{-3}$, $\phi_0 = 0.70$, $\text{Da} = 0.2$, $\alpha = 4$, $\text{Pe}_C = 1$. (b) Traveling dots initially move in random directions with low polar order $p \equiv |\bar{\mathbf{u}}|/|\bar{\mathbf{u}}|$, then synchronize into a hexagonal traveling crystal as speed and p increase. Plot to the right shows the time evolution of averaged speed $|\bar{\mathbf{u}}|$, magnitude of average velocity $|\bar{\mathbf{u}}|$, and polar order $p \equiv |\bar{\mathbf{u}}|/|\bar{\mathbf{u}}|$. The average is taken over all the patterns. Vertical dashed lines in the plots correspond to the time points of the two snapshots. Parameters: $\text{Pe}_R = 1.2 \times 10^{-3}$, $\phi_0 = 0.81$, $\text{Da} = 0.2$, $\alpha = 4$, $\text{Pe}_C = 1$. (c) Short traveling stripes gradually align, with polar order approaching unity as stripes propagate coherently along their minor axes. Parameters: $\text{Pe}_R = 1.4 \times 10^{-3}$, $\phi_0 = 0.79$, $\text{Da} = 0.56$, $\alpha = 15$, $\text{Pe}_C = 0.44$. (d) Dots exhibit intermittent bursts along transient pathways without achieving sustained order; polar order fluctuates and speed decays until dots become stationary. Parameters: $\text{Pe}_R = 2.4 \times 10^{-3}$, $\phi_0 = 0.80$, $\text{Da} = 0.5$, $\alpha = 10$, $\text{Pe}_C = 0.34$.

dicts not only when oscillatory patterns emerge, but also their velocities, amplitudes, and bifurcation types. The excellent quantitative agreement—despite analyzing traveling dots using plane wave solutions and despite the full nonlinear dynamics—demonstrates the power and robustness of weakly nonlinear theory for understanding chemotactic MIPS.

VII. ACTIVE BROWNIAN PARTICLES WITH DIFFERENT CHEMOTACTIC PROPERTIES

In § IV-VI, we studied the illustrative example of ABPs that consume a chemoattractant, for which chemotaxis drives particle dispersal and competes with MIPS clustering, resulting in the formation of complex patterns. However, active matter systems can exhibit diverse chemotactic behaviors: particles can produce rather than consume chemicals, and can respond to chemorepellents rather than chemoattractants. Moreover, many scenarios involve mixtures of particles with different chemotactic properties. Here, we extend our framework to encompass this broader landscape of chemotactic active matter.

Producer particles. We first consider particles that

produce rather than consume the chemical signal. We use the same free energy functional [Eq. (15)] as for consumers, and the same chemotactic sensing function $f(\tilde{c}) = \tilde{c}$. An illustrative model satisfying the requirements that $\partial_c R > 0$ and that there exists a homogeneous steady state is that the particles produce the chemical at a constant rate $g(\tilde{c}) = -g_0$ and that the chemical degrades via first-order kinetics $S(\tilde{c}) = k\tilde{c}$. At steady state, $\tilde{c}_0 = g_0\phi_0/k$. The governing equations [Eqs. (3) and (5)] are again linear in $\delta\tilde{c} = \tilde{c} - \tilde{c}_0$, so scaling the production rate g_0 is equivalent to scaling Pe_C proportionally. Therefore, without loss of generality, we fix $g_0/k = 1$.

Following the analysis in §IV, we generate the chemotactic MIPS phase diagram parameterized by $\{\phi, \text{Pe}_R, \text{Pe}_C\}$ for producer particles, again at $\text{Da} = 0.3$ and $\alpha = 1$ or 10 . The results are shown in Fig. 10(a)-(c) and (d)-(f), respectively. We also investigate the influence of varying Da in Fig. 11. While the stability and stationary/oscillatory instability boundaries are shifted compared to those of the consumer particles, taken altogether, our results show that producer particles exhibit qualitatively the same types of behavior as consumer particles, but with Pe_C having the opposite sign. This sign reversal reflects the fundamental relationship between chemical production/consumption and chemotactic response: producers ($g < 0$) of a chemorepellent

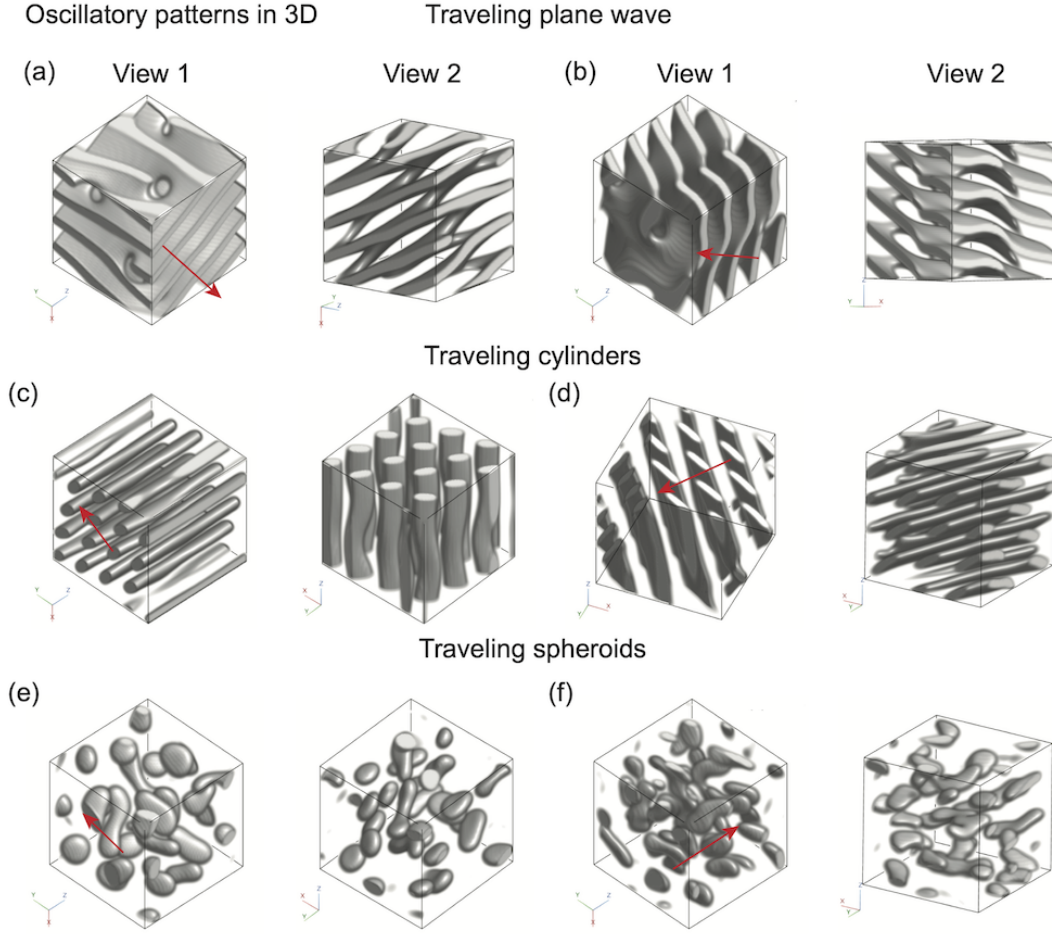


FIG. 9. Oscillatory patterns in 3D exhibit rich morphologies depending on volume fraction and chemotactic strength. Simulations in a $[50l_0, 50l_0, 50l_0]$ periodic domain at $Pe_R = 10^{-3}$, $Da = 1$, and $\alpha = 10$. Each row shows two viewing angles; snapshots are taken at $t = 10^4 t_0$. For clarity, gray regions show dilute phase ($\phi < 0.65$) and transparent regions show dense phase. (a-b) Traveling plane waves at $\phi_0 = 0.55$: layered structures propagate with interconnected topology and embedded voids. $Pe_C = 0.40$ in (a) and 0.71 in (b). (c-d) Traveling cylinders at $\phi_0 = 0.58$: elliptical cylinders with waviness along their axes, resembling 2D dots extruded in 3D. $Pe_C = 0.42$ in (c) and 0.80 in (d). (e-f) Traveling spheroids at $\phi_0 = 0.61$: ellipsoidal droplets with aspect ratio depending on Pe_C . $Pe_C = 0.37$ in (e) and 0.59 in (f). The red arrow indicates the direction in which the patterns move. See Supplemental Movies 5-10.

($\chi_0 < 0$) direct their motion away from the chemical they produce, causing them to disperse and suppressing MIPS, similar to consumers of a chemoattractant. By contrast, producers of a chemoattractant ($\chi_0 > 0$) direct their motion toward the chemical they produce, driving aggregation and enhancing MIPS, similar to consumers of a chemorepellent.

Our simulations confirm these predictions. At small α [Fig. 10(a)-(c)], when chemotactic dispersal is sufficiently strong (chemorepellent producers with $Pe_C < 0$), stationary dots and stripes emerge below the stability boundary, similar to the patterns in Fig. 3(a)-(c). These patterns arise because chemotaxis arrests coarsening, just as for consumers of a chemoattractant. For large α , when chemical diffusivity is sufficiently slow ($\alpha' > \alpha'_{\text{crit}}$, below the dashed red curve in Fig. 10(d)), phase separation al-

ways occurs. In the region where chemotactic dispersal is strong (Pe_C sufficiently negative, right of the colored surface), oscillatory instability emerges again. The simulations in panels (e)-(f) confirm traveling waves and dots in this regime, qualitatively matching the oscillatory patterns observed for consumer particles [Fig. 3(e)-(f)].

Conversely, when $Pe_C > 0$ (chemoattractant producers), chemotaxis enhances aggregation, expanding the phase separation region compared to non-chemotactic MIPS—as seen by comparing the instability regions at positive versus negative Pe_C in Fig. 10(a) and (d). This behavior is similar to that of consumers of a chemorepellent (§IV).

The dependencies on α and Da established in §IV for consumer particles also carry over to producer particles. As shown in Fig. 11, increasing Da (faster

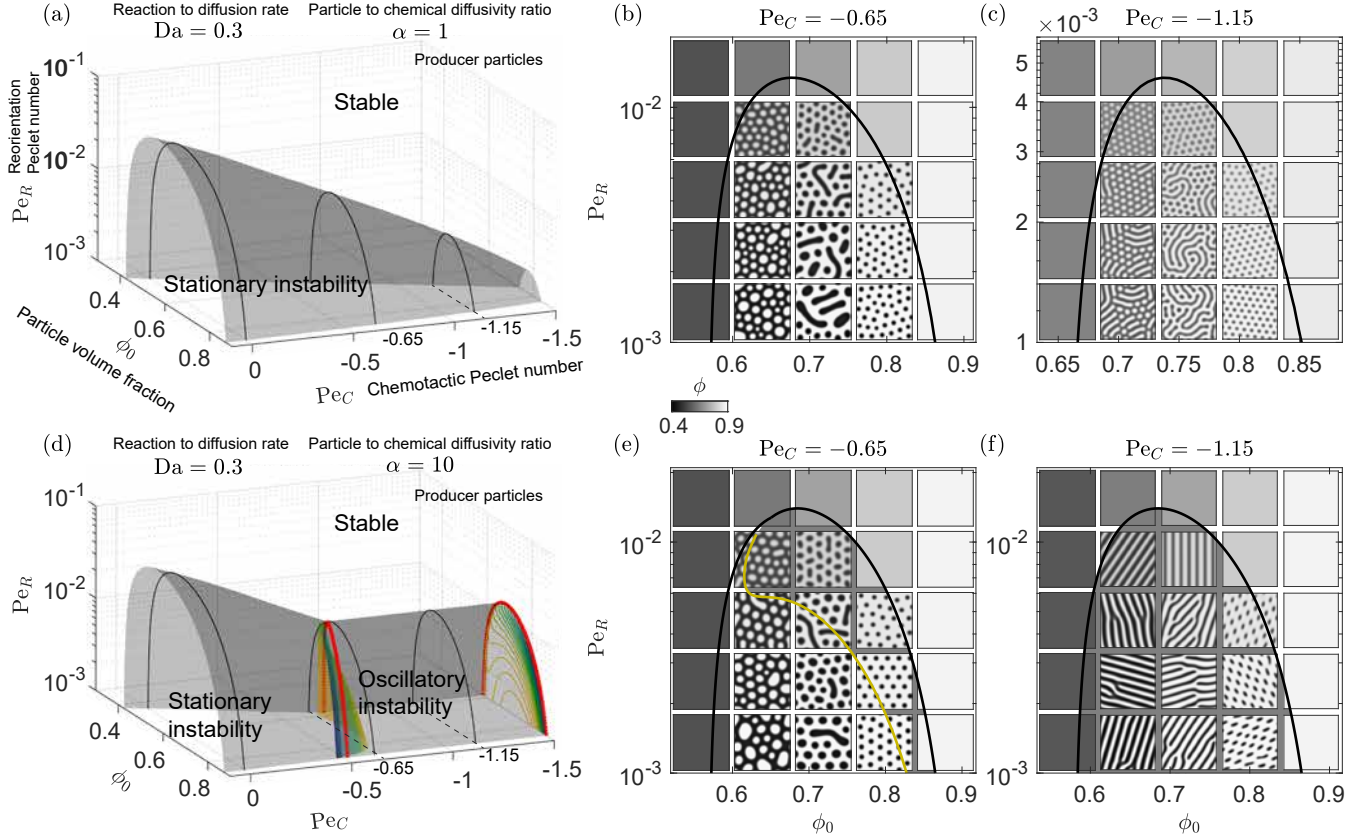


FIG. 10. **Producer particles exhibit similar behavior as consumers but with opposite sign of Pe_C .** Details are as in Fig. 3, but for chemotactic ABPs that produce a chemorepellent, and with the yellow replacing the green curve in (e). At small α (a), chemorepellent producers exhibit stationary dots and stripes below the stability boundary. At large α (d), oscillatory instability emerges when dispersal is sufficiently strong. (b-c, e-f) Cross-sections of the $Pe_R - \phi_0$ phase space at $Pe_C = -0.65$ and -1.15 confirm patterns analogous to the consumer case. Simulation snapshots at $t = 2 \times 10^4 t_0$ in $[100l_0, 100l_0]$ periodic domains confirm our predictions.

chemical uptake/production relative to diffusion) shrinks both the phase separation region and the oscillatory instability region [compare panels (a)-(b) and (c)-(d)]. Conversely, increasing α (slower chemical diffusion relative to particle mobility) expands these regions. The mathematical proof of these dependencies in §S1 A applies generally because it relies only on the structure of the dimensionless parameters α' , Da' , and Pe'_C , not on the specific signs of g and χ_0 .

Mixtures of chemotactic particles. Real ecosystems typically contain diverse populations—different bacterial species [107, 108, 133–135], or mixtures of synthetic colloids with different surface chemistries [50, 136, 137]—that may compete or cooperate through chemical signaling. Such mixtures can exhibit nonreciprocal interactions: particle A may attract B while B repels A, for instance. How does MIPS, which arises from particle motility, interact with these chemically-mediated interactions in mixtures of chemotactic particles? We address this question by extending our continuum model to mixtures of particles with different chemotactic properties. For

simplicity, we consider particles that share the same size, self-propulsion speed, and reorientation time—so if they were non-chemotactic, they would be indistinguishable and exhibit conventional single-component MIPS. The particles differ only in their chemical properties, i.e., in their chemical production/consumption rates and chemotactic responses.

Since the particles have identical active Brownian motion characteristics, the same effective free energy [Eq. (2)] applies, augmented by the entropy of mixing: $\tilde{G}[\phi_1, \dots, \phi_N] = \tilde{G}[\phi] + \int \phi \sum_i \zeta_i \ln \zeta_i dV$, where ϕ_i is the volume fraction of particles of type- i , $\phi = \sum_i \phi_i$ is the total volume fraction, and $\zeta_i = \phi_i/\phi$ is the fraction of type- i particles. The second term is the conditional entropy for mixing, where $\phi \sum_i \zeta_i \ln \zeta_i = \sum_i \phi_i \ln \phi_i - \phi \ln \phi$. The normalized chemical potential of type- i particles is then $\tilde{\mu}_i = \frac{\delta \tilde{G}}{\delta \phi_i} + \ln \zeta_i$. Using the 2D free energy model [Eq. (15)]: $\tilde{\mu}_i = \ln \phi_i + 1 - 2\phi - 0.3\phi^2 - \frac{4}{\pi} \cdot Pe_R \cdot \phi_m \left[\ln \left(1 - \frac{\phi}{\phi_m} \right) - \frac{\phi}{\phi_m - \phi} \right] - \kappa \nabla^2 \phi$. Each particle type obeys the continuity equation [Eq. (3)] with fluxes due to active Brownian motion and chemotaxis [Eqs. (1) and

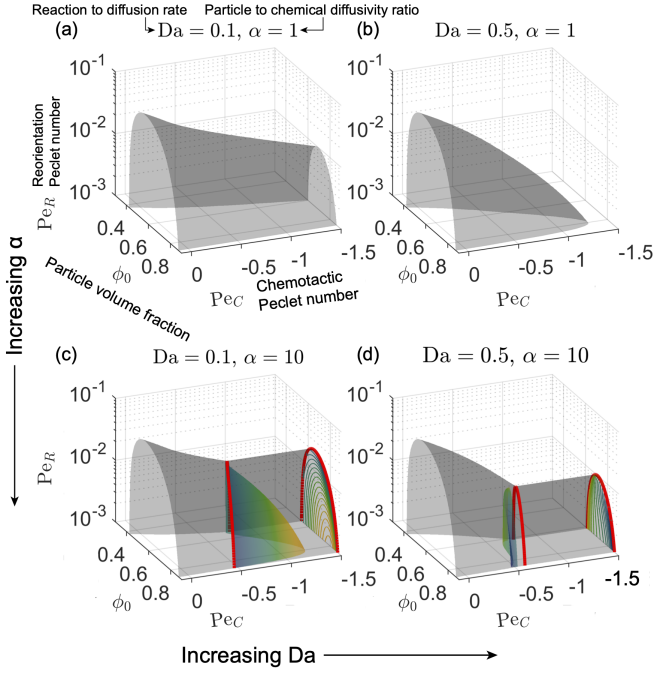


FIG. 11. **Increasing Da and α alter producer particle phase diagrams similar to consumers.** (a-d) Phase behavior at varying Da and α . Faster chemical production (larger Da) shrinks both phase separation and oscillatory regions; slower chemical diffusion (larger α) expands them. These trends are identical to consumer particles [Fig. 4], confirming that the competition between MIPS and chemotactic dispersal (regardless of whether via consumption or production) governs pattern formation.

(4), respectively]: $\frac{\partial \phi_i}{\partial t} = \nabla \cdot [M_0 \phi_i \nabla \tilde{\mu}_i - \chi_{0,i} \phi \nabla f_i(\tilde{c})]$, where $\chi_{0,i}$ and $f_i(\tilde{c})$ are the chemotactic coefficient and chemotactic sensing function of type- i particles, respectively. The chemical concentration then evolves in time according to $\frac{\partial \tilde{c}}{\partial t} = D_c \nabla^2 \tilde{c} - \sum_i R_i(c, \phi_i)$, where $R_i(c, \phi_i)$ is the net consumption rate of type- i particles.

As an illustrative example demonstrating effective non-reciprocal interactions mediated by chemotaxis, we consider two particle types ($i = A, B$) that both consume the same chemical ($R_A = R_B = k\tilde{c}\phi_i - S$) but have opposite chemotactic responses: particle A moves toward the chemical ($\chi_{0,A} = \chi_0 > 0$, chemoattractant consumer) while particle B moves away ($\chi_{0,B} = -\chi_0 < 0$, chemorepellent consumer). Both types have the same sensing function $f_i(\tilde{c}) = \tilde{c}$. The dimensionless parameters $\alpha \equiv M_0/D_c$, $Da \equiv k\kappa/D_c$, and $Pe_C \equiv \chi_0/M_0$ remain as defined previously. In this case, the interactions between type A and B particles are effectively non-reciprocal: Type A particles, by consuming the chemical, deplete it locally, creating a gradient that repels B particles away from A. Meanwhile, B particles also consume the chemical, but this depletion attracts A particles toward B. Thus, B is attracted to A (via chemotaxis toward depleted regions) while A is repelled by B (via chemotaxis away from depleted regions).

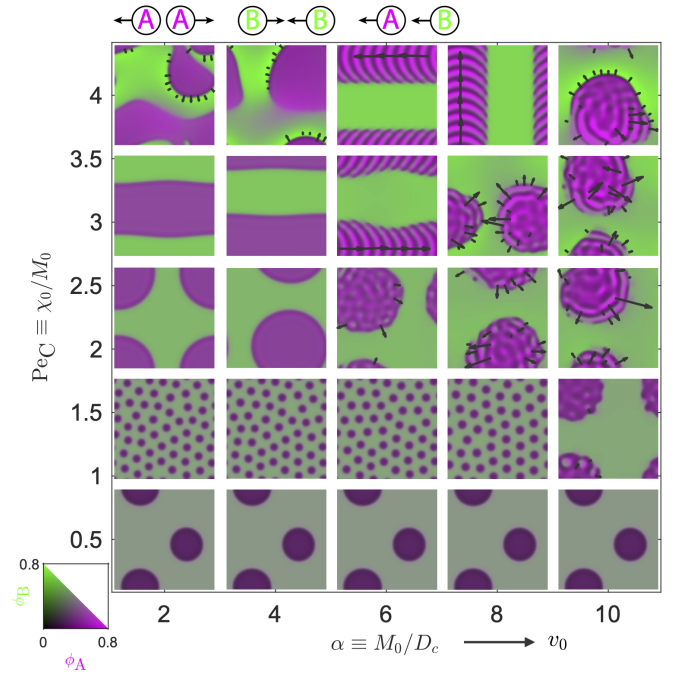


FIG. 12. **Nonreciprocal chemotactic interactions drive spatial segregation and selective oscillations in mixtures.** Phase diagram in $Pe_C - \alpha$ space shows mixtures of chemoattractant consumers (A, green) and chemorepellent consumers (B, magenta). Both types consume the same chemical but have opposite responses: $\chi_{0,A} = \chi_0 > 0$ and $\chi_{0,B} = -\chi_0 < 0$. At $Pe_C = 0$ (non-chemotactic), A and B mix uniformly in MIPS clusters. As Pe_C increases, chemotaxis drives segregation: A particles move away from B-rich regions while B particles are attracted to A-rich regions. At large α , oscillatory patterns emerge selectively in A-rich phases (which satisfy conditions for oscillatory instability) while B-rich phases remain stationary. Simulations are performed in a $[100l_0, 100l_0]$ periodic domain. Snapshots are taken at $t = 2 \times 10^4 t_0$. The initial condition is a uniform mixture of A and B particles where $\phi_A(\mathbf{x}) = \phi_{A0} = 0.3$ and $\phi_B(\mathbf{x}) = \phi_{B0} = 0.3$ with small perturbations and a uniform chemical concentration at $c_0 = S/[k(\phi_{A0} + \phi_{B0})]$. Other fixed parameters are $Pe_R = 10^{-3}$, $Da = 0.5$, $S/k = 1$. See Supplementary Movie S11.

Fig. 12 and Supplementary Movie S11 show simulations of this A-B mixture in the $Pe_C - \alpha$ phase space, starting from a uniform mixture with $\phi_A(\mathbf{x}) = \phi_{A0} = \phi_B(\mathbf{x}) = \phi_{B0} = 0.3$ and $Pe_R = 10^{-3}$, $Da = 0.5$, and $S/k = 1$. In the non-chemotactic limit ($Pe_C = 0$), conventional MIPS occurs and A and B particles are well-mixed in the dense phase—they are indistinguishable. As Pe_C increases, chemotaxis drives segregation of A and B into distinct phases, with the degree of segregation increasing with Pe_C . This segregation arises from the effective nonreciprocal interactions: A particles move away from B-rich regions while B particles are drawn toward A-rich regions. At large α (slow chemical diffusion), oscillatory patterns emerge as in the single-component case. In these oscillatory patterns, the A-rich phase forms waves

while the B-rich phase does not exhibit patterns. When the two phases are separated into two parallel domains, traveling waves emerge in the A-rich phase propagating in the direction normal to the A-B interface, consistent with the traveling waves that are found in consumers of chemoattractant discussed in §VI. When the A-rich phase is encapsulated within the B-rich phase and forms a circular domain, irregular waves that travel in different directions emerge within the A-rich phase, while the A-rich phase as a whole also moves in time-varying directions. At the upper left corner of the phase diagram, while there are no oscillatory patterns within either phase, the interface moves in time-varying directions.

In summary, the effective nonreciprocal interactions between particles with different chemotactic properties give rise to spatial segregation and selective oscillations, creating complex dynamic patterns not observed in either single-component systems or equilibrium mixtures. These findings provide a foundation for understanding pattern formation in diverse multi-component active matter systems, from bacterial ecosystems to engineered colloidal suspensions.

VIII. DISCUSSION

In this work, we have established a theoretical framework for understanding how collective chemotaxis fundamentally alters motility-induced phase separation. By combining linear stability analysis, amplitude equation theory, and numerical simulations, we demonstrated that the competition between MIPS clustering and chemotactic dispersal/aggregation generates a rich landscape of pattern-forming instabilities—from stationary dots and stripes to traveling waves and spirals. This landscape is governed by three new dimensionless parameters beyond those controlling standard MIPS (Pe_R, ϕ): the chemotactic Péclet number Pe_C comparing chemotactic to diffusive transport, the Damköhler number Da comparing chemical reaction to diffusion, and the ratio α comparing particle to chemical diffusivity.

Our central finding is that chemotaxis can either suppress or enhance MIPS depending on the sign of the product $\chi_0 g$. When particles consume chemoattractant or produce chemorepellent ($\chi_0 g > 0$), chemotaxis drives dispersal, opposing the clustering tendency of MIPS. In this regime, we find three distinct outcomes depending on the relative rates of chemical diffusion and uptake: (i) complete suppression of phase separation when chemotaxis is sufficiently fast (large Pe_C), (ii) arrested coarsening leading to stationary patterns of finite wavelength when chemical diffusion is fast (small α), or (iii) oscillatory instabilities generating traveling waves and spirals when chemical diffusion is slow (large α). Conversely, when particles produce chemoattractant or consume chemorepellent ($\chi_0 g < 0$), chemotaxis reinforces MIPS, expanding the phase separation region. This behavior is qualitatively universal: producer and consumer particles ex-

hibit the same phenomenology, differing only in the sign of Pe_C .

A key advance of our work is the quantitative prediction of the patterns that emerge. Using weakly nonlinear analysis, we derived analytical expressions for the amplitude, wavelength, and velocity of both stationary and oscillatory patterns. These predictions remain accurate even far from the linear stability boundary—remarkably, plane wave solutions quantitatively describe traveling dot arrays despite their fundamentally different topology. We identified four distinct bifurcation types governing transitions between different patterns: pitchfork bifurcations at the onset of stationary stripes, saddle-node bifurcations producing hysteresis between dots and uniform states, infinite-period bifurcations where traveling wave velocity grows continuously from zero, and supercritical Hopf bifurcations where velocity jumps discontinuously. The critical conditions for these bifurcations collapse onto universal scaling laws when expressed in terms of the reduced parameters α' , Da' , and Pe'_C .

Beyond single-component systems, we showed that mixtures of particles with different chemotactic properties exhibit effective nonreciprocal interactions that drive spatial segregation and selective pattern formation. These results reveal how chemical signaling can create complex dynamic patterns in multi-component active matter, with potential implications for understanding spatial organization in microbial consortia and designing programmable interactions in synthetic active colloids.

Our work also provides testable predictions for experiments. Using typical parameter values for motile bacteria— $Pe_R \sim 10^{-2}$ [5], $\alpha \lesssim 1$ [5, 34, 117], $Da \sim 10^2$ (with a typical chemical depletion length $\sqrt{D_c/k} \sim 1 \mu\text{m}$ [117] and persistence length $\sim 20 \mu\text{m}$ [138])—we estimate that chemotactic bacteria likely satisfy $\alpha' < \alpha'_{\text{crit}}$, placing them in the regime where chemotaxis suppresses MIPS (left of the dotted boundary in Fig. 2). Combined with substantial chemotactic response ($Pe_C \sim 10$ [34, 38, 117]), our results offer a possible explanation for why MIPS is rarely observed in bacterial collectives [5, 14] despite cells satisfying the motility criteria for phase separation. However, synthetic active colloids offer a versatile experimental platform to explore a broader range of the phase space mapped out in this paper. For example, by tuning swimming speed U_0 , catalyst concentration (controlling k), particle surface chemistry (controlling χ_0), and external chemical supply, one can systematically explore the full phase diagram of chemotactic MIPS. For example, in light-activated Janus colloids [9], spatiotemporal control of photocatalytic activity would enable dynamic tuning across the stationary-to-oscillatory transition, providing direct experimental access to the traveling waves, spirals, and transient dynamics predicted here.

Our study has several limitations that motivate future work. First, our continuum model provides a coarse-grained description of chemotactic ABPs over timescales much longer than the reorientation time τ_R and length

scales much larger than the persistence length $U_0\tau_R$. At shorter time and length scales or sufficiently large Pe_C , particle orientation dynamics may couple to chemotaxis in ways not captured by our model. Particle-based simulations could validate the continuum predictions in these regimes and identify when they break down, requiring one to model the dynamics of both ABP density and orientation fields. Second, we assumed Keller-Segel-type chemotaxis arising from translational drift and orientational bias. Real cells and synthetic colloids employ many other strategies to perform chemotaxis, such as by modulating run-and-tumble frequency [139], directional persistence [40], and sensing of higher-order gradients of chemical concentration [140]. Each of these could potentially couple differently to MIPS. Third, our Cahn-Hilliard-based free energy captures conventional MIPS but not additional phenomena like bubble formation observed in some active systems. Extending our analysis to more general models of ABPs (e.g., active model B+) [82, 141] could reveal new pattern types and bifurcation sequences. Our model chemotactic MIPS can also be extended to account for higher-order effects such as the anisotropic chemical reaction due to the asymmetry of Janus particles [58, 59] and the screening of the chemical field due to the volume occupied by the particles, especially in high-density clusters [60, 68]. These effects may also lead to novel coupling dynamics between particles and hence affect the pattern formation. Finally, real living systems also involve proliferation and death [142]. Incorporating these processes represents an important direction for understanding self-organization in living systems.

Nevertheless, our approach can be applied to other nonreciprocal active systems where pattern formation emerges from the interplay between phase separation and

directional fluxes [11, 83, 84, 86, 90, 91, 93–97, 143–150]. Examples include enzyme-enriched condensates exhibiting self-propulsion, epithelial tissues with mechanochemical feedback, and mixtures of active and passive particles with differential motility. In each case, the amplitude equation method could provide quantitative predictions for pattern onset, morphology selection, and dynamical transitions.

Our work thus establishes chemotactic MIPS as a paradigmatic example of pattern formation in nonreciprocal active matter. The interplay between self-propulsion, phase separation, and chemical signaling yields a rich array of new nonequilibrium phenomena. For bacterial collectives, our findings suggest that chemical communication profoundly shapes spatial structure, potentially regulating functions from nutrient access to collective migration. For synthetic microswimmers, the ability to program pattern formation through controlled chemical gradients opens possibilities for self-assembling materials with tunable structure and dynamics. By providing quantitative principles connecting microscopic parameters to emergent patterns, our framework bridges the gap between theory and experiment, enabling rational design of active materials and deeper understandings of self-organization in living systems.

Acknowledgements. We thank Alejandro Martínez-Calvo for valuable feedback on the manuscript. This work was supported by NSF Grants CBET-1941716, DMR-2011750, and EF-2124863, the Camille Dreyfus Teacher-Scholar Program, the Pew Biomedical Scholars Program, a Princeton Bioengineering Initiative (PBI²) Postdoctoral Fellowship, and a Harold W. Dodds Fellowship.

-
- [1] M. C. Marchetti, J. F. Joanny, S. Ramaswamy, T. B. Liverpool, J. Prost, M. Rao, and R. A. Simha, *Hydrodynamics of soft active matter*, *Reviews of Modern Physics* **85**, 1143 (2013).
 - [2] S. Ramaswamy, *The mechanics and statistics of active matter*, *Annual Review of Condensed Matter Physics* **1**, 323 (2010).
 - [3] T. Vicsek, A. Czirók, E. Ben-Jacob, I. Cohen, and O. Shochet, *Novel type of phase transition in a system of self-driven particles*, *Physical Review Letters* **75**, 1226 (1995).
 - [4] J. D. Murray, *Mathematical biology: I. An introduction* (Springer Science and Business Media., 2007).
 - [5] G. Liu, A. Patch, F. Bahar, D. Yllanes, R. D. Welch, M. C. Marchetti, S. Thutupalli, and J. W. Shaevitz, *Self-driven phase transitions drive myxococcus xanthus fruiting body formation*, *Physical Review Letters* **122**, 248102 (2019).
 - [6] R. Alert and X. Trepat, *Physical models of collective cell migration*, *The Annual Review of Condensed Matter Physics* is *Annu. Rev. Condens. Matter Phys.* **2020** **11**, 77 (2019).
 - [7] E. Scarpa and R. Mayor, *Collective cell migration in development*, *Journal of Cell Biology* **212**, 143 (2016).
 - [8] J. Elgeti, R. G. Winkler, and G. Gompper, *Physics of microswimmers - single particle motion and collective behavior: A review*, *Reports on Progress in Physics* **78**, 10.1088/0034-4885/78/5/056601 (2015).
 - [9] J. Palacci, S. Sacanna, A. P. Steinberg, D. J. Pine, and P. M. Chaikin, *Living crystals of light-activated colloidal surfers*, *Science* **339**, 936 (2013).
 - [10] I. Theurkauff, C. Cottin-Bizonne, J. Palacci, C. Ybert, and L. Bocquet, *Dynamic clustering in active colloidal suspensions with chemical signaling*, *Physical Review Letters* **108**, 268303 (2012).
 - [11] S. Palagi and P. Fischer, *Bioinspired microrobots*, *Nature Reviews Materials* **3**, 113 (2018).
 - [12] G. Gompper, R. G. Winkler, T. Speck, A. Solon, C. Nardini, F. Peruani, H. Löwen, R. Golestanian, U. B. Kaupp, L. Alvarez, T. Kiørboe, E. Lauga, W. C. K. Poon, A. DeSimone, S. Muiños-Landin, A. Fischer, N. A. Söker, F. Cichos, R. Kapral, P. Gaspard, M. Ripoll, F. Sagues, A. Doostmohammadi, J. M. Yeomans, I. S. Aranson, C. Bechinger, H. Stark, C. K.

- Hemelrijk, F. J. Nedelec, T. Sarkar, T. Aryaksama, M. Lacroix, G. Duclos, V. Yashunsky, P. Silberzan, M. Arroyo, and S. Kale, The 2020 motile active matter roadmap, *Journal of Physics: Condensed Matter* **32**, 193001 (2020).
- [13] M. R. Shaebani, A. Wysocki, R. G. Winkler, G. Gompper, and H. Rieger, Computational models for active matter, *Nature Reviews Physics* **2**, 181 (2020).
- [14] M. E. Cates and J. Tailleur, Motility-induced phase separation, *Annual Review of Condensed Matter Physics* **6**, 219 (2015).
- [15] G. S. Redner, M. F. Hagan, and A. Baskaran, Structure and dynamics of a phase-separating active colloidal fluid, *Physical Review Letters* **110**, 055701 (2013).
- [16] Y. Fily and M. C. Marchetti, Athermal phase separation of self-propelled particles with no alignment, *Physical Review Letters* **108**, 235702 (2012).
- [17] J. Bialké, T. Speck, and H. Löwen, Crystallization in a dense suspension of self-propelled particles, *Physical Review Letters* **108**, 168301 (2012).
- [18] M. E. Cates and J. Tailleur, When are active brownian particles and run-and-tumble particles equivalent? consequences for motility-induced phase separation, *EPL (Europhysics Letters)* **101**, 20010 (2013).
- [19] J. Tailleur and M. E. Cates, Statistical mechanics of interacting run-and-tumble bacteria, *Physical Review Letters* **100**, 218103 (2008).
- [20] J. Stenhammar, A. Tiribocchi, R. J. Allen, D. Marenduzzo, and M. E. Cates, Continuum theory of phase separation kinetics for active brownian particles, *Physical Review Letters* **111**, 145702 (2013).
- [21] J. Stenhammar, R. Wittkowski, D. Marenduzzo, and M. E. Cates, Light-induced self-assembly of active rectification devices, *Science Advances* **2**, 1 (2016).
- [22] S. Takatori, W. Yan, and J. Brady, Swim pressure: Stress generation in active matter, *Physical Review Letters* **113**, 028103 (2014).
- [23] S. C. Takatori and J. F. Brady, Towards a thermodynamics of active matter, *Physical Review E* **91**, 032117 (2015).
- [24] S. C. Takatori and J. F. Brady, Forces, stresses and the (thermo?) dynamics of active matter, *Current Opinion in Colloid and Interface Science* **21**, 24 (2016).
- [25] A. P. Solon, J. Stenhammar, R. Wittkowski, M. Kardar, Y. Kafri, M. E. Cates, and J. Tailleur, Pressure and phase equilibria in interacting active brownian spheres, *Physical Review Letters* **114**, 198301 (2015).
- [26] A. P. Solon, J. Stenhammar, M. E. Cates, Y. Kafri, and J. Tailleur, Generalized thermodynamics of phase equilibria in scalar active matter, *Physical Review E* **97**, 020602 (2018).
- [27] A. P. Solon, J. Stenhammar, M. E. Cates, Y. Kafri, and J. Tailleur, Generalized thermodynamics of motility-induced phase separation: phase equilibria, laplace pressure, and change of ensembles, *New Journal of Physics* **20**, 075001 (2018).
- [28] M. C. Marchetti, Y. Fily, S. Henkes, A. Patch, and D. Yllanes, Minimal model of active colloids highlights the role of mechanical interactions in controlling the emergent behavior of active matter, *Current Opinion in Colloid and Interface Science* **21**, 34 (2016).
- [29] E. F. Keller and L. A. Segel, Model for chemotaxis, *Journal of Theoretical Biology* **30**, 225 (1971).
- [30] H. C. Berg and D. A. Brown, Chemotaxis in escherichia coli analysed by three-dimensional tracking, *Nature* **239**, 500 (1972).
- [31] H. C. Berg, Chemotaxis in bacteria, *Annual Review of Biophysics and Bioengineering* **4**, 119 (1975).
- [32] J. Saragosti, V. Calvez, N. Bournaveas, A. Buguin, P. Silberzan, and B. Perthame, Mathematical description of bacterial traveling pulses, *PLoS Computational Biology* **6**, e1000890 (2010).
- [33] V. Sourjik and N. S. Wingreen, Responding to chemical gradients: bacterial chemotaxis, *Current Opinion in Cell Biology* **24**, 262 (2012).
- [34] X. Fu, S. Kato, J. Long, H. H. Mattingly, C. He, D. C. Vural, S. W. Zucker, and T. Emonet, Spatial self-organization resolves conflicts between individuality and collective migration, *Nature Communications* **9**, 2177 (2018).
- [35] J. Cremer, T. Honda, Y. Tang, J. Wong-Ng, M. Vergasola, and T. Hwa, Chemotaxis as a navigation strategy to boost range expansion, *Nature* **575**, 658 (2019).
- [36] M. Seyrich, A. Palugniok, and H. Stark, Traveling concentration pulses of bacteria in a generalized keller–segel model, *New Journal of Physics* **21**, 103001 (2019).
- [37] S. Gude, E. Pinçe, K. M. Taute, A. B. Seinen, T. S. Shimizu, and S. J. Tans, Bacterial coexistence driven by motility and spatial competition, *Nature* **578**, 588 (2020).
- [38] T. Bhattacharjee, D. B. Amchin, J. A. Ott, F. Kratz, and S. S. Datta, Chemotactic migration of bacteria in porous media, *Biophys J* **120**, 3483 (2021).
- [39] Y. Bai, C. He, P. Chu, J. Long, X. Li, and X. Fu, Spatial modulation of individual behaviors enables an ordered structure of diverse phenotypes during bacterial group migration, *eLife* **10**, 10.7554/eLife.67316 (2021).
- [40] T. Bhattacharjee, D. B. Amchin, R. Alert, J. A. Ott, and S. S. Datta, Chemotactic smoothing of collective migration, *eLife* , 1 (2022).
- [41] J. A. Moore-Ott, S. Chiu, D. B. Amchin, T. Bhattacharjee, and S. S. Datta, A biophysical threshold for biofilm formation, *eLife* **11**, 10.7554/eLife.76380 (2022).
- [42] H. Weyer, D. Muramatsu, and E. Frey, Coarsening dynamics of chemotactic aggregates, *Physical Review E* **112**, 054406 (2025).
- [43] P. J. V. Haastert and P. N. Devreotes, Chemotaxis: Signalling the way forward (2004).
- [44] J. R. Howse, R. A. L. Jones, A. J. Ryan, T. Gough, R. Vafabakhsh, and R. Golestanian, Self-motile colloidal particles: From directed propulsion to random walk, *Physical Review Letters* **99**, 048102 (2007).
- [45] M. Ibele, T. Mallouk, and A. Sen, Schooling behavior of light-powered autonomous micromotors in water, *Angewandte Chemie* **121**, 3358 (2009).
- [46] I. Buttinoni, G. Volpe, F. Kümmel, G. Volpe, and C. Bechinger, Active brownian motion tunable by light, *Journal of Physics: Condensed Matter* **24**, 284129 (2012).
- [47] S. Thutupalli, R. Seemann, and S. Herminghaus, Swarming behavior of simple model squirmers, *New Journal of Physics* **13**, 073021 (2011).
- [48] A. Zöttl and H. Stark, Emergent behavior in active colloids, *Journal of Physics: Condensed Matter* **28**, 253001 (2016).
- [49] J. L. Moran and J. D. Posner, Phoretic self-propulsion, *Annual Review of Fluid Mechanics* **49**, 511 (2017).
- [50] C. H. Meredith, A. C. Castonguay, Y.-J. Chiu, A. M.

- Brooks, P. G. Moerman, P. Torab, P. K. Wong, A. Sen, D. Velegol, and L. D. Zarzar, Chemical design of self-propelled janus droplets, *Matter* **5**, 616 (2022).
- [51] B. Liebchen and A. K. Mukhopadhyay, Interactions in active colloids, *Journal of Physics: Condensed Matter* **34**, 083002 (2022).
- [52] S. Michelin, E. Lauga, and D. Bartolo, Spontaneous autophoretic motion of isotropic particles, *Physics of Fluids* **25**, 061701 (2013).
- [53] Z. Izri, M. N. van der Linden, S. Michelin, and O. Dautchot, Self-propulsion of pure water droplets by spontaneous marangoni-stress-driven motion, *Physical Review Letters* **113**, 248302 (2014).
- [54] S. Michelin and E. Lauga, Phoretic self-propulsion at finite péclet numbers, *Journal of Fluid Mechanics* **747**, 572 (2014).
- [55] C. C. Maass, C. Krüger, S. Herminghaus, and C. Bahr, Swimming droplets, *Annual Review of Condensed Matter Physics* **7**, 171 (2016).
- [56] S. Lach, S. M. Yoon, and B. A. Grzybowski, Tactic, reactive, and functional droplets outside of equilibrium, *Chemical Society Reviews* **45**, 4766 (2016).
- [57] B. V. Hokmabad, J. Agudo-Canalejo, S. Saha, R. Golestanian, and C. C. Maass, Chemotactic self-caging in active emulsions, *Proceedings of the National Academy of Sciences* **119**, 10.1073/pnas.2122269119 (2022).
- [58] B. Liebchen, D. Marenduzzo, I. Pagonabarraga, and M. E. Cates, Clustering and pattern formation in chemorepulsive active colloids, *Physical Review Letters* **115**, 258301 (2015).
- [59] B. Liebchen, D. Marenduzzo, and M. E. Cates, Phoretic interactions generically induce dynamic clusters and wave patterns in active colloids, *Physical Review Letters* **118**, 268001 (2017).
- [60] O. Pohl and H. Stark, Dynamic clustering and chemotactic collapse of self-phoretic active particles, *Physical Review Letters* **112**, 238303 (2014).
- [61] F. Mohajerani, X. Zhao, A. Somasundar, D. Velegol, and A. Sen, A theory of enzyme chemotaxis: From experiments to modeling, *Biochemistry* **57**, 6256 (2018).
- [62] J. Agudo-Canalejo, P. Illien, and R. Golestanian, Phoresis and enhanced diffusion compete in enzyme chemotaxis, *Nano Letters* **18**, 2711 (2018).
- [63] A. Y. Jee, Y. K. Cho, S. Granick, and T. Tlusty, Catalytic enzymes are active matter, *Proceedings of the National Academy of Sciences of the United States of America* **115**, E10812 (2018).
- [64] S. Sengupta, K. K. Dey, H. S. Muddana, T. Tabouillot, M. E. Ibele, P. J. Butler, and A. Sen, Enzyme molecules as nanomotors, *Journal of the American Chemical Society* **135**, 1406 (2013).
- [65] J. Agudo-Canalejo, T. Adeleke-Larodo, P. Illien, and R. Golestanian, Enhanced diffusion and chemotaxis at the nanoscale, *Accounts of Chemical Research* **51**, 2365 (2018).
- [66] M. Feng and M. K. Gilson, Enhanced diffusion and chemotaxis of enzymes, *Annual Review of Biophysics* **49**, 87 (2020).
- [67] A. Aubret, M. Youssef, S. Sacanna, and J. Palacci, Targeted assembly and synchronization of self-spinning microgears (2018).
- [68] H. Stark, Artificial chemotaxis of self-phoretic active colloids: Collective behavior, *Accounts of Chemical Research* **51**, 2681 (2018).
- [69] B. Liebchen and H. Löwen, Synthetic chemotaxis and collective behavior in active matter, *Accounts of Chemical Research* **51**, 2982 (2018).
- [70] B. Liebchen and D. Levis, Collective behavior of chiral active matter: Pattern formation and enhanced flocking, *Physical Review Letters* **119**, 058002 (2017).
- [71] S. Saha, R. Golestanian, and S. Ramaswamy, Clusters, asters, and collective oscillations in chemotactic colloids, *Physical Review E* **89**, 062316 (2014).
- [72] S. Saha, S. Ramaswamy, and R. Golestanian, Pairing, waltzing and scattering of chemotactic active colloids, *New Journal of Physics* **21**, 063006 (2019).
- [73] L. Varga, A. Libal, C. J. O. Reichhardt, and C. Reichhardt, Active regimes for particles on resource landscapes, *Physical Review Research* **4**, 013061 (2022).
- [74] L. Varga, A. Libal, C. Reichhardt, and C. J. O. Reichhardt, Pattern formation and flocking for particles near the jamming transition on resource gradient substrates, *Physical Review E* **106**, 064602 (2022).
- [75] J. O’Byrne and J. Tailleur, Lamellar to micellar phases and beyond: When tactic active systems admit free energy functionals, *Physical Review Letters* **125**, 10.1103/PhysRevLett.125.208003 (2020).
- [76] A. Ziepeke, I. Maryshev, I. S. Aranson, and E. Frey, Multi-scale organization in communicating active matter, *Nature Communications* **13**, 6727 (2022).
- [77] F. Fadda, D. A. Matoz-Fernandez, R. van Roij, and S. Jabbari-Farouji, The interplay between chemophoretic interactions and crowding in active colloids, *Soft Matter* **19**, 2297 (2023).
- [78] H. Zhao, A. Košmrlj, and S. S. Datta, Chemotactic motility-induced phase separation, *Physical Review Letters* **131**, 118301 (2023).
- [79] T. Speck, J. Bialke, A. M. Menzel, and H. Lowen, Effective cahn-hilliard equation for the phase separation of active brownian particles, *Physical Review Letters* **112**, 218304 (2014).
- [80] T. Speck, A. M. Menzel, J. Bialké, and H. Löwen, Dynamical mean-field theory and weakly non-linear analysis for the phase separation of active brownian particles, *The Journal of Chemical Physics* **142**, 224109 (2015).
- [81] J. Stenhammar, D. Marenduzzo, R. J. Allen, and M. E. Cates, Phase behaviour of active brownian particles: The role of dimensionality, *Soft Matter* **10**, 1489 (2014).
- [82] E. Tjhung, C. Nardini, and M. E. Cates, Cluster phases and bubbly phase separation in active fluids: Reversal of the ostwald process, *Physical Review X* **8**, 031080 (2018).
- [83] Z. You, A. Baskaran, and M. C. Marchetti, Nonreciprocity as a generic route to traveling states, *Proceedings of the National Academy of Sciences* **117**, 19767 (2020).
- [84] S. Saha, J. Agudo-Canalejo, and R. Golestanian, Scalar active mixtures: The nonreciprocal cahn-hilliard model, *Physical Review X* **10**, 041009 (2020).
- [85] S. Saha and R. Golestanian, Effervescence in a binary mixture with nonlinear non-reciprocal interactions, *Nature Communications* **16**, 7310 (2025).
- [86] F. Brauns and M. C. Marchetti, Nonreciprocal pattern formation of conserved fields, *Physical Review X* **14**, 021014 (2024).
- [87] V. Ouazan-Reboul, J. Agudo-Canalejo, and R. Golestanian, Non-equilibrium phase separation in mixtures of catalytically active particles: size dispersity and screen-

- ing effects, *The European Physical Journal E* **44**, 113 (2021).
- [88] F. Brauns, H. Weyer, J. Halatek, J. Yoon, and E. Frey, Wavelength selection by interrupted coarsening in reaction-diffusion systems, *Physical Review Letters* **126**, 104101 (2021).
- [89] D. Zwicker, R. Seyboldt, C. A. Weber, A. A. Hyman, and F. Jülicher, Growth and division of active droplets provides a model for protocells, *Nature Physics* **13**, 408 (2017).
- [90] L. Demarchi, A. Goychuk, I. Maryshev, and E. Frey, Enzyme-enriched condensates show self-propulsion, positioning, and coexistence, *Physical Review Letters* **130**, 128401 (2023).
- [91] A. Wysocki, R. G. Winkler, and G. Gompper, Propagating interfaces in mixtures of active and passive brownian particles, *New Journal of Physics* **18**, 123030 (2016).
- [92] R. Wittkowski, J. Stenhammar, and M. E. Cates, Nonequilibrium dynamics of mixtures of active and passive colloidal particles, *New Journal of Physics* **19**, 105003 (2017).
- [93] J. S. Bois, F. Jülicher, and S. W. Grill, Pattern formation in active fluids, *Physical Review Letters* **106**, 028103 (2011).
- [94] M. Radszuweit, S. Alonso, H. Engel, and M. Bär, Intracellular mechanochemical waves in an active poroelastic model, *Physical Review Letters* **110**, 138102 (2013).
- [95] S. Banerjee, K. J. Utuje, and M. C. Marchetti, Propagating stress waves during epithelial expansion, *Physical Review Letters* **114**, 228101 (2015).
- [96] C. A. Weber, C. H. Rycroft, and L. Mahadevan, Differential activity-driven instabilities in biphasic active matter, *Physical Review Letters* **120**, 248003 (2018).
- [97] S. Yin and L. Mahadevan, Contractility-induced phase separation in active solids, *Physical Review Letters* **131**, 148401 (2023).
- [98] F. Raßhofer, S. Bauer, A. Ziepeke, I. Maryshev, and E. Frey, Capillary wave formation in conserved active emulsions, *Physical Review Research* **7**, 043240 (2025).
- [99] W. J. M. Ridgway, M. P. Dalwadi, P. Pearce, and S. J. Chapman, Motility-Induced Phase Separation Mediated by Bacterial Quorum Sensing, *Physical Review Letters* **131**, 228302 (2023).
- [100] H. Weyer, D. Muramatsu, and E. Frey, Chemotaxis-Induced Phase Separation, *Physical Review Letters* **135**, 208402 (2025).
- [101] D. Osmanović and E. Franco, Complex dynamics in reaction-phase separation systems, *Physical Review E* **111**, 025404 (2025).
- [102] A. Martínez-Calvo, N. S. Wingreen, and S. S. Datta, Pattern formation by bacteria-phage interactions, arXiv 10.1101/2023.09.19.558479 (2023).
- [103] E. Frey and H. Weyer, Pattern Formation Beyond Turing: Physical Principles of Mass-Conserving Reaction-Diffusion Systems, arXiv 10.48550/ARXIV.2512.12558 (2025).
- [104] J. Romano, M. K. Johnsrud, B. Mahault, and R. Golestanian, Non-reciprocal interactions between condensates in chemically active mixtures, arXiv 10.48550/ARXIV.2511.23425 (2025).
- [105] L. Hupe, J. M. Materska, D. Zwicker, R. Golestanian, B. Waclaw, and P. Bittihn, Phase separation in a mixture of proliferating and motile active matter, arXiv 10.48550/ARXIV.2506.05288 (2025).
- [106] J. Van Der Kolk, F. Raßhofer, R. Swiderski, A. Haldar, A. Basu, and E. Frey, Anomalous Collective Dynamics of Autochemotactic Populations, *Physical Review Letters* **131**, 088201 (2023).
- [107] J. Hu, D. R. Amor, M. Barbier, G. Bunin, and J. Gore, Emergent phases of ecological diversity and dynamics mapped in microcosms, *Science* **378**, 85 (2022).
- [108] M. Ghoul and S. Mitri, The ecology and evolution of microbial competition (2016).
- [109] M. E. Hibbing, C. Fuqua, M. R. Parsek, and S. B. Peterson, Bacterial competition: Surviving and thriving in the microbial jungle (2010).
- [110] C. Ratzke, J. Barrere, and J. Gore, Strength of species interactions determines biodiversity and stability in microbial communities, *Nature Ecology and Evolution* **4**, 376 (2020).
- [111] J. Bialké, H. Löwen, and T. Speck, Microscopic theory for the phase separation of self-propelled repulsive disks, *EPL (Europhysics Letters)* **103**, 30008 (2013).
- [112] M. E. Cates, D. Marenduzzo, I. Pagonabarraga, and J. Tailleur, Arrested phase separation in reproducing bacteria creates a generic route to pattern formation, *Proceedings of the National Academy of Sciences of the United States of America* **107**, 11715 (2010).
- [113] J. Bialké, J. T. Siebert, H. Löwen, and T. Speck, Negative interfacial tension in phase-separated active brownian particles, *Physical Review Letters* **115**, 1 (2015).
- [114] E. F. Keller and L. A. Segel, Initiation of slime mold aggregation viewed as an instability, *Journal of theoretical biology* **26**, 399 (1970).
- [115] E. F. Keller and L. A. Segel, Traveling bands of chemotactic bacteria: a theoretical analysis, *Journal of theoretical biology* **30**, 235 (1971).
- [116] J. D. Murray, *Mathematical Biology II: Spatial Models and Biomedical Applications*, edited by J. D. Murray, Vol. 18 (Springer New York, 2003).
- [117] R. Alert, A. Martínez-Calvo, and S. S. Datta, Cellular sensing governs the stability of chemotactic fronts, *Physical Review Letters* **128**, 148101 (2022).
- [118] H. Masoud and M. J. Shelley, Collective surfing of chemically active particles, *Physical Review Letters* **112**, 10.1103/PhysRevLett.112.128304 (2013).
- [119] E. O. Budrene and H. C. Berg, Complex patterns formed by motile cells of escherichia coli, *Nature* **349**, 630 (1991).
- [120] E. O. Budrene and H. C. Berg, Dynamics of formation of symmetrical patterns by chemotactic bacteria, *Nature* **376**, 49 (1995).
- [121] D. E. Woodward, R. Tyson, M. R. Myerscough, J. D. Murray, E. O. Budrene, and H. C. Berg, Spatio-temporal patterns generated by salmonella typhimurium, *Biophysical Journal* **68**, 2181 (1995).
- [122] T. Bhattacharjee and S. S. Datta, Confinement and activity regulate bacterial motion in porous media, *Soft Matter* **15**, 9920 (2019).
- [123] A. V. Narla, J. Cremer, and T. Hwa, A traveling-wave solution for bacterial chemotaxis with growth, *Proceedings of the National Academy of Sciences* **118**, 10.1073/pnas.2105138118 (2021).
- [124] M. C. Cross and P. C. Hohenberg, Pattern formation outside of equilibrium, *Reviews of Modern Physics* **65**, 851 (1993).
- [125] Q. Yu and A. Košmrlj, Pattern formation of lipid domains in bilayer membranes, *Soft Matter* **21**, 4288

- (2025).
- [126] S. H. Strogatz, *Nonlinear Dynamics and Chaos* (CRC Press, 2018).
- [127] N. Rana and R. Golestanian, Defect Solutions of the Nonreciprocal Cahn-Hilliard Model: Spirals and Targets, *Physical Review Letters* **133**, 078301 (2024).
- [128] P. S. Hagan, Spiral waves in reaction-diffusion equations, *SIAM Journal on Applied Mathematics* **42**, 762 (1982).
- [129] A. M. Menzel and H. Lowen, Traveling and resting crystals in active systems, *Physical Review Letters* **110**, 055702 (2013).
- [130] A. Wysocki, R. G. Winkler, and G. Gompper, Cooperative motion of active brownian spheres in three-dimensional dense suspensions, *EPL (Europhysics Letters)* **105**, 48004 (2014).
- [131] F. Turci and N. B. Wilding, Phase separation and multi-body effects in three-dimensional active brownian particles, *Physical Review Letters* **126**, 038002 (2021).
- [132] A. Martínez-Calvo, T. Bhattacharjee, R. K. Bay, H. N. Luu, A. M. Hancock, N. S. Wingreen, and S. S. Datta, Morphological instability and roughening of growing 3d bacterial colonies, *Proceedings of the National Academy of Sciences* **119**, 10.1073/pnas.2208019119 (2022).
- [133] A. Martínez-Calvo, C. Trenado-Yuste, H. Lee, J. Gore, N. S. Wingreen, and S. S. Datta, Interfacial Morphodynamics of Proliferating Microbial Communities, *Physical Review X* **15**, 011016 (2025).
- [134] S. Mitri, E. Clarke, and K. R. Foster, Resource limitation drives spatial organization in microbial groups, *ISME Journal* **10**, 1471 (2016).
- [135] O. Hallatschek, P. Hersen, S. Ramanathan, and D. R. Nelson, Genetic drift at expanding frontiers promotes gene segregation (2007).
- [136] J. Agudo-Canalejo and R. Golestanian, Active phase separation in mixtures of chemically interacting particles, *Physical Review Letters* **123**, 018101 (2019).
- [137] A. Sengupta, T. Kruppa, and H. Löwen, Chemotactic predator-prey dynamics, *Physical Review E - Statistical, Nonlinear, and Soft Matter Physics* **83**, 10.1103/PhysRevE.83.031914 (2011).
- [138] M. E. Cates, Diffusive transport without detailed balance in motile bacteria: does microbiology need statistical physics?, *Reports on Progress in Physics* **75**, 042601 (2012).
- [139] E. F. Keller and L. A. Segel, Initiation of slime mold aggregation viewed as an instability, *Journal of Theoretical Biology* **26**, 399 (1970).
- [140] S. Mahdisoltani, R. B. A. Zinati, C. Duclut, A. Gambassi, and R. Golestanian, Nonequilibrium polarity-induced chemotaxis: Emergent galilean symmetry and exact scaling exponents, *Physical Review Research* **3**, 013100 (2021).
- [141] R. Wittkowski, A. Tiribocchi, J. Stenhammar, R. J. Allen, D. Marenduzzo, and M. E. Cates, Scalar φ^4 field theory for active-particle phase separation, *Nature Communications* **5**, 4351 (2014).
- [142] O. Hallatschek, S. S. Datta, K. Drescher, J. Dunkel, J. Elgeti, B. Waclaw, and N. S. Wingreen, Proliferating active matter (2023).
- [143] P. Roca-Cusachs, R. Sunyer, and X. Trepát, Mechanical guidance of cell migration: lessons from chemotaxis, *Current Opinion in Cell Biology* **25**, 543 (2013).
- [144] A. Shellard and R. Mayor, All roads lead to directional cell migration, *Trends in Cell Biology* **30**, 852 (2020).
- [145] S. SenGupta, C. A. Parent, and J. E. Bear, The principles of directed cell migration, *Nature Reviews Molecular Cell Biology* **22**, 529 (2021).
- [146] R. Sunyer, V. Conte, J. Escribano, A. Elosegui-Artola, A. Labernadie, L. Valon, D. Navajas, J. M. García-Aznar, J. J. Muñoz, P. Roca-Cusachs, and X. Trepát, Collective cell durotaxis emerges from long-range intercellular force transmission, *Science* **353**, 1157 (2016).
- [147] R. Alert and J. Casademunt, Role of substrate stiffness in tissue spreading: Wetting transition and tissue durotaxis, *Langmuir* **35**, 7571 (2019).
- [148] D. J. Cohen, W. J. Nelson, and M. M. Maharbiz, Galvanotactic control of collective cell migration in epithelial monolayers, *Nature Materials* **13**, 409 (2014).
- [149] M. Mijalkov, A. McDaniel, J. Wehr, and G. Volpe, Engineering sensorial delay to control phototaxis and emergent collective behaviors, *Physical Review X* **6**, 011008 (2016).
- [150] Y. Zhang, D. S. Lee, Y. Meir, C. P. Brangwynne, and N. S. Wingreen, Mechanical frustration of phase separation in the cell nucleus by chromatin, *Physical Review Letters* **126**, 10.1103/PhysRevLett.126.258102 (2021).

Supplementary Information

CONTENTS

I.	Introduction	1
II.	Model	2
III.	General linear stability analysis	3
IV.	Phase diagram of chemotactic MIPS	6
V.	Stationary patterns	8
VI.	Oscillatory patterns	11
VII.	Active Brownian particles with different chemotactic properties	15
VIII.	Discussion	19
	References	20
S1.	Linear stability analysis	25
	A. Connecting the general linear stability analysis to specific models of the chemotactic ABPs	25
	B. Derivation of the oscillatory instability condition from linear stability analysis	26
S2.	Amplitude equation: Theory	27
	A. Stationary patterns	27
	1. Uniform solution	28
	2. Stripes	28
	3. Dots	29
	B. Oscillatory patterns	30
S3.	Amplitude equation: Comparison with simulation	31
	A. Stationary patterns	31
	1. Pattern hysteresis by ramping parameters	31
	2. Comparison with the full-model simulation	32
	B. Oscillatory patterns	32
	1. Traveling stripes and dots in 2D	32
	2. Traveling wave in 1D	33
	3. Spiral waves	34
S4.	Supplemental movies	35

S1. LINEAR STABILITY ANALYSIS

A. Connecting the general linear stability analysis to specific models of the chemotactic ABPs

The general stability analysis derived in the main text applies to arbitrary constitutive relations for chemical kinetics and chemotactic sensing. Here, we connect these general results to the specific models used throughout the main text. In particular, we summarize the functional forms of chemical reaction kinetics ($g(\tilde{c})$, $S(\tilde{c})$) for consumer and producer particles used in the main text in Table S1 as well as the relationship between dimensionless parameters (α' and α , Da' and Da , Pe'_C and Pe_C). The chemotactic sensing function is $f(\tilde{c}) = \tilde{c}$. With these relationships, we can readily convert the stability conditions $Da' \geq Da'_{\text{crit}}$ and $Pe'_C \geq Pe'_{C,\text{crit}}$ from the linear stability analysis to an expression written explicitly in terms of $\partial_\phi \tilde{\mu}_h$ as also shown in Table S1. Because $\tilde{\mu}_h$ depends linearly on Pe_C [Eqs. (15), (16)], we can then express the stability condition explicitly in terms of Pe_R and then study how the stability boundary shifts

in the $\text{Pe}_R - \phi_0$ phase diagram as α , Da and Pe_C varies. For example, based on the 2D chemical potential Eq. (15), we find

$$\text{Pe}_R = \frac{\pi}{4} \frac{(\phi - \phi_m)^2}{\phi_m(\phi - 2\phi_m)} \left(\frac{1}{\phi} - 2 - 0.6\phi - \partial_\phi \tilde{\mu}_h \right). \quad (\text{S1})$$

Substituting the expressions for the stability conditions in terms of $\partial_\phi \tilde{\mu}_h$ into Eq. (S1), we obtain the expression for $\text{Pe}_R - \phi_0$ relation at the stability boundary.

From the expression of $\text{Da}' \geq \text{Da}'_{\text{crit}}$ we see that

1. $\text{Da}' < \text{Da}'_{\text{crit}}$ corresponds to the region below the boundary of $\text{Da}' = \text{Da}'_{\text{crit}}$ in the $\text{Pe}_R - \phi_0$ phase diagram because $\text{Da}' < \text{Da}'_{\text{crit}}$ is equivalent to

$$\text{Pe}_R < \frac{\pi}{4} \frac{(\phi - \phi_m)^2}{\phi_m(\phi - 2\phi_m)} \left(\frac{1}{\phi} - 2 - 0.6\phi + \frac{2\phi_0 \sqrt{\alpha \text{Da} + 1}}{\alpha \phi_0} \right). \quad (\text{S2})$$

2. The boundary of $\text{Da}' = \text{Da}'_{\text{crit}}$ always lies within the spinodal region because $-\partial_\phi \tilde{\mu}_h = \frac{2\phi_0 \sqrt{\alpha \text{Da} + 1}}{\alpha \phi_0} > 0$.
3. The boundary of $\text{Da}' = \text{Da}'_{\text{crit}}$ is independent of Pe_C .
4. At a given Da and ϕ_0 , the boundary of $\text{Da}' = \text{Da}'_{\text{crit}}$ shifts upward with increasing α , because $\partial_\phi \tilde{\mu}_h$ (and hence Pe_R) increases.
5. At a given α and ϕ_0 , the boundary of $\text{Da}' = \text{Da}'_{\text{crit}}$ shifts downward with increasing Da , because $\partial_\phi \tilde{\mu}_h$ (and hence Pe_R) decreases.

From the expressions of $\text{Pe}'_C \geq \text{Pe}'_{C,\text{crit}}$ for consumers and producers, we see that

1. $\text{Pe}'_C < \text{Pe}'_{C,\text{crit}}$ corresponds to the region below the boundary of $\text{Pe}'_C = \text{Pe}'_{C,\text{crit}}$ in the $\text{Pe}_R - \phi_0$ phase diagram for the same reason as above.
2. The boundary of $\text{Pe}'_C = \text{Pe}'_{C,\text{crit}}$ always lies within the spinodal region because at the boundary $-\partial_\phi \tilde{\mu}_h > 0$.
3. The boundary of $\text{Pe}'_C = \text{Pe}'_{C,\text{crit}}$ is independent of α .
4. At a given Da and ϕ_0 , the boundary of $\text{Pe}'_C = \text{Pe}'_{C,\text{crit}}$ shifts downward with increasing Pe_C for consumers, because $\partial_\phi \tilde{\mu}_h$ (and hence Pe_R) decreases, while it shifts upward with increasing Pe_C for producers.
5. At a given Da and ϕ_0 , the boundary of $\text{Pe}'_C = \text{Pe}'_{C,\text{crit}}$ is independent of Da at small chemotactic dispersal rate or when chemotaxis leads to aggregation, specifically when $\text{Pe}_C < kS_0^{-1} \text{Da} \phi_0^3$ for consumers and $-\text{Pe}_C < kg_0^{-1} \text{Da}$ for producers. Otherwise at higher chemotactic dispersal rate, the boundary of $\text{Pe}'_C = \text{Pe}'_{C,\text{crit}}$ shifts downward with increasing Da because $\partial_\phi \tilde{\mu}_h$ (and hence Pe_R) decreases.

B. Derivation of the oscillatory instability condition from linear stability analysis

As described in the linear stability analysis in Sec. III, the condition for oscillatory instability is that there exists \tilde{q} for which $\text{tr}(\tilde{\mathbf{J}}) > 0$ and $\Delta < 0$. From Eq. (10), the roots of $\text{tr}(\tilde{\mathbf{J}}) = 0$ are

$$\tilde{q}_\pm^2 = \frac{1}{2\alpha'} \left(\alpha' - 1 \pm \sqrt{(\alpha' - 1)^2 - 4\alpha' \text{Da}'} \right). \quad (\text{S3})$$

$\text{tr}(\tilde{\mathbf{J}}) > 0$ when $\tilde{q}_- < \tilde{q} < \tilde{q}_+$. Therefore, the critical $\text{Pe}'_{C,*}$ above which unstable oscillatory mode emerges corresponds to when there exists a critical $\tilde{q}^* \in [\tilde{q}_-, \tilde{q}_+]$ for which $\Delta = 0$ and for all $\tilde{q} \in [\tilde{q}_-, \tilde{q}_+]$, $\Delta \geq 0$. As show in ref. [78], the critical wavenumber \tilde{q}^* can be either \tilde{q}_\pm , or \tilde{q}'_{lr} , which are the roots of Δ of multiplicity 2 ($\Delta(\tilde{q}_{lr}) = 0$, and $d\Delta/d\tilde{q}(\tilde{q}_{lr}) = 0$). \tilde{q}'_{lr} exists when $(\alpha' + 1)^2 - 12\alpha' \text{Da}' \geq 0$, and their expressions are given by

$$\tilde{q}'_{lr}{}^2 = \frac{1}{6\alpha'} \left(\alpha' + 1 \pm \sqrt{(\alpha' + 1)^2 - 12\alpha' \text{Da}'} \right). \quad (\text{S4})$$

TABLE S1. Functional forms of $g(\tilde{c})$, $S(\tilde{c})$, the relationship between α' and α , Da' and Da , Pe'_C and Pe_C , and the equivalent expressions for Eq. (12) and Eq. (13) written explicitly in terms of $\partial_\phi \tilde{\mu}_h$ for both consumers and producers. $h(x) = x$ when $0 < x < 1$, and $h(x) = 2\sqrt{x} - 1$ when $x > 1$.

Consumer		Producer
$g(\tilde{c}) = k\tilde{c}$		$g(\tilde{c}) = -g_0$
$S(\tilde{c}) = -S_0$		$S(\tilde{c}) = k\tilde{c}$
$\alpha' = \alpha\phi_0 \partial_\phi \tilde{\mu}_h $		$\alpha' = \alpha\phi_0 \partial_\phi \tilde{\mu}_h $
$\text{Da}' = \text{Da} \frac{\phi_0}{ \partial_\phi \tilde{\mu}_h }$		$\text{Da}' = \text{Da} \frac{1}{ \partial_\phi \tilde{\mu}_h }$
$\text{Pe}'_C = \text{Pe}_C \frac{1}{\phi_0^2 \partial_\phi \tilde{\mu}_h } \frac{S_0}{k}$		$\text{Pe}'_C = -\text{Pe}_C \frac{1}{ \partial_\phi \tilde{\mu}_h } \frac{g_0}{k}$
$\text{Da}' \geq \text{Da}'_{\text{crit}}$ [Eq. (12)] is equivalent to		
$-\partial_\phi \tilde{\mu}_h \leq \frac{2\phi_0\sqrt{\alpha\text{Da}+1}}{\alpha\phi_0}$		$-\partial_\phi \tilde{\mu}_h \leq \frac{2\sqrt{\phi_0\alpha\text{Da}+1}}{\alpha\phi_0}$
$\text{Pe}'_C \geq \text{Pe}'_{C,\text{crit}}$ [Eq. (13)] is equivalent to		
$-\partial_\phi \tilde{\mu}_h \leq \phi_0\text{Da} \cdot h\left(\frac{S_0\text{Pe}_C}{k\text{Da}\phi_0^3}\right)$		$-\partial_\phi \tilde{\mu}_h \leq \text{Da} \cdot h\left(-\frac{g_0\text{Pe}_C}{k\text{Da}}\right)$

Furthermore, if $\tilde{q}_- < \tilde{q}_l < \tilde{q}_+$, \tilde{q}^* is \tilde{q}_+ , \tilde{q}_- , or \tilde{q}_l , whichever makes $\Delta(\tilde{q}^*) = 0$ at the smallest Pe'_C , otherwise, \tilde{q}^* is \tilde{q}_+ or \tilde{q}_- .

The minimum Pe'_C at which $\Delta(\tilde{q}) = 0$ is given by

$$\text{Pe}_{C,\Delta=0}(\tilde{q}) = \frac{\alpha'}{4\tilde{q}^2\text{Da}'} \left[\tilde{q}^4 + \left(\sigma - \frac{1}{\alpha'} \right) \tilde{q}^2 - \frac{\text{Da}'}{\alpha'} \right]^2. \quad (\text{S5})$$

Defining $\text{Pe}'_{C,\pm} = \text{Pe}_{C,\Delta=0}(\tilde{q}_\pm)$ and $\text{Pe}'_{C,l} = \text{Pe}_{C,\Delta=0}(\tilde{q}_l)$, then the critical $\text{Pe}'_{C,*}$ of unstable oscillation is

$$\text{Pe}'_{C,*} = \begin{cases} \min\{\text{Pe}'_{C,+}, \text{Pe}'_{C,-}, \text{Pe}'_{C,l}\}, & \text{when } \tilde{q}_- < \tilde{q}_l < \tilde{q}_+ \text{ or equivalently } \text{Da}' < \frac{(\alpha'+1)^2}{12\alpha'}, \text{Da}' > 1 - \frac{2}{\alpha'}, \text{ and } \alpha' > 5 \\ \min\{\text{Pe}'_{C,+}, \text{Pe}'_{C,-}\}, & \text{otherwise} \end{cases} \quad (\text{S6})$$

S2. AMPLITUDE EQUATION: THEORY

In this section, we present details on deriving the morphologies of both stationary and oscillatory patterns (Secs. V and VI in the main text).

A. Stationary patterns

We start with the amplitude equations [Eq. (18) in the main text] with $N = 3$, which govern the dynamics of the complex amplitudes A_c and A_ϕ . It will be convenient to rescale space by $l_0 = \sqrt{\kappa}$ and rescale time by $\tau_0 = \kappa/D_c$ (which should not be confused with t_0 or τ_R in the main text). For the sake of simplicity, we drop the tilde notation for the rescaled variables. We express the amplitudes in the polar form $A_{\phi,n} = R_{\phi,n}e^{i\psi_n}$ and $A_{c,n} = R_{c,n}e^{i\theta_n}$ and introduce new phase variables $\Theta_i = \theta_i - \psi_i$ and $\Psi = \sum_{i=1}^3 \psi_i$. The dynamical equations for the moduli and phases of the amplitudes are

$$\frac{dR_{c,i}}{dt} = -(k_c^2 + \text{Da}\phi_0)R_{c,i} - \text{Da}c_0R_{\phi,i} \cos \Theta_i - \text{Da}[R_{c,i+1}R_{\phi,i+2} \cos(\Psi + \Theta_i + \Theta_{i+1}) + R_{c,i+2}R_{\phi,i+1} \cos(\Psi + \Theta_i + \Theta_{i+2})], \quad (\text{S7})$$

$$\frac{dR_{\phi,i}}{dt} = \alpha\phi_0k_c^2[(a - k_c^2)R_{\phi,i} + \text{Pe}_CR_{c,i} \cos \Theta_i - 2\gamma R_{\phi,i+1}R_{\phi,i+2} \cos \Psi - b(3R_{\phi,i}^2 + 6R_{\phi,i+1}^2 + 6R_{\phi,i+2}^2)R_{\phi,i}], \quad (\text{S8})$$

$$\frac{d\psi_i}{dt} = \alpha\phi_0k_c^2 \left(\text{Pe}_C \frac{R_{c,i}}{R_{\phi,i}} \sin \Theta_i + 2\gamma \frac{R_{\phi,i+1}R_{\phi,i+2}}{R_{\phi,i}} \sin \Psi \right), \quad (\text{S9})$$

$$\frac{d\theta_i}{dt} = \text{Da} \left(c_0 \frac{R_{\phi,i}}{R_{c,i}} \sin \Theta_i + \frac{R_{c,i+1}R_{\phi,i+2}}{R_{c,i}} \sin(\Psi + \Theta_i + \Theta_{i+1}) + \frac{R_{c,i+2}R_{\phi,i+1}}{R_{c,i}} \sin(\Psi + \Theta_i + \Theta_{i+2}) \right), \quad (\text{S10})$$

where the index i cycles through $i = 1, 2, 3$ and the dimensionless parameters are defined by $\text{Da} = \kappa k/D_c$, $\alpha = M_0/D_c$, and $\text{Pe}_C = \chi_0/M_0$. In the following, we consider the fixed points corresponding to the uniform, stripe, and dot solutions. The stability of these solutions is determined from the Jacobian of the amplitude equations evaluated at the fixed points.

1. Uniform solution

The uniform solution is represented by $R_{c,i} = R_{\phi,i} = 0$, which is always a fixed point. To determine its stability, we consider the Jacobian of the R equations, which can be decomposed into three identical 2-by-2 matrices:

$$J_1 = \frac{\partial(\dot{R}_{c,1}, \dot{R}_{\phi,1})}{\partial(R_{c,1}, R_{\phi,1})} = \begin{pmatrix} -k_c^2 - \text{Da}\phi_0 & \text{Da}c_0 \\ -\alpha\phi_0 k_c^2 \text{Pe}_C & \alpha\phi_0 k_c^2 (a - k_c^2) \end{pmatrix}. \quad (\text{S11})$$

Hence, the stability condition is

$$\text{tr } J_1 = -k_c^2 - \text{Da}\phi_0 + \alpha\phi_0 k_c^2 (a - k_c^2) < 0, \quad (\text{S12})$$

$$\det J_1 = \alpha\phi_0 k_c^2 [-(a - k_c^2)(k_c^2 + \text{Da}\phi_0) + \text{Pe}_C \text{Da}c_0] > 0, \quad (\text{S13})$$

which simplifies to

$$a < \min \left(a_c, 2\sqrt{\frac{\text{Da}}{\alpha}} + \frac{1}{\alpha\phi_0} \right) = \min \left(2\sqrt{\text{Pe}_C \text{Da}c_0} - \text{Da}\phi_0, 2\sqrt{\frac{\text{Da}}{\alpha}} + \frac{1}{\alpha\phi_0} \right). \quad (\text{S14})$$

This condition is equivalent to the linear stability condition obtained for the general case in Sec. III of the main text. Indeed, mode coupling does not affect the stability of the uniform solution.

2. Stripes

For the stripe solution, we have $R_{\phi,1} = R_\phi$, $R_{c,1} = R_c$, and $R_{\phi,2} = R_{\phi,3} = R_{c,2} = R_{c,3} = 0$. The resulting amplitude equations are

$$\frac{dR_c}{dt} = -(k_c^2 + \text{Da}\phi_0)R_c - \text{Da}c_0 R_\phi \cos \Theta, \quad (\text{S15})$$

$$\frac{dR_\phi}{dt} = \alpha\phi_0 k_c^2 [(a - k_c^2)R_\phi + \text{Pe}_C R_c \cos \Theta - 3bR_\phi^3], \quad (\text{S16})$$

$$\frac{d\psi}{dt} = \alpha\phi_0 k_c^2 \text{Pe}_C \frac{R_c}{R_\phi} \sin \Theta, \quad (\text{S17})$$

$$\frac{d\theta}{dt} = \text{Da}c_0 \frac{R_\phi}{R_c} \sin \Theta. \quad (\text{S18})$$

From the last two equations, we have $\sin \Theta = 0$ and thus $\Theta = 0$ or π . However, only $\Theta = \pi$ is the physical solution as the first equation leads to

$$\frac{R_c}{R_\phi} = \frac{\text{Da}c_0}{k_c^2 + \text{Da}\phi_0} (-\cos \Theta) > 0 \Rightarrow \cos \Theta = -1. \quad (\text{S19})$$

Therefore, the ϕ and c fields are in antiphase. Substituting this into the second equation gives both amplitudes:

$$R_\phi = \frac{1}{\sqrt{3b}} \sqrt{a - k_c^2 - \frac{\text{Da}\text{Pe}_C c_0}{k_c^2 + \text{Da}\phi_0}}, \quad R_c = \frac{\text{Da}c_0}{k_c^2 + \text{Da}\phi_0} R_\phi. \quad (\text{S20})$$

Therefore, the maximum amplitude is reached when $k_c^2 = \sqrt{\text{Da}\text{Pe}_C c_0} - \text{Da}\phi_0$. The stripe solution only exists when $a > a_c \equiv 2\sqrt{\text{Da}\text{Pe}_C c_0} - \text{Da}\phi_0$.

The stability is governed by the 6-by-6 Jacobian $J = \frac{\partial \dot{R}}{\partial R}$, which decomposes into a 2-by-2 matrix J_1 (describing stability along the wavevector) and a 4-by-4 matrix J_2 (describing stability in the other two directions):

$$J_1 = \frac{\partial(\dot{R}_{c,1}, \dot{R}_{\phi,1})}{\partial(R_{c,1}, R_{\phi,1})} = \begin{pmatrix} -k_c^2 - \text{Da}\phi_0 & \text{Da}c_0 \\ -\alpha\phi_0 k_c^2 \text{Pe}_C & \alpha\phi_0 k_c^2 (a - k_c^2 - 9bR_\phi^2) \end{pmatrix}, \quad (\text{S21})$$

$$J_2 = \frac{\partial(\dot{R}_{c,2}, \dot{R}_{c,3}, \dot{R}_{\phi,2}, \dot{R}_{\phi,3})}{\partial(R_{c,2}, R_{c,3}, R_{\phi,2}, R_{\phi,3})} = \begin{pmatrix} -k_c^2 - \text{Da}\phi_0 & \text{Da}R_\phi & \text{Da}c_0 & \text{Da}R_c \\ \text{Da}R_\phi & -k_c^2 - \text{Da}\phi_0 & \text{Da}R_c & \text{Da}c_0 \\ -\alpha\phi_0 k_c^2 \text{Pe}_C & 0 & \alpha\phi_0 k_c^2 (a - k_c^2 - 6bR_\phi^2) & \alpha\phi_0 k_c^2 \cdot 2\gamma R_\phi \\ 0 & -\alpha\phi_0 k_c^2 \text{Pe}_C & \alpha\phi_0 k_c^2 \cdot 2\gamma R_\phi & \alpha\phi_0 k_c^2 (a - k_c^2 - 6bR_\phi^2) \end{pmatrix}. \quad (\text{S22})$$

The eigenvalues of the Jacobian are computed numerically to determine the stability boundary of the stripes, which are shown in Fig. 5 in the main text.

The above analysis is valid for $\alpha < \alpha_c = \max \left\{ \frac{4}{\text{Pe}_C c_0}, \frac{1}{a^2} \left(\sqrt{\text{Da}} + \sqrt{\text{Da} + a\phi_0^{-1}} \right)^2 \right\}$ [Eq. (29) in the main text], where the pattern remains stationary. Oscillatory patterns emerge at large α , which will be discussed in the next section.

3. Dots

The dots pattern is represented by $R_{c,1} = R_{c,2} = R_{c,3} = R_c$ and $R_{\phi,1} = R_{\phi,2} = R_{\phi,3} = R_\phi$. The equations for the phases are

$$\frac{d\psi_1}{dt} = \alpha\phi_0 k_c^2 \left(\text{Pe}_C \frac{R_c}{R_\phi} \sin \Theta_1 + 2\gamma R_\phi \sin \Psi \right), \quad (\text{S23})$$

$$\frac{d\theta_1}{dt} = \text{Da} \left(c_0 \frac{R_\phi}{R_c} \sin \Theta_1 + R_\phi (\sin(\Psi + \Theta_1 + \Theta_2) + \sin(\Psi + \Theta_1 + \Theta_3)) \right). \quad (\text{S24})$$

Since our analysis is in the vicinity of the bifurcation point, the amplitudes are small, but their ratios are finite. Thus, setting the leading order of the right-hand-side to zero leads to $\sin \Theta_1 = 0$ and therefore $\Theta_1 = 0$ or π . Similar to the stripe case, it can be shown that only the antiphase solution is physical $\Theta_{1,2,3} = \pi$, while the in-phase solution leads to negative R . The equations for R reduce to

$$\frac{dR_{c,i}}{dt} = -(k_c^2 + \text{Da}\phi_0) R_{c,i} + \text{Da}c_0 R_{\phi,i} - \text{Da} \cos \Psi (R_{c,i+1} R_{\phi,i+2} + R_{c,i+2} R_{\phi,i+1}), \quad (\text{S25})$$

$$\frac{dR_{\phi,i}}{dt} = \alpha\phi_0 k_c^2 [(a - k_c^2) R_{\phi,i} - \text{Pe}_C R_{c,i} - 2\gamma R_{\phi,i+1} R_{\phi,3} \cos \Psi - b(3R_{\phi,i}^2 + 6R_{\phi,i+1}^2 + 6R_{\phi,i+2}^2) R_{\phi,1}]. \quad (\text{S26})$$

From the first equation, we have

$$R_c = \frac{\text{Da}c_0 R_\phi}{k_c^2 + \text{Da}\phi_0 + 2\text{Da}R_\phi \cos \Psi}. \quad (\text{S27})$$

Substituting this into the second equation leads to

$$15bR_\phi^2 + 2\gamma R_\phi \cos \Psi - a + k_c^2 + \frac{\text{Pe}_C \text{Da}c_0}{k_c^2 + \text{Da}\phi_0 + 2\text{Da}R_\phi \cos \Psi} = 0. \quad (\text{S28})$$

Expanding to the quadratic order in R_ϕ , we find

$$15bR_\phi^2 + 2\gamma R_\phi \cos \Psi + \frac{\text{Pe}_C \text{Da}c_0}{k_c^2 + \text{Da}\phi_0} \left(-\frac{2\text{Da} \cos \Psi}{k_c^2 + \text{Da}\phi_0} R_\phi + \left(\frac{2\text{Da} \cos \Psi}{k_c^2 + \text{Da}\phi_0} \right)^2 R_\phi^2 \right) = a - k_c^2 - \frac{\text{Pe}_C \text{Da}c_0}{k_c^2 + \text{Da}\phi_0}. \quad (\text{S29})$$

The right hand side is maximized at $k_c^2 = \sqrt{\text{Da}\text{Pe}_C c_0} - \text{Da}\phi_0$, which simplifies the equation to

$$\left(15b + \frac{4\text{Da}^2 \cos^2 \Psi}{\sqrt{\text{Pe}_C \text{Da}c_0}} \right) R_\phi^2 + 2(\gamma - \text{Da}) \cos \Psi R_\phi = a - a_c. \quad (\text{S30})$$

In practice, $15b \gg \frac{4\text{Da}^2}{\sqrt{\text{Pe}_C \text{Da}c_0}}$, so the condition for the discriminant to be positive is

$$[(\gamma - \text{Da}) \cos \Psi]^2 + 15b(a - a_c) > 0 \Rightarrow a > a_c - \frac{(\gamma - \text{Da})^2 \cos^2 \Psi}{15b}. \quad (\text{S31})$$

Therefore, the minimum a that can sustain the dots pattern is $a_{\text{dots}} = a_c - \frac{(\gamma - \text{Da})^2}{15b}$, which is reached when $\cos \Psi = \text{sgn}(\text{Da} - \gamma)$ (the sign guarantees a positive amplitude). The corresponding R_ϕ is

$$R_\phi = \frac{1}{15b} \left(|\gamma - \text{Da}| + \sqrt{(\gamma - \text{Da})^2 + 15b(a - a_c)} \right) = \frac{1}{15b} \left(|\gamma - \text{Da}| + \sqrt{15b(a - a_{\text{dots}})} \right). \quad (\text{S32})$$

Therefore, at $a = a_{\text{dots}}$, the dots pattern emerges through a saddle-node bifurcation, where R_ϕ jumps from 0 to a finite value $\left(\frac{|\gamma - \text{Da}|}{15b}\right)$.

The stability of the fixed point is determined by numerically computing the eigenvalues of the Jacobian:

$$J = \frac{\partial(\dot{R}_c, \dot{R}_\phi)}{\partial(R_c, R_\phi)} = \begin{pmatrix} -k_c^2 - \text{Da}\phi_0 & \text{Da}R_\phi & \text{Da}R_\phi & \text{Da}c_0 & \text{Da}R_c & \text{Da}R_c \\ \text{Da}R_\phi & -k_c^2 - \text{Da}\phi_0 & \text{Da}R_\phi & \text{Da}R_c & \text{Da}c_0 & \text{Da}R_c \\ \text{Da}R_\phi & \text{Da}R_\phi & -k_c^2 - \text{Da}\phi_0 & \text{Da}R_c & \text{Da}R_c & \text{Da}c_0 \\ -\tilde{\alpha}\text{Pe}_C & 0 & 0 & \tilde{\alpha}(a - k_c^2 - 21bR_\phi^2) & \tilde{\alpha}(2\gamma R_\phi - 12bR_\phi^2) & \tilde{\alpha}(2\gamma R_\phi - 12bR_\phi^2) \\ 0 & -\tilde{\alpha}\text{Pe}_C & 0 & \tilde{\alpha}(2\gamma R_\phi - 12bR_\phi^2) & \tilde{\alpha}(a - k_c^2 - 21bR_\phi^2) & \tilde{\alpha}(2\gamma R_\phi - 12bR_\phi^2) \\ 0 & 0 & -\tilde{\alpha}\text{Pe}_C & \tilde{\alpha}(2\gamma R_\phi - 12bR_\phi^2) & \tilde{\alpha}(2\gamma R_\phi - 12bR_\phi^2) & \tilde{\alpha}(a - k_c^2 - 21bR_\phi^2) \end{pmatrix}. \quad (\text{S33})$$

where $\tilde{\alpha} = \alpha\phi_0 k_c^2$.

The stability of stationary pattern morphologies is summarized in the phase diagram in Fig. 5 in the main text.

B. Oscillatory patterns

As discussed in the main text, we consider the traveling wave solution $\phi(\mathbf{x}, t) - \phi_0 = R_\phi e^{i(k_c x + \omega t)} + \text{c.c.}$, and $\tilde{c} - \tilde{c}_0 = R_c e^{i(k_c x + \omega t + \Theta)} + \text{c.c.}$. The equations for the phases are

$$\frac{d\psi}{dt} = \omega = \alpha\phi_0 k_c^2 \text{Pe}_C \frac{R_c}{R_\phi} \sin \Theta, \quad (\text{S34})$$

$$\frac{d\theta}{dt} = \omega + \dot{\Theta} = \text{Da}c_0 \frac{R_\phi}{R_c} \sin \Theta. \quad (\text{S35})$$

Setting $\dot{\Theta} = 0$ and multiplying the two equations lead to $\omega^2 = \alpha\phi_0 k_c^2 \text{Pe}_C \text{Da}c_0 \sin^2 \Theta$. Hence, the (rescaled) phase velocity is

$$\tilde{v} = \frac{\omega}{k_c} = \sqrt{\text{Da}c_0 \phi_0 \alpha \text{Pe}_C} \sin \Theta. \quad (\text{S36})$$

The (dimensional) phase velocity is

$$v = \frac{l_0}{\tau_0} \frac{\omega}{k_c} = \frac{D_c}{\sqrt{\kappa}} \sqrt{\text{Da}c_0 \phi_0 \alpha \text{Pe}_C} \sin \Theta = v_0 \sqrt{\text{Da}c_0 \phi_0 \alpha^{-1} \text{Pe}_C} \sin \Theta, \quad (\text{S37})$$

where $v_0 = M_0/\sqrt{\kappa} = \alpha D_c/\sqrt{\kappa}$. This is the result in Eq. (21) of the main text.

Next, we consider the equations for $R_{c,\phi}$:

$$\frac{dR_c}{dt} = -(k_c^2 + \text{Da}\phi_0)R_c - \text{Da}c_0 R_\phi \cos \Theta = 0, \quad (\text{S38})$$

$$\frac{dR_\phi}{dt} = \alpha\phi_0 k_c^2 [(a - k_c^2)R_\phi + \text{Pe}_C R_c \cos \Theta - 3bR_\phi^3] = 0. \quad (\text{S39})$$

Combining Eq. (S34) and Eq. (S38), we have

$$\frac{R_c}{R_\phi} = \frac{\omega}{\alpha\phi_0 k_c^2 \text{Pe}_C \sin \Theta} = -\frac{\text{Da}c_0 \cos \Theta}{k_c^2 + \text{Da}\phi_0} \Rightarrow \cos \Theta = -\frac{k_c^2 + \text{Da}\phi_0}{k_c \sqrt{\text{Da}c_0 \alpha\phi_0 \text{Pe}_C}}, \quad (\text{S40})$$

which is Eq. (22) in the main text. A necessary condition is $\cos \Theta > -1$, which requires

$$k_c + \frac{\text{Da} \cdot \phi_0}{k_c} < \sqrt{\text{Da}c_0 \alpha\phi_0 \text{Pe}_C}, \quad (\text{S41})$$

which is Eq. (23) in the main text. Substituting $\frac{R_c}{R_\phi}$ into Eq. (S39) leads to

$$R_\phi = \frac{1}{\sqrt{3b}} \sqrt{a - k_c^2 - \frac{\text{Pe}_C \text{Da}c_0}{k_c^2 + \text{Da}\phi_0} \cos^2 \Theta}, \quad (\text{S42})$$

which is Eq. (24) in the main text.

The stability of the fixed points is determined from the Jacobian:

$$J = \frac{\partial(\dot{R}_c, \dot{R}_\phi)}{\partial(R_c, R_\phi)} = \begin{pmatrix} -(k_c^2 + \text{Da}\phi_0) & -\text{Da}c_0 \cos \Theta \\ \alpha\phi_0 k_c^2 \text{Pe}_C \cos \Theta & \alpha\phi_0 k_c^2 (a - k_c^2 - 9bR_\phi^2) \end{pmatrix}. \quad (\text{S43})$$

Stability requires $\det J > 0$ and $\text{tr} J < 0$: It can be shown that $\det J = 6bR_\phi^2 (k_c^2 + \text{Da}\phi_0) \cdot \alpha\phi_0 k_c^2 > 0$, while $\text{tr} J = 2\alpha\phi_0 k_c^2 \left(k_c^2 + \frac{\text{Da}}{k_c^2 \alpha} + \frac{1}{\alpha\phi_0} - a \right)$. Therefore, the stability condition is

$$k_c^2 + \frac{\text{Da}}{k_c^2 \alpha} + \frac{1}{\alpha\phi_0} < a, \quad (\text{S44})$$

which is Eq. (25) in the main text.

To summarize, the condition for a stable traveling wave is

- Existence: $\cos \Theta > -1 \Rightarrow k_c + \frac{\text{Da}\phi_0}{k_c} < \sqrt{\text{Da}c_0 \alpha\phi_0 \text{Pe}_C}$.
- Stability: $\text{tr} J < 0 \Rightarrow k_c^2 + \frac{\text{Da}}{k_c^2 \alpha} + \frac{1}{\alpha\phi_0} < a$.

The traveling waves can be destabilized by violating either of these conditions, which correspond to two different types of bifurcations: a Hopf bifurcation (when the stability condition is more restrictive) and an infinite-period bifurcation (when the existence condition is more restrictive). They are discussed in detail in the main text (Section VI).

S3. AMPLITUDE EQUATION: COMPARISON WITH SIMULATION

In this section, we provide further details on the comparison between the theoretical results of the amplitude equation and numerical simulations to supplement the main text.

A. Stationary patterns

1. Pattern hysteresis by ramping parameters

Fig. 5 in the main text shows simulations of the weakly nonlinear model, all of which start from the uniform state with the same random perturbation as the initial condition. Here, we ramp up and down the value of Da for each Pe_C , using the final state at the previous Da as the initial condition for the next Da value. The results are shown in Fig. S1. Comparing results of ramping up the value of Da [Fig. S1(a)] and ramping down the value of Da [Fig. S1(b)] in the region where both the dots and stripes solutions are stable, and in particular

From the rows of $\text{Pe}_C = 0.7$ and $\text{Pe}_C = 0.8$, we see that by ramping up the value of Da [Fig. S1(a)], at low Da , the pattern transitions from stripes to dots. In the region where both stripes and dots are stable, the pattern is dominated by stripes with a small number of dots in between. At higher Da , the system transitions from dot pattern to the uniform state. In the region where both dots and uniform state are stable, we observe a coexistence of dots

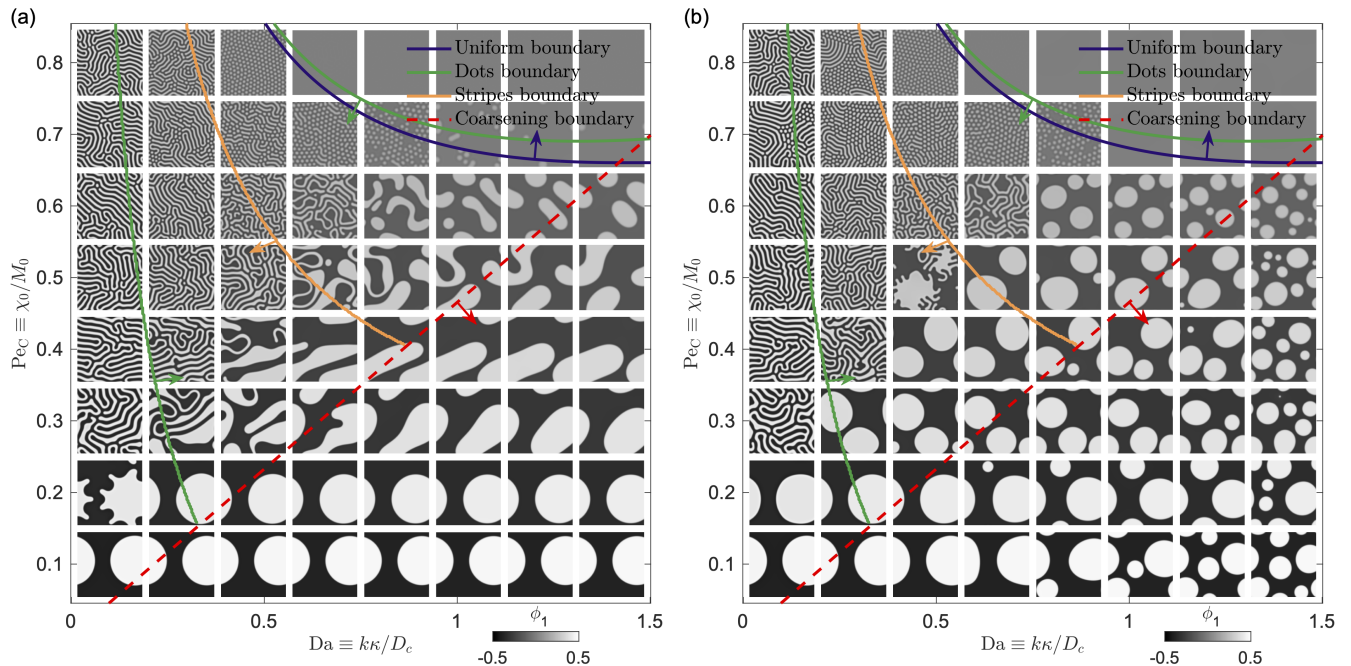


FIG. S1. Comparison of simulations of the weakly nonlinear model and the amplitude equation results. The simulations are performed by (a) ramping up and (b) ramping down the value of Da for each Pe_C , using the final state displayed in the phase diagram at the previous Da as the initial condition for the next Da value. All parameter settings are the same as in Fig. 5 in the main text. A duration of $t = 5 \times 10^4 t_0$ is used for each simulation.

and uniform state. In the opposite direction, we start from a uniform state at high Da and ramp down the value of Da [Fig. S1(b)]. The uniform state persists through the region where both dots and uniform state are stable until the uniform state is no longer stable and dots emerge. At lower Da , in the region where both stripes and dots are stable, the pattern is dominated by dots with a small number of stripes. Therefore, the results of ramping up and ramping down the value of Da show that in the region where multiple states are stable, the coexistence or dominance of one state over the other depends on the initial condition, and hysteresis is observed in the transition between the two states.

2. Comparison with the full-model simulation

Next, we repeat the simulations using the full models while all other parameters are identical to Fig. 5. The results are shown in Fig. S2. We see that the prediction of the dots region is only valid near the boundary of the uniform region, since away from the uniform region, the amplitude of the deviation from the uniform state becomes higher and the model enters the deeply nonlinear regime, which the weakly nonlinear model cannot capture. Nevertheless, $Pe_C > Da\phi_0^2\tilde{c}_0^{-1}$ (below the red dashed line) remains a good estimate for when coarsening occurs.

B. Oscillatory patterns

1. Traveling stripes and dots in 2D

Fig. S3 shows the snapshots of the simulations used to generate Fig. 6 in the main text. We first ramp up the value of α for each Pe_C , using the final state at the smaller α as the initial condition for the next α value. Then we ramp down the value of α in the opposite direction. The results during the ramp-down are displayed and used in Fig. 6 in the main text. This method of continuation enhances the smoothness of the velocity and amplitude versus α curves, although discontinuity may still occur as the system picks another pattern with a jump in its characteristic wavevector, often associated with the transition between traveling band and traveling dots. For patterns whose aspect ratio is smaller than 3.7, the velocity, represented by the red arrows, is obtained by tracking the center of mass of the

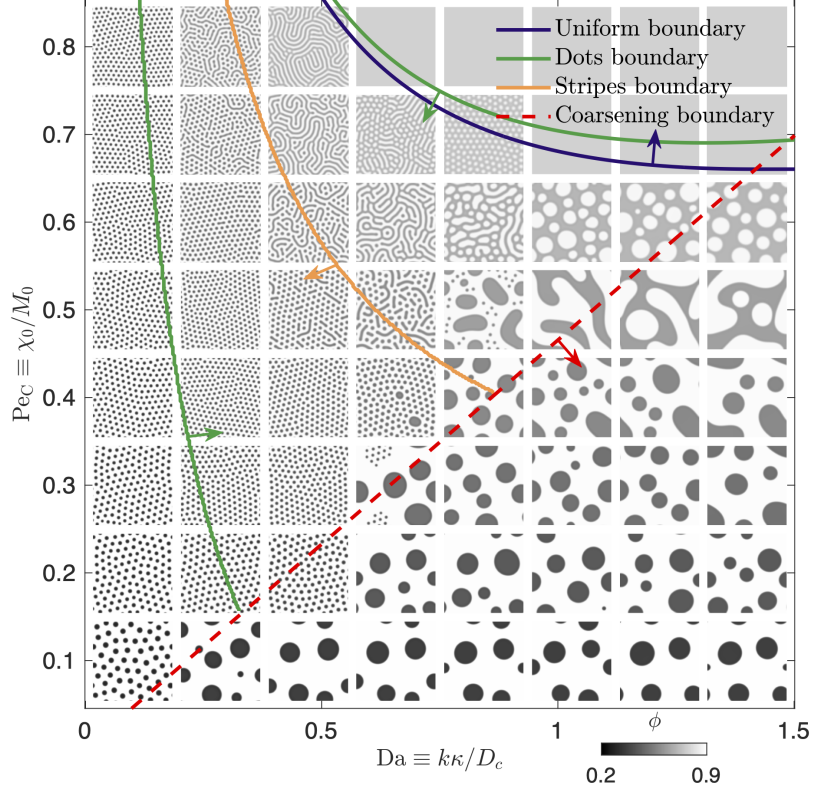


FIG. S2. Comparison of simulations of the full model and the amplitude equation results. All parameter settings are the same as in Fig. 5 in the main text. All simulations start from the uniform state with the same random perturbation as the initial condition.

pattern; otherwise, the velocity is defined by the level set velocity as described in the main text. We find excellent agreement between the predicted boundary of oscillatory patterns $\alpha_c = 4/(\text{Pe}_C \tilde{c})$, denoted by the blue dashed curve, and the simulation. With this particular set of parameters, traveling band patterns tend to occur at high Pe_C and low α , while traveling dot or short stripes patterns occur at low Pe_C and high α .

2. Traveling wave in 1D

Next, we repeat the above simulations in 1D, thus eliminating the dot patterns. Similarly, we ramp up and then down the value of α for each Pe_C and ensure that the system chooses either stationary stripes or traveling bands. As a result, compared to Fig. 6, smoother $\tilde{v} - \alpha$ and $R_\phi - \alpha$ curves are obtained (Fig. S4). Again, in Fig. S4(c), we find that $\tilde{v} - \alpha$ curves in the low Pe_C regime where infinite-period bifurcation occurs collapse well to the analytical prediction $\tilde{v} \cdot \alpha \text{Pe}_C^{-1/2} = \sqrt{\text{Da} \tilde{c}_0 \phi_0 (\alpha - \alpha_c)}$ denoted by the dashed line. However, the critical α_c in the low Pe_C regime differs from that in Fig. 6 in 2D. In 2D, the critical α_c obtained from simulation agrees with $\alpha_c = 4/(\text{Pe}_C \tilde{c}_0)$ (blue dashed curve), which is the minimum α above which traveling wave exists, according to Eq. (23), which corresponds to a wavenumber of $\tilde{k}_c = \sqrt{\text{Da} \phi_0}$. At other wavenumbers, the critical α_c is larger. We find that in 1D simulations, at low Pe_C when the pattern transitions from stationary to traveling wave, the wavelength of the traveling wave near the critical α_c transitions continuously from the wavelength of the stationary wave pattern at lower α , which suggests that \tilde{k}_c is equal to that of the stationary wave whose analytical expression is obtained in Sec. V: $k_c^2 = \sqrt{\text{Da} \text{Pe}_C \tilde{c}_0} - \text{Da} \phi_0$. Hence, the critical α_c predicted by the existence condition Eq. (23) that corresponds to the wavenumber of the stationary pattern is

$$\alpha_c = \frac{(k_c^2 + \text{Da} \phi_0)^2}{\tilde{k}_c^2 \text{Da} \tilde{c}_0 \phi_0 \text{Pe}_C} \Big|_{k_c^2 = \sqrt{\text{Pe}_C \text{Da} \tilde{c}_0} - \text{Da} \phi_0} = \frac{1}{\phi_0 (\sqrt{\text{Pe}_C \text{Da} \tilde{c}_0} - \text{Da} \phi_0)}. \quad (\text{S45})$$

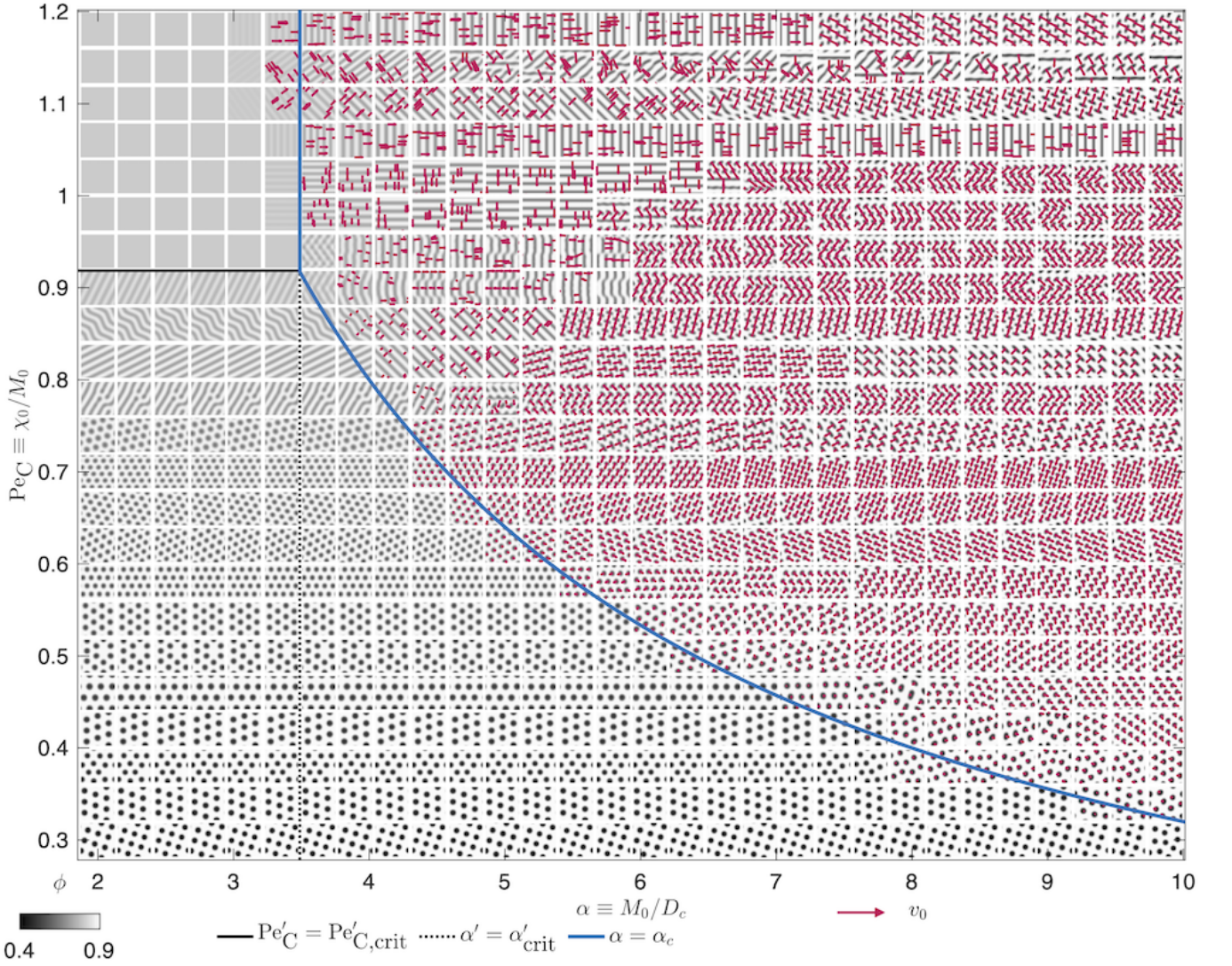


FIG. S3. Simulations used to generate Fig. 6 in the main text. Simulations are performed on a $[50l_0, 50l_0]$ periodic domain and solved on a 128×128 grid. The snapshots are taken at $t = 5 \times 10^3 t_0$. Arrows indicated the velocity of the patterns. Speed smaller than $0.05v_0$ is not shown. For stripe patterns, only regions where $|\nabla\phi| > 0.1$ are included for calculating the level set velocities, of all eligible pixels, at most 10 pixels are randomly chosen to display the velocities (red arrows). The blue solid line is the critical α for the onset of oscillatory patterns predicted by the amplitude equation.

Recall that at high Pe_C , the critical α_c is determined by the stability condition, hence overall

$$\alpha_c = \max \left\{ \frac{1}{\phi_0(\sqrt{Pe_C Da \tilde{c}_0} - Da\phi_0)}, \frac{1}{a^2} \left(\sqrt{Da} + \sqrt{Da + a\phi_0^{-1}} \right)^2 \right\}. \quad (\text{S46})$$

We see that the critical α_c agrees well with this prediction as shown by the black dashed curve in Fig. S4(d) and is larger than the blue dashed curve $\alpha_c = 4/(Pe_C \tilde{c}_0)$. The predicted traveling wave velocities at various Pe_C are plotted as the dashed curves. In the low Pe_C regime, it is given by Eq. (21) and (22) using $k_c^2 = \sqrt{Da Pe_C \tilde{c}_0} - Da\phi_0$, while in the high Pe_C regime, it is given by Eq. (27).

3. Spiral waves

Starting from spiral waves in Fig. 7 at different Pe_C as the initial condition, we ramp down α and plot the simulations in the $Pe_C - Da$ phase diagram in Fig. S5. We observe that, at low Pe_C , the spiral wave solution remains stable as α

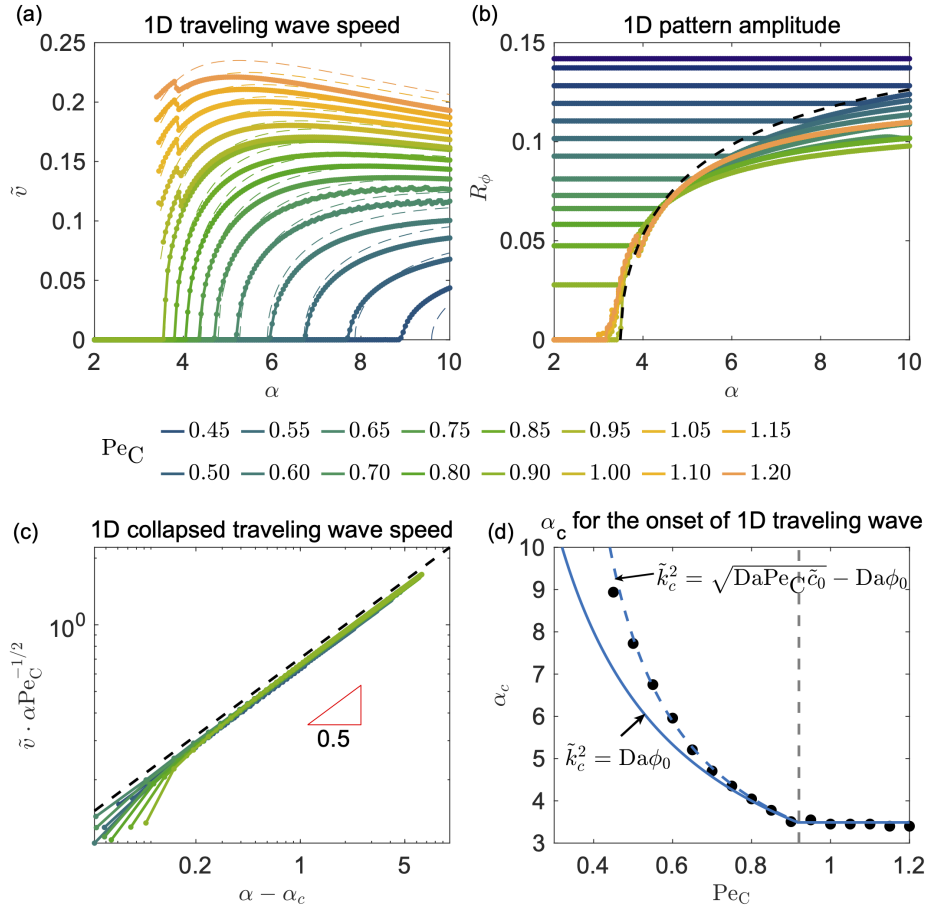


FIG. S4. Properties of the traveling waves in 1D. $Da = 0.5$, $Pe_R = 10^{-3}$, $\phi_0 = 0.8$, and $S_0/k = 1$. Simulations are performed in a 1D periodic domain whose length is $200l_0$. (a) The average normalized speed $\tilde{v} = v/v_0$ as a function of α at different Pe_C . The speed is obtained by tracking the peaks. The dashed curves of the same color are the analytical prediction from the amplitude equation [Eqs. (26) and (27)]. (c) The amplitude of the pattern as a function of α that corresponds to (b). The black dashed curve is the analytical prediction from the amplitude equation at low Pe_C [Eq. (28)]. (d) The critical α as a function of Pe_C for the onset of oscillatory patterns. Dots are from simulations (first α when $\tilde{v} > 0.01$). The blue solid curve is Eq. (29) $\alpha_c = 4/(Pe_C \tilde{c}_0)$ when $\tilde{k}_c^2 = \sqrt{Da\phi_0}$. The blue dashed curve is given by Eq. (S45) when $\tilde{k}_c^2 = \sqrt{DaPe_C \tilde{c}_0} - Da\phi_0$ to the left of the vertical dashed line, which indicates infinite period bifurcation to the left and supercritical Hopf bifurcation to the right.

decreases all the way until the pattern becomes stationary. On the other hand, at high Pe_C , the spiral wave becomes unstable below a certain α and becomes traveling plane waves.

Fig. S6(a) shows the level set velocity averaged in space and time as a function of Pe_C and α . The non-spiral-wave patterns are colored in gray. We see that the trend of the speed obtained from simulations, including the spiral waves, agrees with the prediction of the amplitude equation, which is shown in dashed curves of the same color. Similar to traveling dots and stripes, the spiral wave speed collapses according to $\tilde{v} \cdot \alpha Pe_C^{-1/2} = \sqrt{Da\tilde{c}_0\phi_0(\alpha - \alpha_c)}$ as shown in Fig. S6(b). Fig. S6(c-d) shows the amplitude R_ϕ as a function of Pe_C and α . Similar to traveling dots and stripes, the amplitude of the spiral wave increases with increasing α and decreasing Pe_C . The amplitude of the spiral wave in the regime of supercritical Hopf bifurcation agrees well with the prediction of the amplitude equation [Eq. (28)] denoted by the dashed curve.

S4. SUPPLEMENTAL MOVIES

All movies are available at this link.

1. 2D traveling wave pattern (Fig. 8a). $Pe_R = 1.9 \times 10^{-3}$, $\phi_0 = 0.70$, $Da = 0.2$, $\alpha = 4$, $Pe_C = 1$.

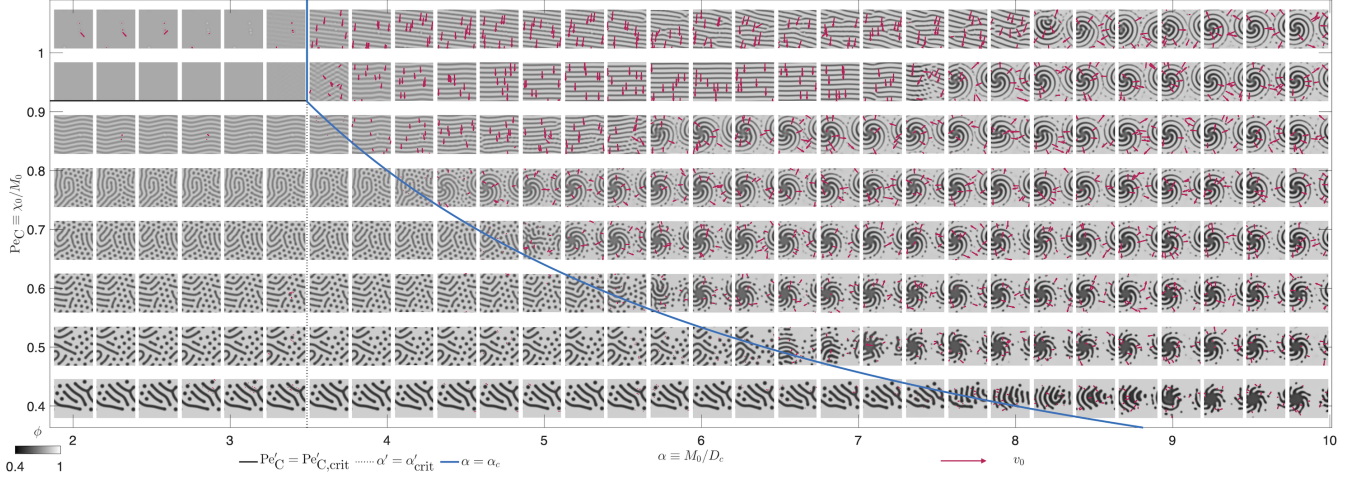


FIG. S5. Phase diagram of the spiral waves in the $Pe_C - Da$ plane. For each Pe_C , the value of α is ramped down from $\alpha = 10$, using the final state of the previous simulation at a higher α as the initial condition. Simulations are performed on a $[50l_0, 50l_0]$ periodic domain and solved on a 256×256 grid. The snapshots are taken at $t = 5 \times 10^3 t_0$. Arrows indicated the level set velocity of the patterns. Speed smaller than $0.05v_0$ is not shown. Only regions where $|\nabla\phi| > 0.1$ are included for calculating the level set velocities. The blue solid line is the critical α for the onset of oscillatory patterns predicted by the amplitude equation.

2. 2D traveling dots pattern (Fig. 8b). $Pe_R = 1.2 \times 10^{-3}$, $\phi_0 = 0.81$, $Da = 0.2$, $\alpha = 4$, $Pe_C = 1$.
3. 2D short traveling stripes pattern (Fig. 8c). $Pe_R = 1.4 \times 10^{-3}$, $\phi_0 = 0.79$, $Da = 0.56$, $\alpha = 15$, $Pe_C = 0.44$.
4. 2D dot pattern that exhibits intermittent bursts (Fig. 8d). $Pe_R = 2.4 \times 10^{-3}$, $\phi_0 = 0.80$, $Da = 0.5$, $\alpha = 10$, $Pe_C = 0.34$.
5. 3D traveling plane wave pattern (Fig. 9a). $Pe_R = 10^{-3}$, $Da = 1$, $\alpha = 10$. $\phi_0 = 0.55$, $Pe_C = 0.40$.
6. 3D traveling plane wave pattern (Fig. 9b). $Pe_R = 10^{-3}$, $Da = 1$, $\alpha = 10$. $\phi_0 = 0.55$, $Pe_C = 0.71$.
7. 3D traveling cylinder pattern (Fig. 9c). $Pe_R = 10^{-3}$, $Da = 1$, $\alpha = 10$. $\phi_0 = 0.58$, $Pe_C = 0.42$.
8. 3D traveling cylinder pattern (Fig. 9d). $Pe_R = 10^{-3}$, $Da = 1$, $\alpha = 10$. $\phi_0 = 0.58$, $Pe_C = 0.80$.
9. 3D traveling spheroid pattern (Fig. 9e). $Pe_R = 10^{-3}$, $Da = 1$, $\alpha = 10$. $\phi_0 = 0.61$, $Pe_C = 0.37$.
10. 3D traveling spheroid pattern (Fig. 9f). $Pe_R = 10^{-3}$, $Da = 1$, $\alpha = 10$. $\phi_0 = 0.61$, $Pe_C = 0.59$.
11. Dynamics of a mixture of chemoattractant consumers (green) and chemorepellent consumers (magenta) (Fig. 12).

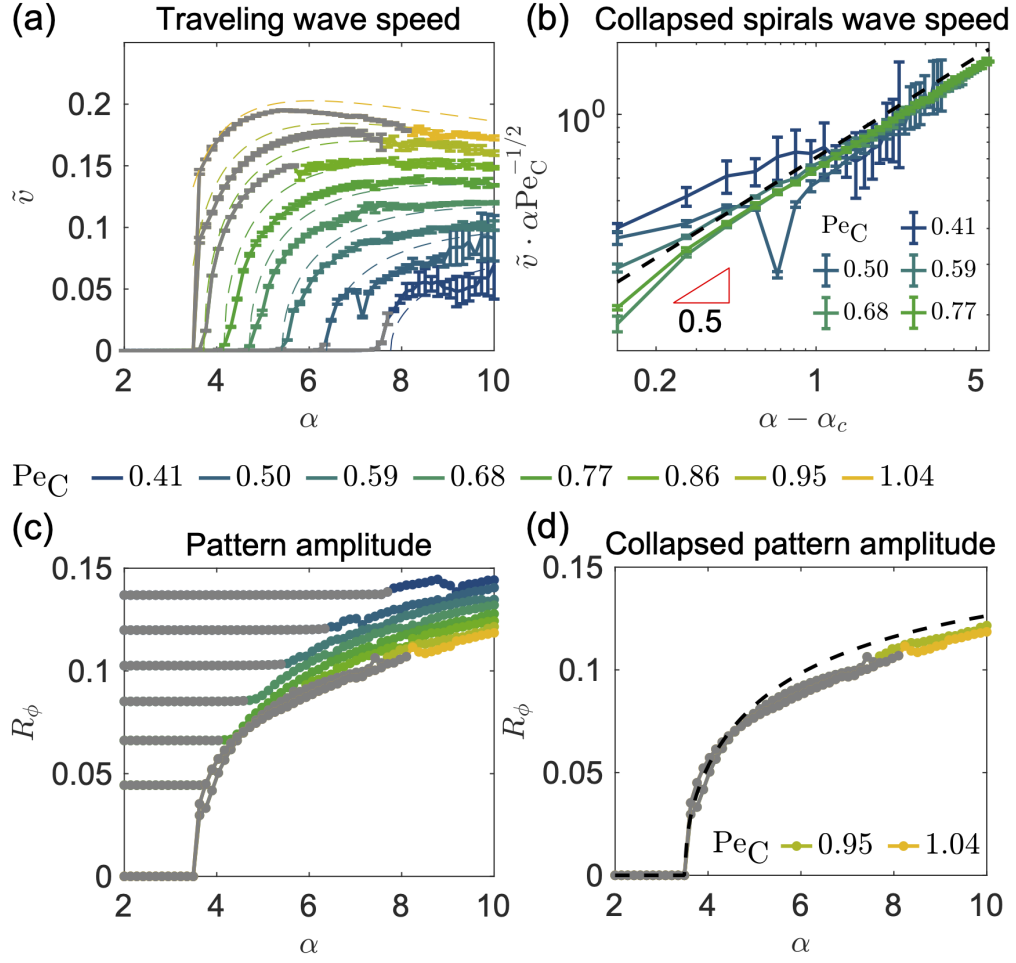


FIG. S6. Properties of the spiral waves extracted from Fig. S5. (a) The average normalized speed $\tilde{v} = v/v_0$ as a function of α and Pe_C . The speed is obtained by averaging the level set velocity in space and time. The dashed curves of the same color are the analytical prediction from the amplitude equation [Eq. (26) and (27)]. Non-spiral wave patterns (including stationary and traveling waves) are colored in gray. (b) The collapse of the spiral wave speed according to $\tilde{v} \cdot \alpha Pe_C^{-1/2} = \sqrt{Da\tilde{c}_0\phi_0(\alpha - \alpha_c)}$ (dashed line). (c) The amplitude of the pattern as a function of α and Pe_C . (d) The amplitude of the pattern in the high Pe_C regime. The black dashed curve is the analytical prediction from the amplitude equation at high Pe_C [Eq. (28)].